AD-A031 915 NAVAL SHIP SYSTEMS COMMAND WASHINGTON D C F/G 9/1
REPORT OF THE MATHEMATICAL MODEL WORKING GROUP, MEETING REPORT --ETC(U)
APR 73

UNCLASSIFIED NL

1 OF 2
AD A031915

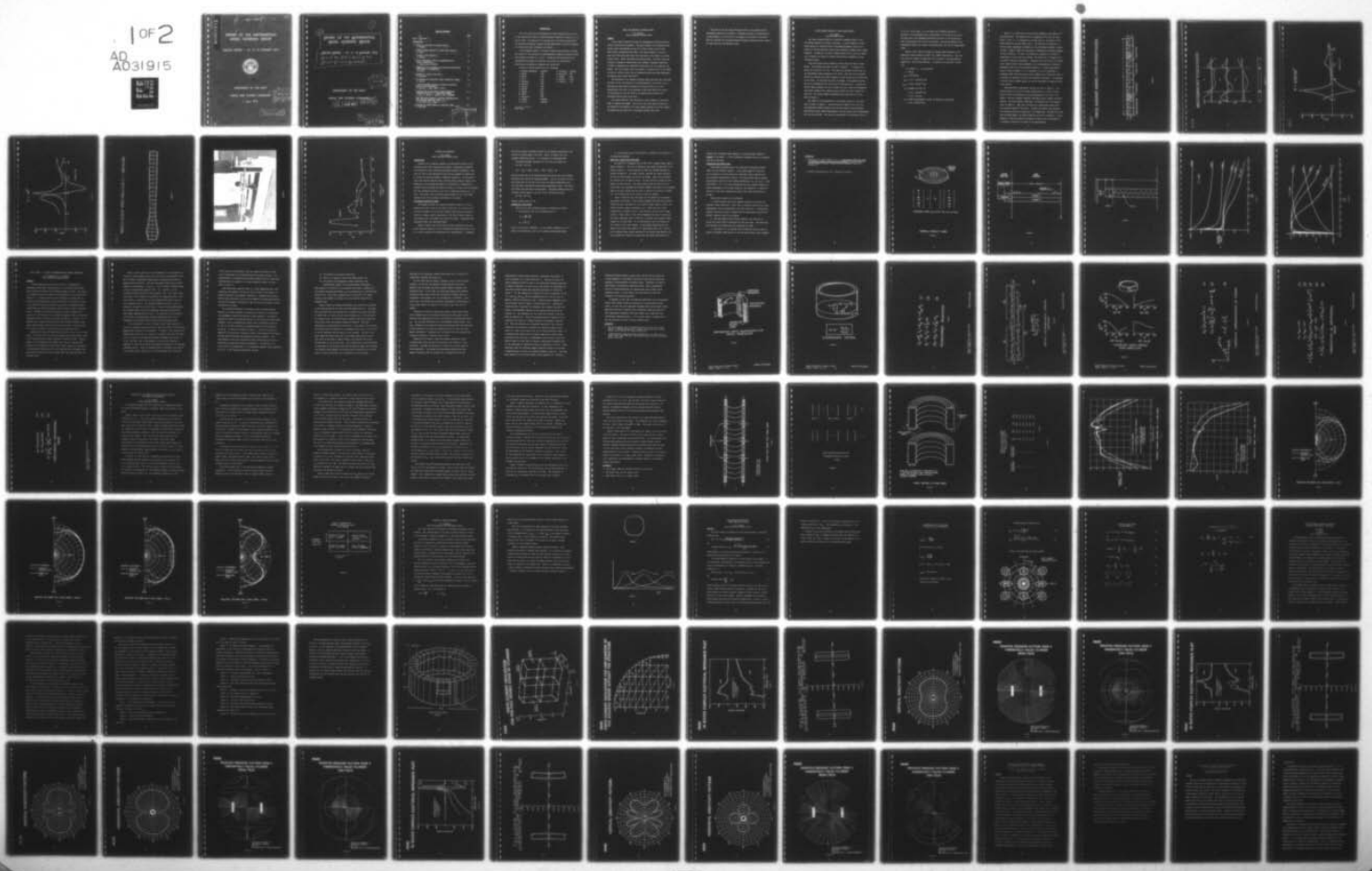

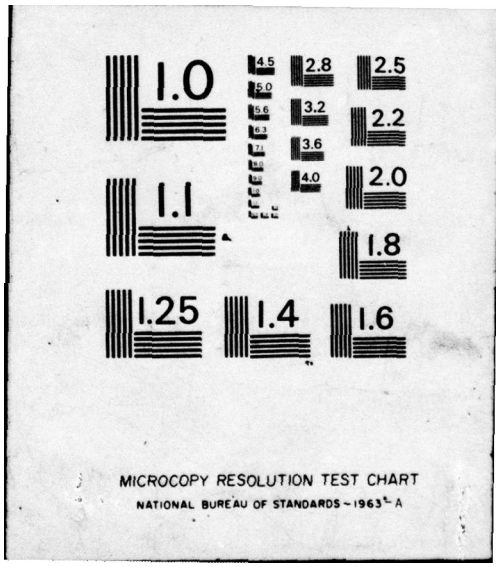
1.0
1.1
1.25
1.4
1.6
1.8
2.0
2.2
2.5
2.8
3.2
3.6
4.0
4.5
5.0
5.6
MICROCOPY RESOLUTION TEST CHART
NATIONAL BUREAU OF STANDARDS ~ 1963 A

MOST Project-4

FC

REPORT OF THE MATHEMATICAL MODEL WORKING GROUP

MEETING REPORT – 16, 17, 18 JANUARY 1973

DEPARTMENT OF THE NAVY

NAVAL SHIP SYSTEMS COMMAND

1 April 1973

(1)

(6)

REPORT OF THE MATHEMATICAL MODEL WORKING GROUP

MEETING REPORT – 16, 17, 18 JANUARY 1973

Held at the International Center, Stanford Research Institute.

DEPARTMENT OF THE NAVY

NAVAL SHIP SYSTEMS COMMAND

(11) 1 April 1973

(12) 135 p.

TABLE OF CONTENTS

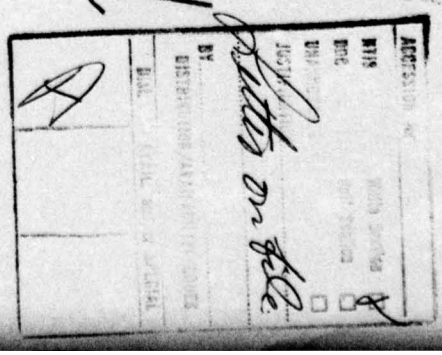

INTRODUCTION

The fourth meeting of the Mathematical Model Working Group was held at the International Center, Stanford Research Institute on January 16, 17, and 18, 1973. The purpose of the meeting was to provide the opportunity for detailed information exchange between MMWG members on matters relating to various math model techniques and results.

In his opening remarks Dr. Sherman (Working Group Chairman) reviewed the results of the Transducer and Hydromechanics Committee program development meeting of January 3, 4, and 5. During the THC meeting there was considerable discussion and interest in the need for noise models - particularly as applied to submarine hull structures.

Present at the SRI meeting were the following:

C. Sherman (Chairman)	- NUSC/NL	R. Radlinski	- NUSC/NL
G. Martin	- NUC	E. Spurlock*	- SRI
R. Smith	- NUC	J. Young*	- SRI
J. Hunt	- NUC	R. Kolesar	- NSSC
G. Benthien	- NUC	C. Campbell	- ADL
M. Knittel	- NUC		
D. Davison	- NUC		
S. Hanish	- NRL		
P. Rogers	- NRL		
R. Baier	- NRL		
L. Van Buren	- NRL		
R. Dunham	- NUSC/NL		
D. Porter	- NUSC/NL		

*Part-time

MODEL FOR BAFFLING OF FLEXURAL WAVES

C.H. Sherman
Naval Underwater Systems Center

SUMMARY

A very simple version of a model for evaluating the effectiveness of baffle structures was presented. The model consists of an infinite plane elastic plate representing the hull of a ship on which are two other plane layers representing the baffle. The layer adjacent to the hull layer has fluid properties while the other layer of the baffle is another elastic plate. Water lies beyond this second plate. The fluid layer can be given a dispersive velocity and other frequency dependent properties to make it represent more complicated structures such as a compliant tube baffle. The outer elastic layer is probably a necessary part of the baffle in order to avoid too much loss of hydrophone sensitivity when hydrophones are mounted just outside the baffle.

The solutions to two separate problems using this model were described. The first is the calculation of the effectiveness of the baffle layer in reducing the noise pressure produced by flexural waves in the hull. Specifically, the ratio of the pressure at the outer side of the baffle to the pressure on the hull without the baffle was calculated for a specified flexural wave in the hull.

The second problem is the calculation of the tendency of the baffle layer to degrade the signal. The ratio of the total signal pressure on the outside of the baffle to the total signal pressure on the hull without the baffle was calculated for a specified incident sound wave.

The ratio of the two ratios described above is the signal-to-noise improvement produced by the baffle. Although this model is oversimplified in many respects, it does serve as an example of the type of calculation which is required for evaluating different baffle concepts and other aspects of large aperture, hull-mounted arrays.

FINITE ELEMENT ANALYSIS OF TOWED ARRAY MODULES

R.R. Smith
Naval Undersea Center

The finite element method is a numerical technique useful in the vibrational analysis of complex structures. It can be applied to towed arrays giving the vibration levels (including hydrophone output) for a variety of forcing functions (cable strum, turbulent boundary layer, drogue whipping). Ultimately, the finite element method can be used as a design tool to predict the effect of various construction techniques on array self-noise levels.

This paper gives some preliminary results using the finite element method. The mathematical model is shown in Figure 1. It consists of a module 33" long with 1.25" O.D. The module has endcaps on both ends and two hydrophones freely suspended in the fluid. The left end is vibrated axially (to simulate the axial component of cable strum) and the right end is left free. An isotropic hose wall is assumed. This geometry matches that of an experimental test which will be described later. Axisymmetric "fluid" finite elements are used to model the inner fluid and axisymmetric thick shell elements with complex Young's modulus are used to model the hose wall. The finite element idealization and nodal points are also shown in Figure 1.

The effect of the hydrophones on the pressure pattern in the inner fluid is shown in Figure 2. Plotted along the length of the array are the differences between pressure (ΔP) with and without the hydrophones. Differences between radial displacements (ΔR) and between axial displacements (ΔZ) are also plotted. All curves are normalized to the maximum value of

P, R, or Z in the array. The low level curve (maximum scattering 2 percent) is for hydrophones with cross section 0.25 of that of the fluid. The high level curve (maximum scattering 10 percent) is for hydrophones with cross section 0.75 of that of the fluid. As would be expected, the hydrophones scatter the pressure and radial waves, but not the longitudinal waves.

Figures 3 and 4 show the predicted complex input impedance of the module for Young's modulus 3.39×10^7 and 1.0×10^8, respectively. Note that the curves are similar in shape with the frequency of the antiresonance higher for a large Young's modulus. A typical set of predicted results are:

$Y = 3.39 \times 10^7 \ (1 - j.25)$ Newt/met^2

$f = 100$ Hz

$F_{in} = 6.28$ Newtons

$U_{in} = (-.17, -.63) \times 10^{-4}$ met.

$U_{out} = (-.58, .25) \times 10^{-4}$ met.

P_1 = pressure at hydr. #1

$= (-.29, -.18) \times 10^5$ μbar

$= (-.42, -.26)$ psi

R_1 = radial displacement at hydr. #1 (bulge wave amplitude)

$= (.19, .22) \times 10^{-5}$ met.

Figure 5 is a frame from a motion picture showing a time history of a vibrating module. The radial motion is exaggerated 10:1 over the axial motion. Note: a) the existence of a bulge wave, b) the motion of the fluid relative to the hose wall, and c) the vibration in thickness of the hose wall, indicating a necessity to use thick shell elements to model the wall. Figure 5 shows that the model is simulating the proper phenomena in axial vibration. In order to determine the validity of the model in simulating an actual towed array module, the theory must be compared with controlled laboratory experiments. Comparison with sea tests is of limited value because several noise phenomena occur simultaneously and generally hydrophone output is the only measured quantity. A simple experimental setup is shown in Figure 6. It is intended to use this experiment to determine radial hose wall motion, input impedance and hydrophone output as a function of frequency for axial and transverse vibrations. The adequacy of various finite element models can then be determined by comparison with these results.

Some preliminary experimental results are shown in Figure 7. The vertical axis is the ratio of radial displacement at a point 10 inches from the front of the module to axial displacement at the front of the module. The curve labeled "computed" represents finite element predicted results. The curve labeled "experiment" was obtained from the apparatus shown in Figure 6. This curve is given for a region where bulge waves were actually measured (70-200 Hz). Outside this region, the component of transverse motion was comparable to the bulge wave. Although the curves have the same shapes, the levels differ by as much as 50 percent. Further analysis of both the computed and measured results will be performed in an attempt to discover the source of the discrepancies.

FINITE ELEMENT MODEL (WITH HYDROPHONES)

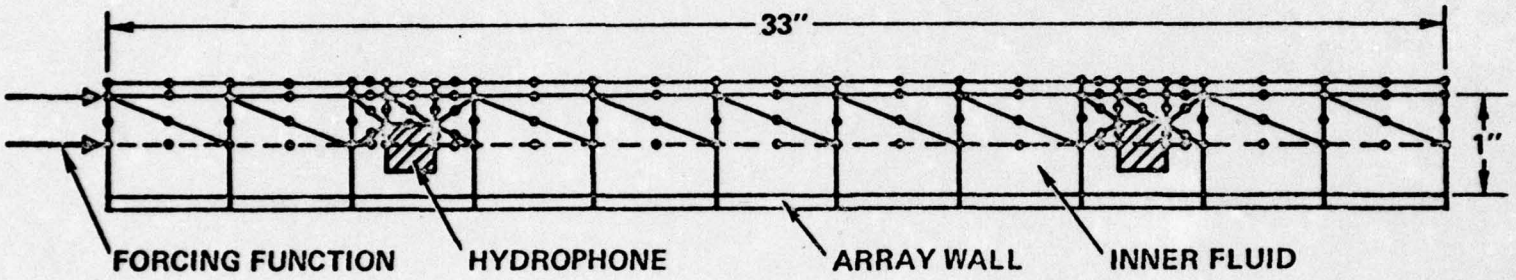

FIGURE 1

SCATTERING OFF HYDROPHONES

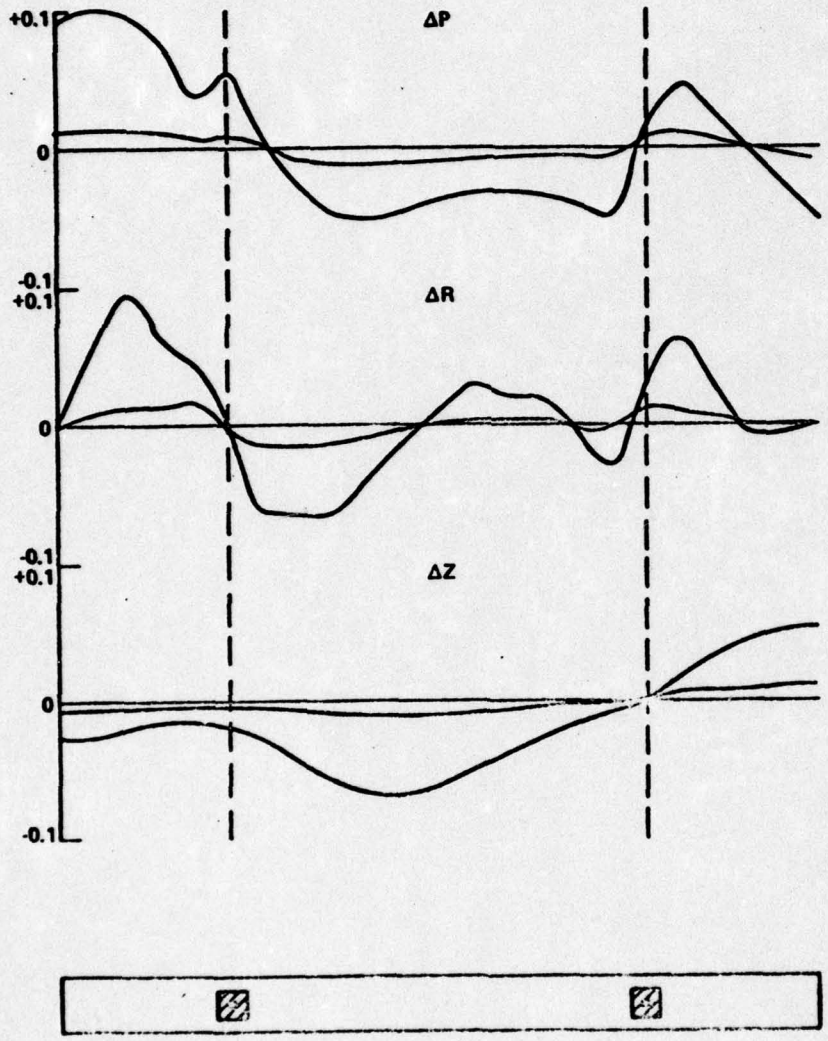

FIGURE 2

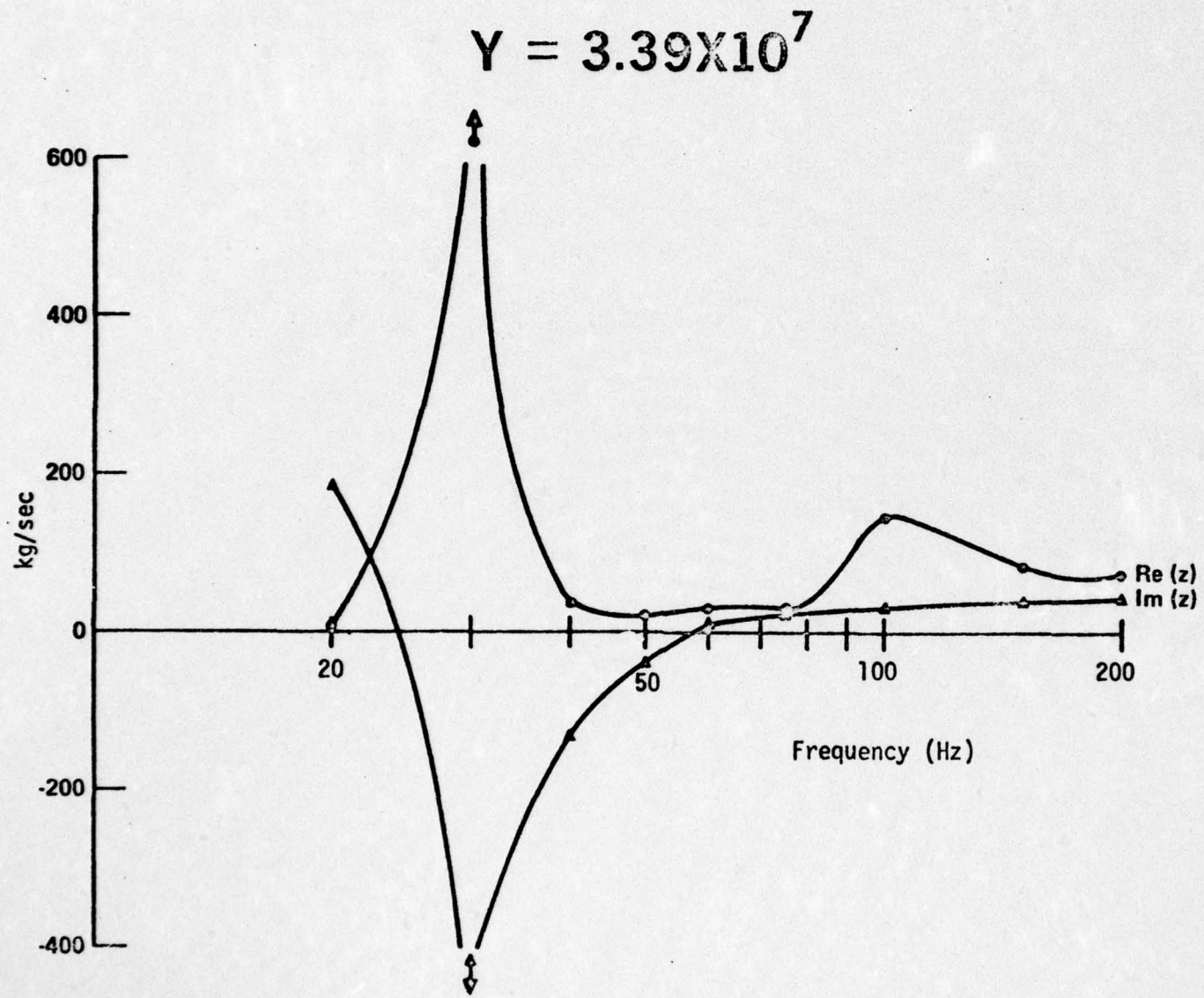
Y = 3.39X10^7
600
400
200
0
-200
-400
kg/sec
20
50
100
200
Frequency (Hz)
Re (z)
Im (z)

FIGURE 3

$Y = 10^8$

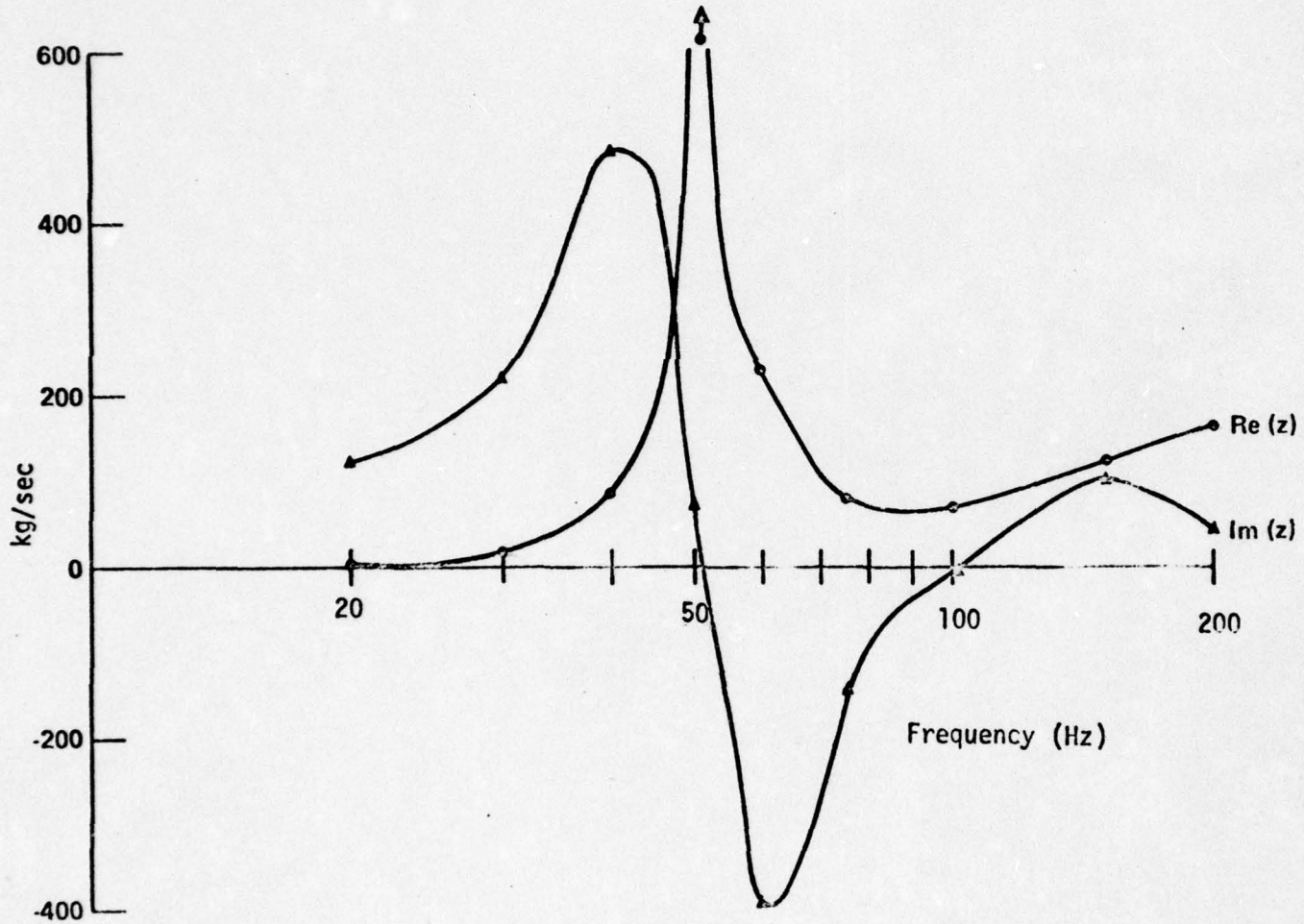

FIGURE 4

TOWED ARRAY WITH DAMPING II = .1000E-03

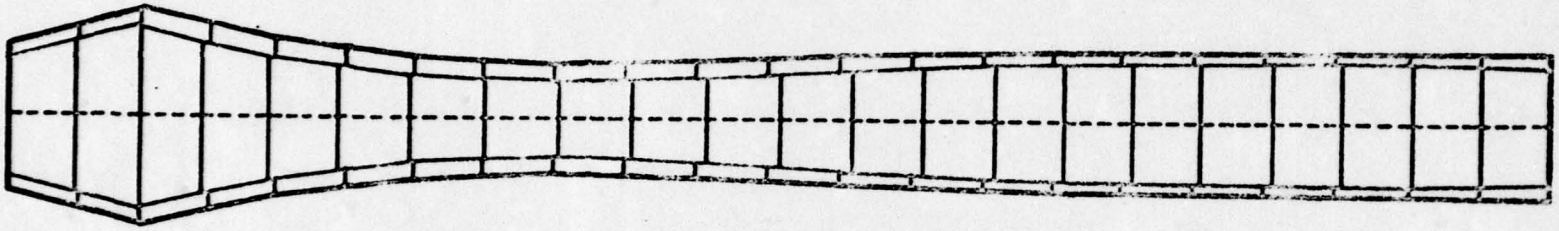

FIGURE 5

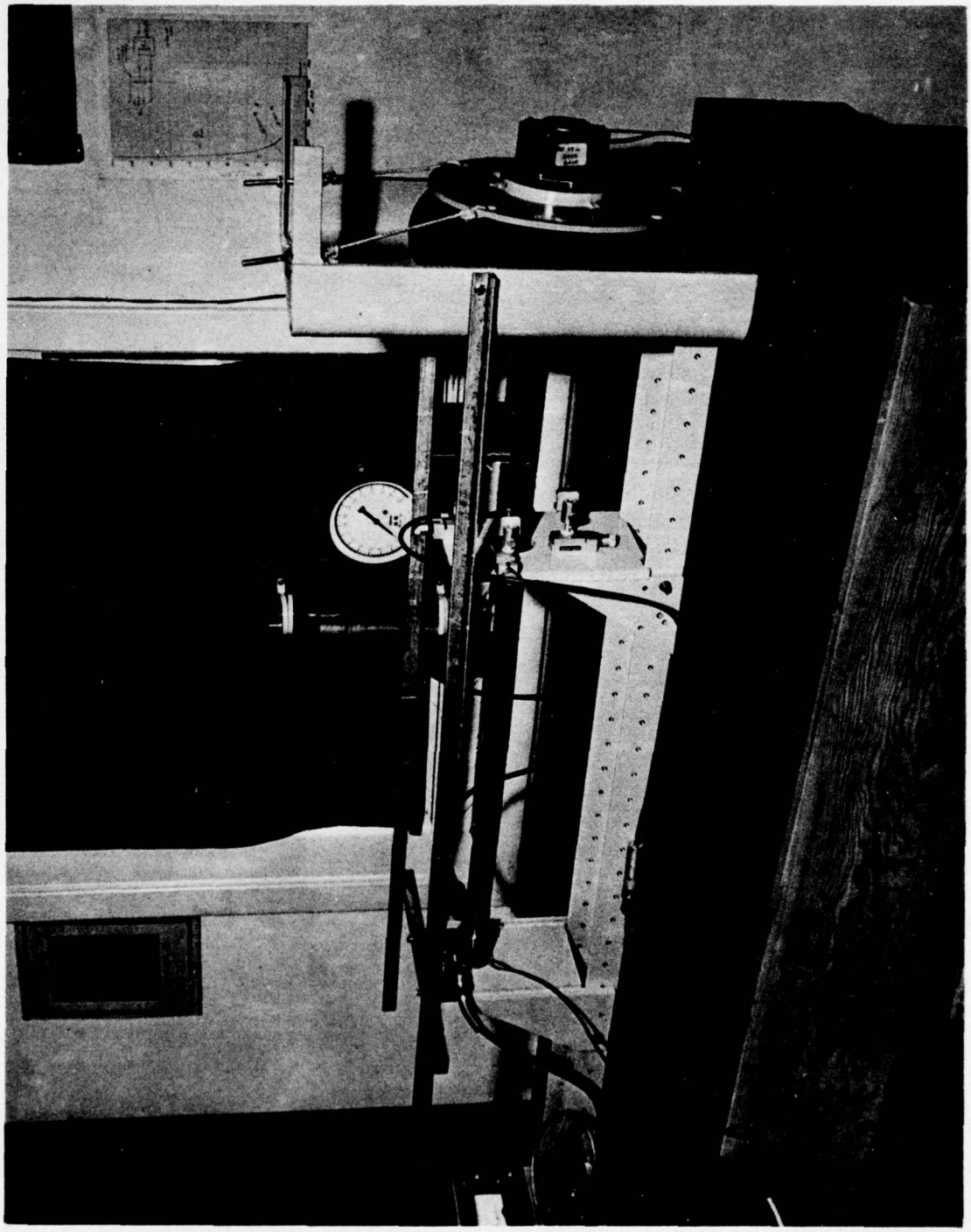

FIGURE 6

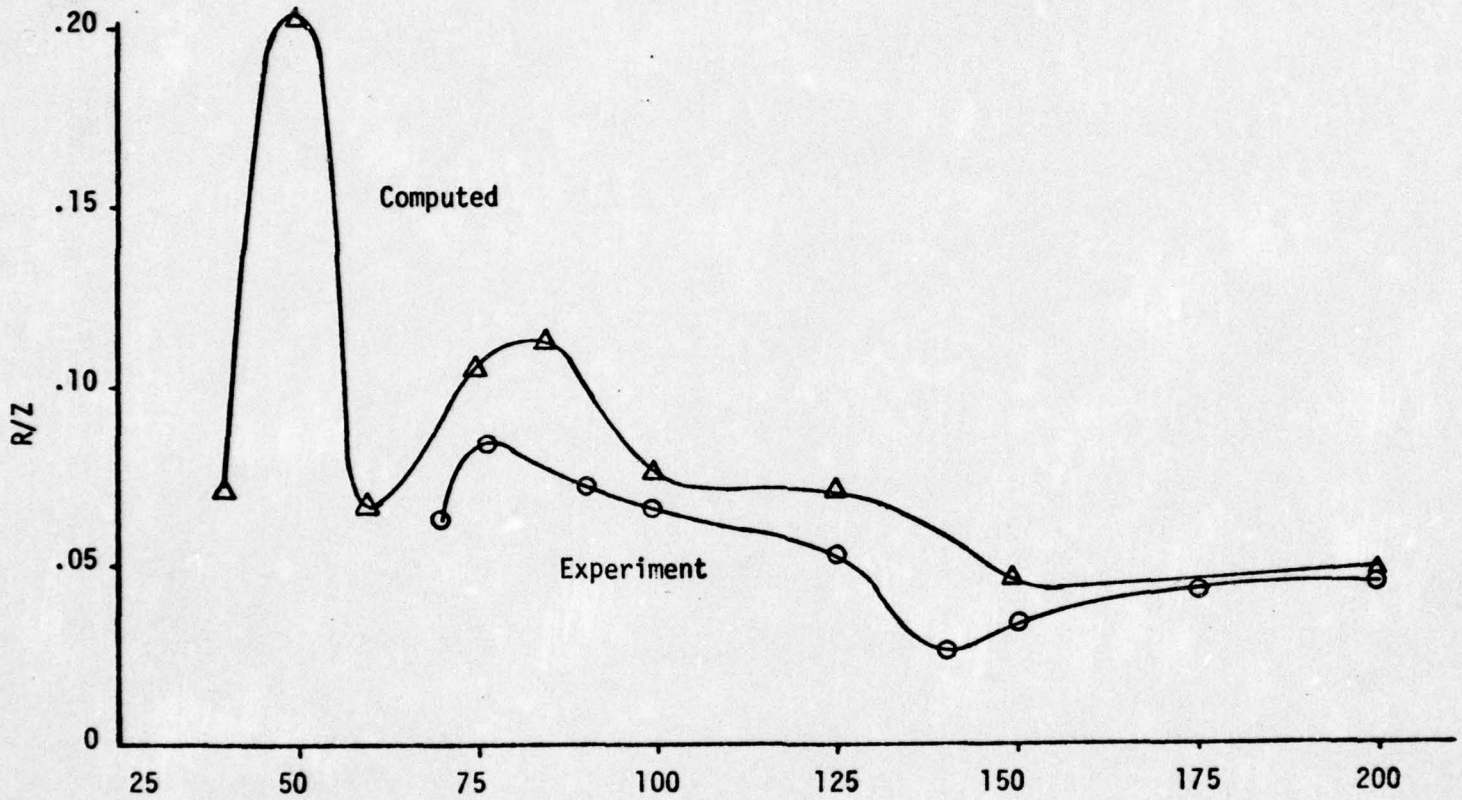
.20
.15
.10
.05
0
R/Z
Computed
Experiment
25
50
75
100
125
150
175
200
Frequency (Hz)

FIGURE 7

FLEXURAL DISC MODELING

R.W. Dunham
Naval Underwater Systems Center

INTRODUCTION

Flexural disc transducer elements are particularly useful in low frequency active sonar systems being capable of generating relatively low frequencies while maintaining reasonable physical dimensions. They also are used in line hydrophone arrays and are amenable to application as drivers in proposed designs of Helmholtz resonators. In the present talk, some results obtained from a special purpose computer program (see Reference 1) for modeling axisymmetric, multilaminate, piezoelectric flexural discs including the support structure, or hinge, will be presented. The case considered involves a disc with no radiation loading (i.e., in air). The results show an optimum hinge geometry for the class hinge studies as far as the coupling coefficient is concerned.

THE GENERAL FLEXIBILITY MODEL

The program is based on a general flexibility model for a multilaminate disc with a hole at the center (solid disc is a special case). The disc is broken up into circular contours which serve as mechanical "ports" to render a matrix description of the disc's elastic behavior. The program itself is divided into three basic parts: Subprogram FLEX, Subprogram BOUCO, and Subprogram DYANA.

Figure 1 shows a disc with typical circular contours and the port matrix equation relating a vector containing the generalized port forces to a vector containing the generalized port displacements. In addition

the vectors contain variables involved in the boundary conditions at the inside and outside edges of the disc. Hence, the matrix [D] is an expanded flexibility matrix. It is evaluated by Subprogram FLEX.

The general dynamic equations for the n-port disc model are:

$$[A]\ (W) = [D]\ (F_t)$$

$$(F_t) = (F_a) + \left\{[K] + j\omega[R] - \omega^2[M] - \omega[X]\right\}\quad (W)$$

Here the matrix [D] is the reduced flexibility matrix after the boundary conditions were applied by Subprogram BOUCO. (F_t) is the vector of total force given here as the sum of the vector of applied generalized force and load terms involving the generalized displacement vector. The matrix [A] relates the generalized displacements. Subprogram DYANA performs the necessary matrix algebra to get (W) on the left-hand side only.

$$[B]\ (W) = [D]\ (F_a)$$

Finally, DYANA solves for (W).

ASSUMPTIONS IN THE MODEL

There are two basic assumptions made in developing the model.

1. The strains S_1 and S_2 are assumed given by:

$$S_1 = Z\frac{d\emptyset}{dr} + \frac{dY}{dr}$$

$$S_2 = Z\frac{\emptyset}{r} + \frac{Y}{r}$$

where Z is the axial coordinate, r is the radial coordinate, $\emptyset$ is the slope of the deflection, and Y is the uniform radial displacement.

2. The shearing strain (if included) is assumed to be parabolic as in simple beam bending.

MODEL FOR A SIMPLE DISC WITH HINGE

The model for a bilaminar disc of PZT-4 with a simple flange hinge is shown in Figure 2. The disc is modeled as one radial section since it is uniform radially. The two laminates of PZT-4 are assumed identical in material properties. The hinge, however, requires two radial sections; one for the thick region and one for the flange. Also, three laminates are required for the hinge as shown. The disc portion is broken up into twenty circular contours. The hinge requires only one contour at its inside edge, this supplying the flexible boundary conditions for the outside edge of the disc portion when the disc is united to the hinge in a BOUCO run. The outside edge of the flange is taken as clamped.

Figure 3 shows the disc and hinge with the geometrical parameters pertaining to the model. Both resonant frequency and effective coupling coefficient were calculated vs. the relative flange length, a/(a+b), for various relative flange thicknesses, t_w/t. These plots are shown, respectively, in Figures 4 and 5. Note that for the very thick flange, a/(a+b) = .9450, there is very little dependence on a/(a+b) as expected, the values remaining close to those for a uniform, full thickness hinge clamped at its outer edge. It is interesting to note the behavior of the curves for very thin flanges. As the flange becomes shorter and shorter the curves first appear to be approaching values for a uniform, full thickness hinge, simply supported at its outside edge (shown as S.S. on the graph) but finally the curves take off toward the values for a

uniform, full thickness hinge clamped at its outside edge, (shown as clamped on the graph). A little reflection indicates this is in agreement with one's intuition.

CONCLUSIONS AND FUTURE PLANS

This computer program proved very efficient for modeling flexural discs with the flexible supports. A very large number of cases were run to generate the curves shown with relatively little computer time and relatively few manhours invested. The study showed that an optimum hinge geometry exists for the coupling coefficient, i.e., for $t_w/t \simeq .2100$ and $a/(a+b) \simeq .65$. It is also interesting that the resonant frequency is fairly independent of the flange length for this geometry. It should be pointed out that this consideration ignores the stress distribution at present.

Future plans consist of the following.

1. Actual flexural discs with supports similar to the above are presently being constructed. These will be carefully measured generating experimental curves corresponding to the ones shown here. Corresponding computer runs will be made to compare with the experimental results thus giving a thorough check on the program.

2. One shortcoming of the present program is the inability to output the stress profile throughout the disc and hinge. This deficiency will shortly be rectified when this capability is added.

3. The model is to be modified into an effective two-port model to supply an effective ABCD matrix for use with Dave Porter's array programs.

REFERENCES

1. DeLaCroix, R.F. and Cliffel, E.M., Jr., Performance Prediction Model for Radially Symmetric Flexural Disk Transducer, General Dynamics/ Electro Dynamic Division - Hydroacoustics Department Report No. HL 101-72*.

* Presently Hydroacoustics, Inc., Rochester, New York.

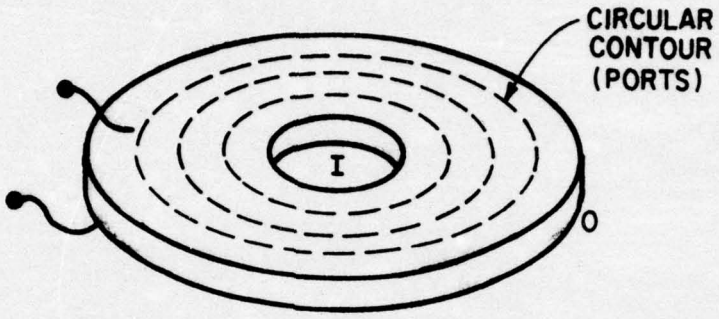

$$\begin{Bmatrix} \bar{W} \\ q \\ \Phi_O \\ Y_O \\ \Phi_I \\ Y_I \end{Bmatrix} = \begin{bmatrix} \quad \\ \quad D \quad \\ \quad \end{bmatrix} \begin{Bmatrix} \bar{F} \\ V \\ M_O \\ N_O \\ M_I \\ N_I \end{Bmatrix}$$

SUBPROGRAM **FLEX** CALCULATES [D] FOR THE MODEL.

GENERAL FLEXIBILITY MODEL

FIGURE 1

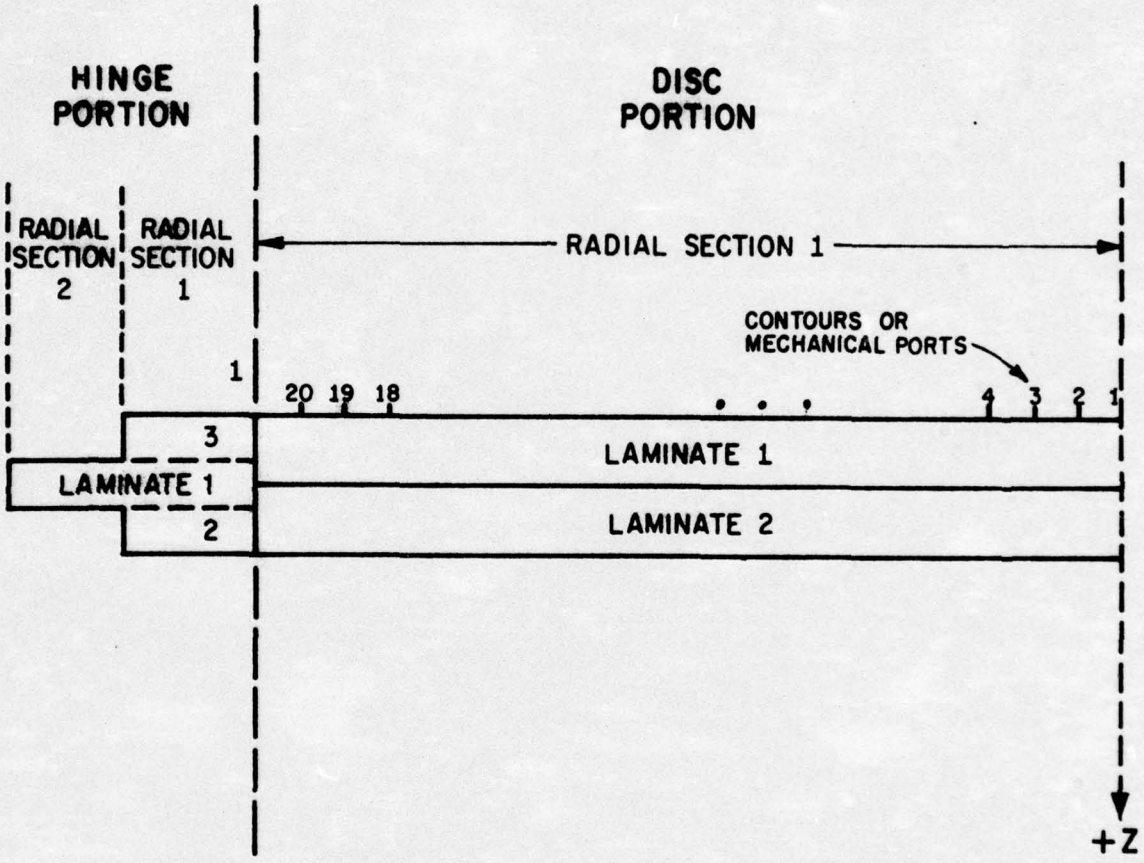
HINGE PORTION
DISC PORTION
RADIAL SECTION 2
RADIAL SECTION 1
RADIAL SECTION 1
CONTOURS OR MECHANICAL PORTS
1
20 19 18
4 3 2 1
3
LAMINATE 1
LAMINATE 1
LAMINATE 2
2
+Z

FIGURE 2

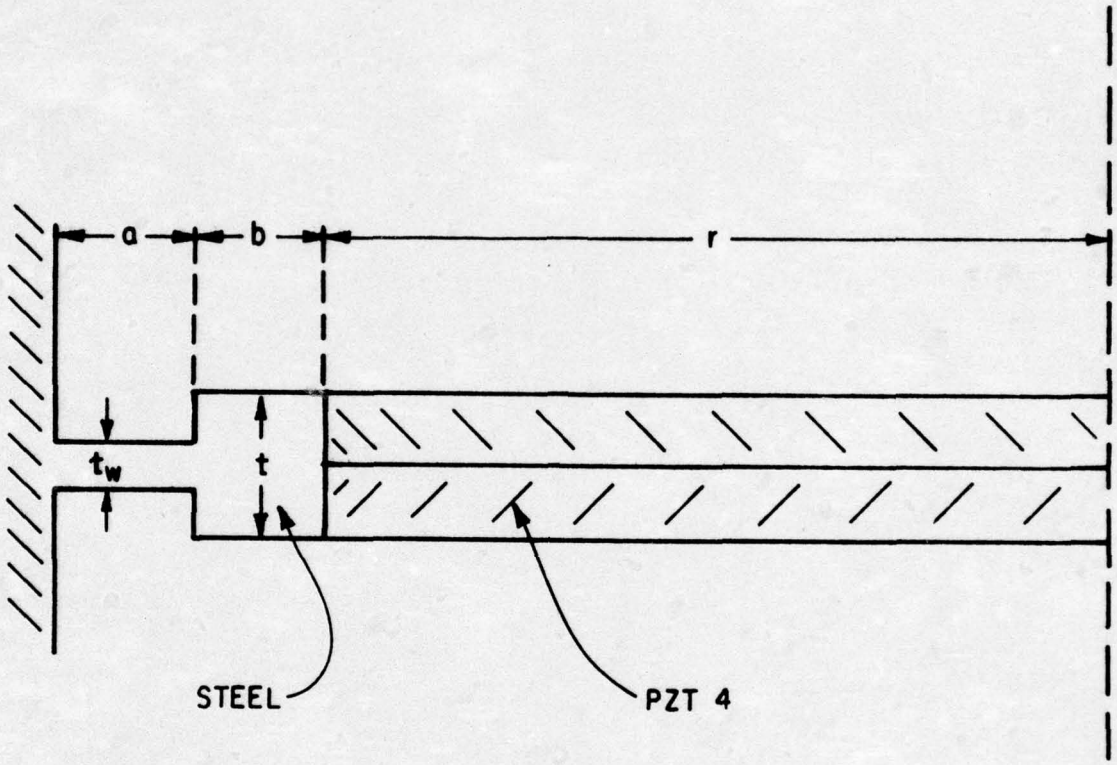

FIGURE 3

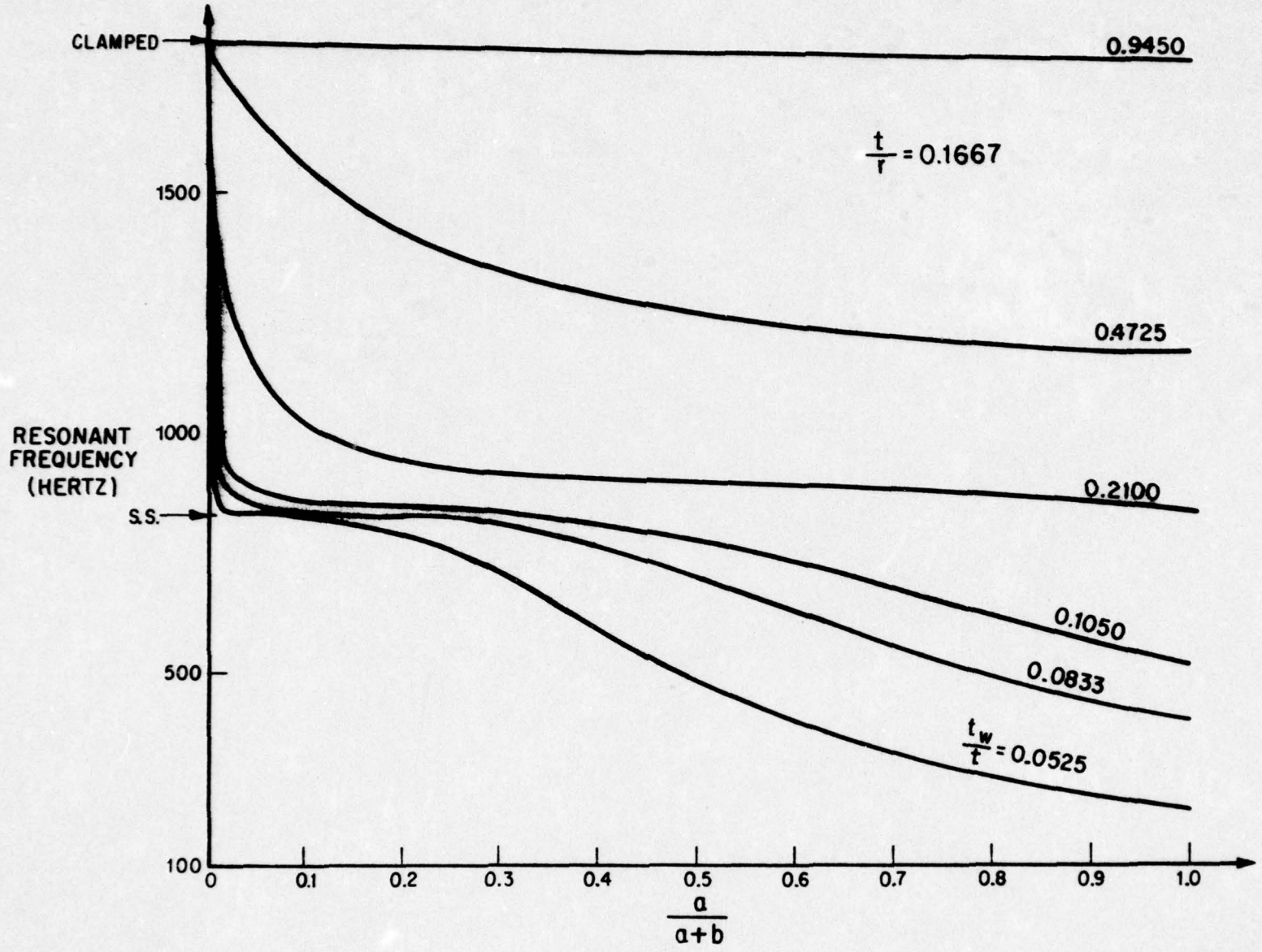
CLAMPED
0.9450
$\frac{t}{r} = 0.1667$
1500
0.4725
RESONANT FREQUENCY (HERTZ)
1000
0.2100
S.S.
0.1050
0.0833
500
$\frac{t_w}{t} = 0.0525$
100
0
0.1
0.2
0.3
0.4
0.5
0.6
0.7
0.8
0.9
1.0
$\frac{a}{a+b}$

FIGURE 4

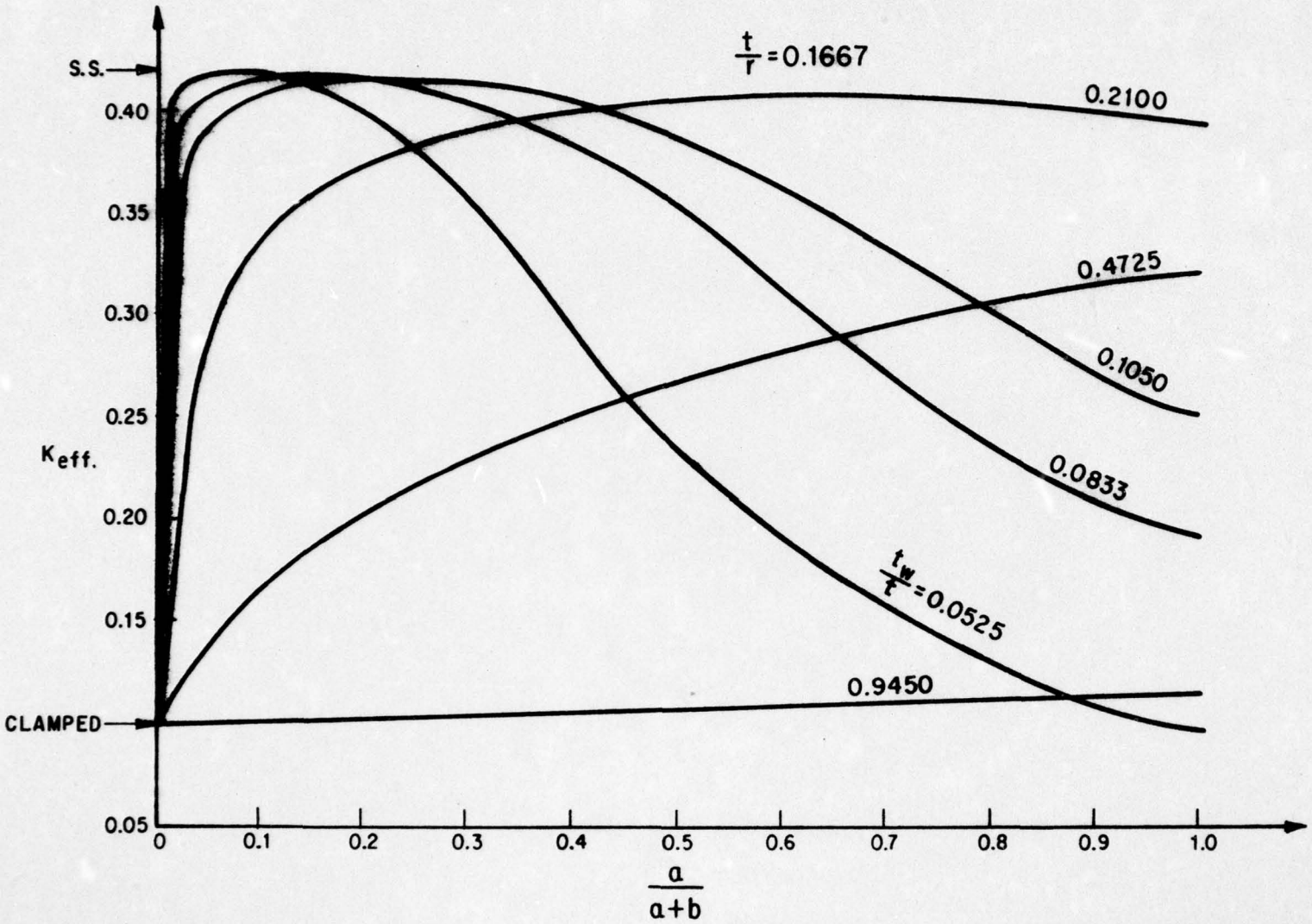
S.S.
CLAMPED
$K_{eff.}$
0.40
0.35
0.30
0.25
0.20
0.15
0.05
$\frac{t}{r}$ = 0.1667
0.2100
0.4725
0.1050
0.0833
$\frac{t_w}{t}$ = 0.0525
0.9450
0
0.1
0.2
0.3
0.4
0.5
0.6
0.7
0.8
0.9
1.0
$\frac{a}{a+b}$

FIGURE 5

USE OF ORTHOGONAL FIELDS IN MAGNETOSTRICTIVE SCROLL TRANSDUCERS

C. L. LeBlanc and C. H. Sherman
Naval Underwater Systems Center

ABSTRACT

A linear magnetostrictive theory is used to investigate the alternating small signal characteristics of a thin-wall scroll transducer polarized and driven with orthogonal magnetic fields. The concept of orthogonal excitation, advocated by researchers in the International Nickel Co., is studied from this linear viewpoint and values for the effective electromechanical coupling coefficient are presented in terms of the material coupling coefficient k_{33} derived by applying colinear polarization and excitation magnetic fields along the axis of principal strain. Although the effective coupling was found to depend quite heavily on the orientation of the resultant magnetic fields, no case was encountered where the effective coupling exceeded k_{33}. However, it is expected that orthogonal excitation will have genuine advantages under large signal driving conditions and two special cases of high amplitude drive will be discussed; linearized drive and unpolarized drive.

Magnetostrictive scroll transducers have been in use for over twenty years. In all this time the first new approach for driving these scrolls is the orthogonal drive concept invented by AR Edson at INCO. Investigation of the orthogonal drive concept shows that the coupling coefficient for an orthogonally driven scroll cannot exceed the coupling for a conventionally driven scroll but that high amplitude orthogonal drive gives better linearity and more acoustic power than high amplitude conventional drive.

Figure 1 shows a thin wall scroll transducer with two windings; an exterior toroidal winding, which is the one used in conventional scrolls, and an interior solenoidnal winding which is completely surrounded by magnetostrictive material. Bias and alternating currents can be superimposed in both windings. Current i_t in the toroidal winding produces a closed circumferential magnetic field - H_3'. Current i_s in the solenoidal winding produces an axial magnetic field - H_1' - which forms a closed path in the material as outlined by the connecting arrows. This latter field is transverse to the H_3' circumferential field; thus, the term "orthogonal drive". The resultant magnetic field is H_3 and is inclined at an angle ϕ to the H_3' field. To gain a better understanding of orthogonal drive, the scroll transducer was analyzed using linear, small signal magnetostrictive theory[1]. The objective was to determine the effective electromechanical coupling coefficient and to see if orthogonal drive provided higher coupling than conventional drive.

It is conventional to write the linear, small signal equations of state in a coordinate system with the x_3 direction parallel with the bias magnetization direction in the material. In Figure 2, the resultant bias magnetization vector (H_3) is inclined at an angle ϕ such that the tangent of ϕ is the ratio of the physically applied orthogonal bias fields, H_1' to H_3'. The first step in the analysis is to write the constitutive equations of state for polarized polycrystalline material in the unprimed coordinate system. Since the unprimed system is rotated by the angle ϕ to the primed system, which fits the scroll geometry and by which the

scroll motion can be described, then the original equations of state must be transformed to the primed system for practical analysis. The transformation is accomplished using tensor analysis and the transformed equations which are needed in the prime coordinate system are those shown in Figure 3.

These particular equations apply to a simple magnetostrictive ring transducer with magnetic isotropy and relate strain S, and stress T to magnetic intensity H and magnetic induction B. Assuming that the mechanical stress and strain, as well as the magnetic intensity and induction are uniform throughout the material, then the static and dynamic coupling coefficients are equal.

The coupling coefficient is evaluated, using an energy approach defined in the IEEE Standards on Piezoelectric Crystals, by calculating the piezomagnetic strain and induction energy densities. The specific energies are found by multiplying equation (1) by the only existing stress component, the T_3' circumferential stress, and by multiplying equations (2) and (3) by their respective alternating magnetic field components, H_1' and H_3'. The results are shown in Figure 4. Equation (1) gives the magnitude of the effective coupling in terms of the unprimed coefficients, the ones usually measured and published as material constants. The relationships between the primed and unprimed coefficients are found by comparing the appropriate bracketed expressions. In equation (1), H' is the ratio of the magnitudes of the alternating magnetic field components, H_1' to H_3'. If the following assumptions are made:

(1) the material is isotropic elastically,

(2) there is no change in volume upon magnetization, and

(3) the elastic and piezomagnetic shear coefficients have relationships similar to their piezoceramic counterparts,

then equation (1) reduces to the calculable form given by equation (2). The material coupling coefficient k_{33} is associated with a conventionally driven scroll. Many cases, ranging from H' equals zero to H' equals infinity, are possible in equation (2); only specific cases will be commented upon.

Figure 5 shows the coupling coefficient ratio plotted as a function of the bias direction $\emptyset$ for various driving signal ratios H'. The upper left plot shows that the coupling factor varies as the cosine of $\emptyset$ when H' equals zero (or, when the only active driving field is the H_3' field). For $\emptyset$ equals zero, the driving field is parallel with the S_3' strain and the H_3' bias vector, and maximum coupling is achieved. This case represents the conventionally driven scroll. For $\emptyset$ equals ninety degrees, the driving field is transverse to the magnetic bias vector, which is now in the x_1' direction, and the result is zero coupling. The plot in the upper right hand corner shows that the coupling factor varies as one-half the sine of $\emptyset$ when H' equals infinity (or, when the only active driving field is now the H_1' field). For $\emptyset$ equals zero, the driving field is transverse to the H_3' bias vector and the result is again zero coupling. For $\emptyset$ equals ninety degrees, the driving field is parallel with the bias vector in the x_1' direction, but is transverse to the S_3' strain,

resulting in the transverse coupling coefficient which is one-half the conventional coupling coefficient k_{33}.

The two lower plots in Figure 5 represent cases of more practical interest. On the left the resultant driving and bias vectors are parallel with one another and when $\emptyset$ equals roughly 55 degrees, the coupling is zero. On the right the orientation between the resultant driving and bias vectors varies and at $\emptyset$ equals 45 degrees they are transverse to one another; note, no coupling null is detected. In the former case, the parallel and transverse piezomagnetic contributions to the S_3' strain oppose one another; in the latter case, they aid one another.

Although the effective coupling was found to depend quite heavily on the orientation of the resultant driving field with respect to the resultant bias magnetization vector, the effective coupling cannot exceed k_{33} - the coupling coefficient for a conventionally driven scroll. However, orthogonal drive should have genuine advantages under high amplitude driving conditions as we will now demonstrate with two specific cases. Edson's and Huston's [2] approach will be followed with the exception that Cartesian components of induction will be used.

Equation (1) of Figure 6 shows the relation between the useful circumferential strain S_3' and the S_3 strain in the direction of magnetization. Although the relation is a static one, we will assume it holds dynamically. The square law relationship between strain and magnetic induction given in equation (2), in conjunction with the

normalization criteria (where subscript s designates saturation), is used in equation (1) to derive equation (3). Equation (3) gives the useful normalized strain in terms of the normalized Cartesian components of magnetic induction. We will now use this formula in considering the case which provides linear high amplitude operation, as outlined in Figure 7. Let the components of induction be given by equations (1) and (2), where b_{px} and b_{py} are bias components and u(t) and v(t) are, in general, arbitrary functions of time. Inserting these components in the strain formula, given in Figure 6 yields equation (3). Applying the condition shown in equation (4) eliminates the bracketed term with the squared, time dependent functions on the extreme right-hand side of equation (3). The expression for the strain then reduces to the form given in equation (5). Since both bracketed terms in equation (5) are constants, the strain is a linear function of the magnetic induction u(t). When the induction is a sinusoidal function of time, the bias components can be adjusted to maximize the alternating peak-to-peak strain to a value of the square root of two times saturation strain. In a conventionally biased scroll the peak-to-peak strain cannot exceed saturation strain and there is considerable second harmonic distortion. Figure 8 shows the other case of interest, unpolarized orthogonal drive. Let the components of induction be given by equations (1) and (2). These conditions cause the resultant magnetic induction vector to be constant in magnitude and to rotate at an angular frequency, omega (ω). Inserting these equations in the strain formula yields equation (3). Driving to

saturation induction makes b_o equal unity, and then the S_3' strain has a fixed component of one-quarter saturation strain with an alternating component of three-quarters saturation strain. Therefore, the peak-to-peak strain is three-halves saturation strain. When a conventional scroll is driven unpolarized, the peak-to-peak strain cannot exceed saturation strain. In both cases, the strain varies at twice the frequency of the driving induction.

In summary, we note that the coupling coefficient for an orthogonally driven scroll cannot exceed the coupling for a conventionally driven scroll. We also note that polarized orthogonal drive gives higher strain amplitude with better linearity than conventional polarized drive and that unpolarized orthogonal drive gives higher strain amplitude than conventional unpolarized drive. For the latter cases, orthogonal drive has the potential for about 3 dB more acoustic power.

REFERENCES

1. "Use of Orthogonal Fields in Magnetostrictive Scroll Transducers", Charles L. LeBlanc and Charles H. Sherman, Naval Underwater Systems Center, TM No. TD12-75-72, dated 2 March 1972.

2. "High-Performance Magnetostrictive Transducers", A.P. Edson and E.L. Huston, Tech. Paper 788-T-OP, INCO (Paul D. Merica Research Laboratory dated 9 June 1972.

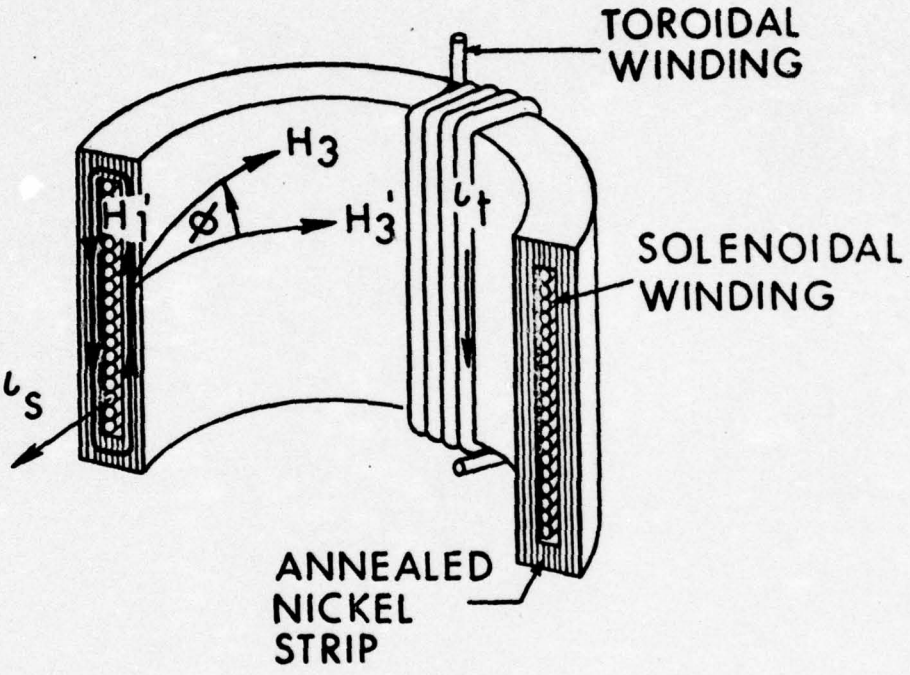

ORTHOGONAL-DRIVE MAGNETOSTRICTIVE
SCROLL TRANSDUCER

FIGURE 1

Official Photograph

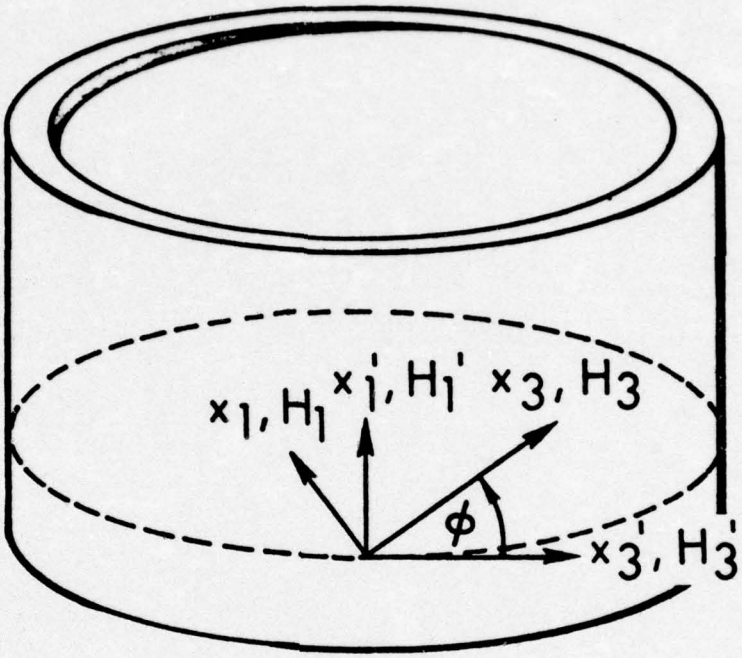

$$\tan \phi = \frac{H_1' \text{ d.c.}}{H_3' \text{ d.c.}}$$

COORDINATE SYSTEM

FIGURE 2

$$S'_3 = s^{H'}_{33}\, T'_3 + d'_{13}\, H'_1 + d'_{33}\, H'_3 \qquad (1)$$

$$B'_1 = d'_{13}\, T'_3 + \mu^{T'}_{33}\, H'_1 \qquad (2)$$

$$B'_3 = d'_{33}\, T'_3 + \mu^{T'}_{33}\, H'_3 \qquad (3)$$

TRANSFORMED EQUATIONS

FIGURE 3

Naval Underwater Systems Center
NP24 - 47473 - 11 - 72

$$k' = \left| \frac{\overbrace{\left[d_{31} \sin^3\phi + (d_{33} - d_{15}) \sin\phi \cos^2\phi \right]}^{d'_{13}} H' + \overbrace{\left[d_{33} \cos^3\phi + (d_{31} + d_{15}) \sin^2\phi \cos\phi \right]}^{d'_{33}}}{\left\{ \underbrace{\left[s^H_{33} \cos^4\phi + s^H_{11} \sin^4\phi + (2s^H_{13} + s^H_{55}) \sin^2\phi \cos^2\phi \right]}_{s^{H'}_{33}} \underbrace{\mu^T_{33}}_{\mu^T_{33}} \left[1 + H'^2 \right] \right\}^{\frac{1}{2}}} \right| \quad (1)$$

$$\frac{k'}{k_{33}} = \left| \frac{\left[\cos\phi - H' \frac{\sin\phi}{2} \right]}{\left[1 + H'^2 \right]^{\frac{1}{2}}} \right| \quad (2)$$

EFFECTIVE ELECTROMECHANICAL COUPLING COEFFICIENT

FIGURE 4

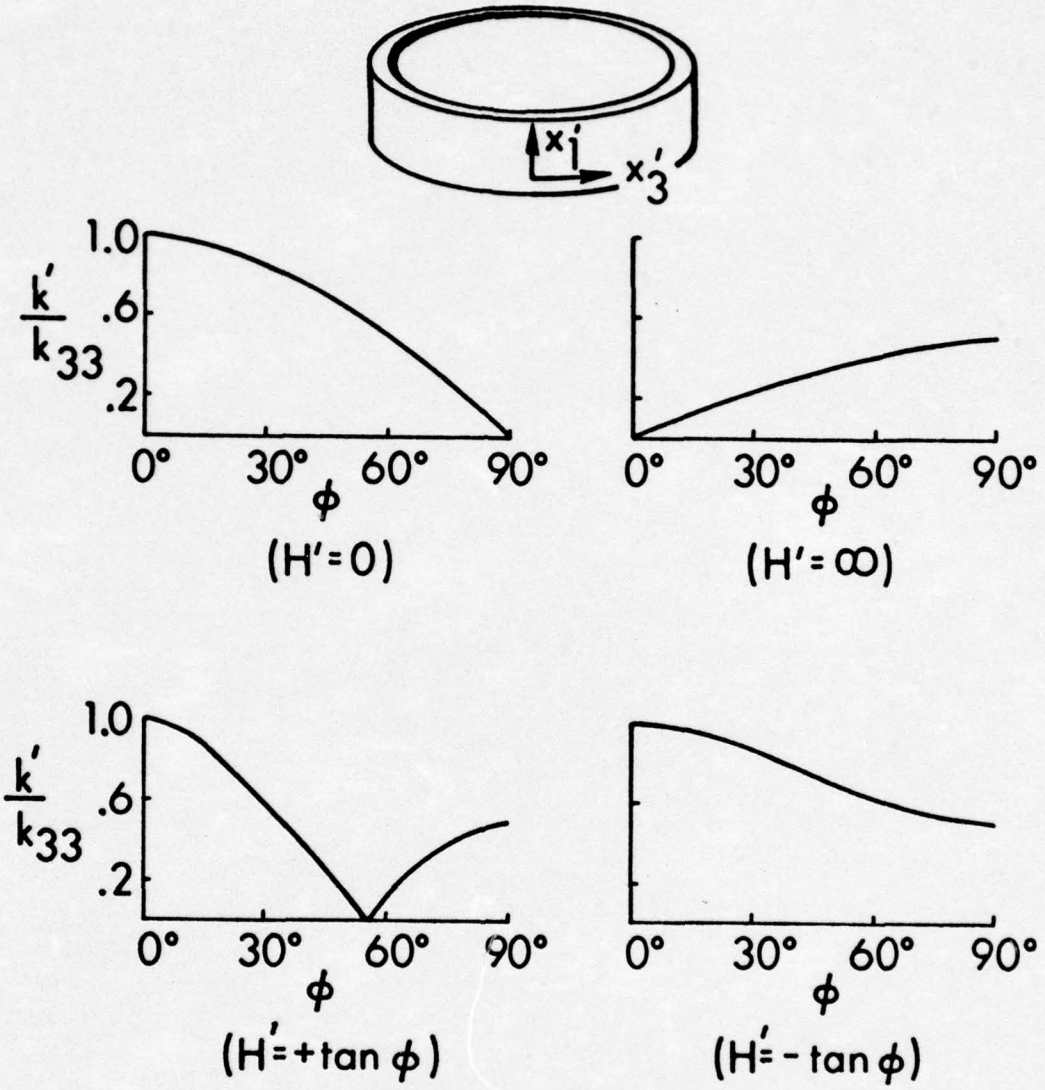

COUPLING RATIO VERSUS
BIAS DIRECTION

FIGURE 5

Naval Underwater Systems Center
NP24 - 47477 - 11 - 72

Official Photograph

$$S_3' = \frac{1}{2} S_3 (3\cos^2\phi - 1) \quad (1)$$

$$S_3 = S_s \left(\frac{B}{B_s}\right)^2;\ S = \frac{S_3'}{S_s};\ \text{and}\ b = \frac{B}{B_s} \quad (2)$$

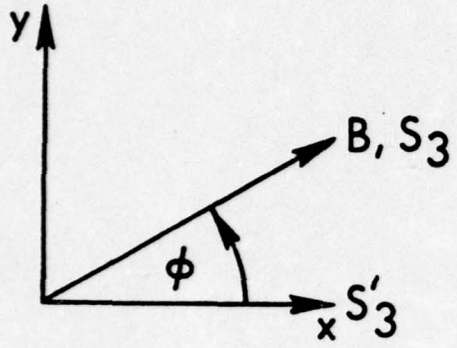

$$S = b_x^2 - \frac{1}{2} b_y^2 \quad (3)$$

CARTESIAN REPRESENTATION OF STRAIN

FIGURE 6

Naval Underwater Systems Center
NP24 - 47471 - 11 -72

$$b_x = b_{px} + u(t) \tag{1}$$

$$b_y = b_{py} + v(t) \tag{2}$$

$$S = \left[b_{px}^2 - \frac{1}{2} b_{py}^2 \right] + \left[2 b_{px} u(t) - b_{py} v(t) \right] + \left[u(t)^2 - \frac{1}{2} v(t)^2 \right] \tag{3}$$

$$v(t) = \sqrt{2}\ u(t) \tag{4}$$

$$S = \left[b_{px}^2 - \frac{1}{2} b_{py}^2 \right] + \left[2 b_{px} - \sqrt{2}\, b_{py} \right] u(t) \tag{5}$$

LINEARIZATION BY ORTHOGONAL DRIVE

FIGURE 7

Naval Underwater Systems Center
NP24 - 47475 - 11 - 72

Official Photograph

$$b_x = b_o \sin(wt) \qquad (1)$$

$$b_y = b_o \cos(wt) \qquad (2)$$

$$S = \frac{1}{4} b_o^2 - \frac{3}{4} b_o^2 \cos(2wt) \qquad (3)$$

UNPOLARIZED ORTHOGONAL
DRIVE

FIGURE 8

Naval Underwater Systems Center
NP24 - 47469 - 11 - 72

COMPARISON OF TWO METHODS FOR ANALYZING FREE-FLOODED RING ARRAYS OF TRANSDUCERS

D.T. Porter
Naval Underwater Systems Center

Two computer programs used for predicting the transmitting behavior of coaxial free-flooded arrays of transducer rings are discussed in this paper.

Figure 1 shows a cross section of an array of three transducer rings, labelled T_1, T_2, T_3. In the gaps between transducers, and at the ends of the array are placed "water rings", having the thickness of the transducer rings and the density of water. Mutual coupling coefficients between all transducer and water rings are calculated in conventional cylindrical coordinates by Rogers' equations on the outer and inner surfaces of an infinite rigid cylinder. Thus, the inner and outer surfaces of the transducer rings are connected by the action of the water rings. Unfortunately, the formulation of this "water ring" method requires the extension of the cylindrical surface past the end water rings to be rigid. Because of this mathematical approximation, the predicted pattern will be inaccurate near the array's axis.

In Figure 2 we show that for M transducer rings and N water rings array equations for M+N radiators can be derived, as in equation (1). F is the driving force vector, Z is the mutual impedance matrix, and V is the velocity vector. The velocity vector is solved for by inverting the Z matrix, as in equation (2). The NUSC/NL program is presently limited to M+N less than or equal to 60. By breaking the program into three

separate parts this limitation could be raised to 200. However, the largest array of coaxial free-flooded rings of which we have knowledge is 18.

An important assumption of this program is that the water rings with their discrete velocities will adequately simulate the continuous velocity variations that actually exist in the gaps between transducer rings and at the ends of the array.

Calculations have been done for arrays with various numbers of water rings per gap and per end. If the gap is much less than a wavelength and also less than the transducer height, then one or two water rings per gap will suffice. However, on the extension of the cylindrical surface at the ends of the array the velocity normal to the cylindrical surface is changing rapidly in magnitude and phase. As yet, a satisfactory method for determining the required number and size of end water rings has not been determined.

The program as written requires the inner and outer velocities of any ring to be equal and out of phase, and the top and bottom edges of each ring have zero normal velocity. The program contains lumped circuits for simple ceramic and magnetostrictive rings. The output includes source level, directivity index, beam patterns, radiation impedance data, currents, voltages, powers, and efficiency.

The second program (ref. b) is based upon the Helmholtz Integral formulation. In this program we combined the NRL Multiple Ring SHIP Program (courtesy of Peter Rogers) with the lumped element transducer

model of the Water-Ring Program. The computer input and output of the two programs (i.e., Rogers' and Porter's) contain nearly the same items.

In the SHIP model, the transducer rings are subdivided into bands on their four surfaces, as is shown in Figure 3. The SHIP model calculates mutual impedance coefficients between the i^{th} and j^{th} rings of an array by imposing a unit velocity on the i^{th} ring, and calculating the pressure on the j^{th} ring. For any ring, the ratios of the inner, outer, and edge velocities must remain fixed over the array. The outer velocity is treated as the reference velocity. These reference velocities are determined by the matrix - inversion solution of the force-impedance - velocity equations shown in Figure 2. In calculating mutual impedance coefficients (Z_{ij}), the Helmholtz Integral model takes into account the scattering produced by all the rings. If each of the N transducers have M bands, then NxM equations are required to solve for the pressures on the NxM bands. Note that in the Water-Ring Program the calculation of Z_{ij} between bands on an infinite cylinder involved only bands i and j.

We now examine the Z_{ij} matrix of a four ring array, using the Helmholtz Integral Program. The rings have a mean radius of 2.58 inches, a height of 0.75 inch, a thickness of 0.25 inch, and a small gap between rings of 0.06 inch. The array is resonant in water around 10 kHz; the Z_{ij} presented are for 4 kHz. The inner and outer velocities on the ring surface are assumed to be equal and out of phase; the top and bottom edge velocities were assumed to be zero.

Figure 4 shows the 1-1 and 1-2 terms of the Z_{ij} matrix, for various numbers of side and top bands. Note that as the number of bands is

increased the convergence of the matrix elements is slow, particularly for the resistive elements, R_{11} and R_{12}. A free-flooding ring transducer is basically a dipole radiator, with a large amount of cancellation of the radiation from the two sides. Many bands may be needed to predict this cancellation. Although the ring thickness at 4 kHz is only about $\lambda/60$, several bands are needed on the top and bottom edges, because the pressure is changing very rapidly across these surfaces. Note the R_{11} and R_{12} for I (top bands)=2 and J(side bands)=6. For I=2 and J=8 there is only about a two percent decrease in R_{11} and R_{12} compared to I=2 and J=6. However, for the I=4, J=6 case there was about a nine percent decrease in R_{11} and R_{12} compared to I=2, J=6. Also we note that, for all the cases in Figure 4, $R_{12} > R_{11}$, so that the mutual resistance between rings 1 and 2 was actually greater than the self-resistance of ring 1. In conventional baffled arrays, it is unheard of for the mutual resistance between two radiators to exceed the self-resistance of one of them. Apparently, the pressure cancellation in the R_{12} calculation was less than for R_{11}. At this frequency, $X_{11} > X_{12}$, and $X_{12} >> R_{11}$ or R_{12}. However, if the ring's Thevenin internal reactance nearly cancelled the radiation reactance, then the condition of $R_{12} > R_{11}$ could cause the array's velocity control to be erratic.

The multiple ring SHIP program operating on the NUSC Univac 1108 can use up to 96 total bands in an array. For I=4, J=8, there are 24 bands per ring, which would limit the maximum number of rings to only 4! Using smaller I and J enables one to handle larger arrays, but with less accuracy. However, there seems no reason why the required I and J should get larger

as the gap width becomes larger. Recall that with the Water-Ring Program the calculation becomes more difficult as gap width increases.

Figure 5 compares calculated and measured (ref. c) transmitting current responses for this same four ring array. At most frequencies, the Helmholtz Integral program agrees more closely with the measurement than does the Water-Ring program. The gaps between rings are about $\lambda/100$ at 10 kHz, and the gaps are also much less than the ring height, so that the water rings should well simulate the action in the gaps. However the whole array is only slightly longer than $\lambda/2$ at 10 kHz. Therefore, the array end effects are important, and the Water-Ring Program is not reliable in modeling end effects.

The calculations did not take into account any of the array's mounting structure. Slightly off of each end of the array was a fiberglass ring which supported the wires that excited the magnetostrictive material. The fiberglass rings must have had some effects on radiation around the ends of the array, and are partly responsible for the difference between the measurement and the Helmholtz Integral calculations. Other causes for this difference are inaccuracies in the transducer circuit model, in the Z_{ij} matrix, and in the assignment of the relative velocities on the different ring surfaces.

Figure 6 compares calculated N_{DI} for the two mathematical models for the same four ring array. The calculated N_{DI} for the Water-Ring model is lower for all frequencies, especially 10-14 kHz. This difference is calculated N_{DI} is consistent with the calculated beam patterns.

Figures 7, 8, 9, and 10 compare the measured patterns with those calculated at 6.0, 9.5, 12.0, and 14.0 kHz. For most of these frequencies all three of these patterns agree well except near the array axis. In general, the Helmholtz Integral patterns are more directive than the measured patterns, which are in turn more directive than the Water Ring patterns.

One of the objectives of this project is to establish which types of arrays are best suited to each model. Two parameters are used to categorize an array. One is simply the number of rings. The second is the ratio of the gap width to the ring height.

Figure 11 shows some of our conclusions with respect to the usefulness of the two models. This chart is based on some intuition and a limited amount of array calculations (not presented here). The chart suggests that the Water-Ring program gives poor results for sparse arrays, and the Helmholtz Integral program deteriorates for arrays of more than 10 rings. In those cases where either program is useable, the Helmholtz Integral program should be more accurate. Presently neither program can accurately predict the behavior for a large, sparse array. Hopefully this situation can be improved by new approximations, probably based on the Helmholtz Integral formulation.

REFERENCES

a. JASA, August 1968, pp. 514-522, Article by D.T. Porter.

b. NRL Report 7240, by P.H. Rogers, 1972.

c. NUSL Report 723, by T.J. Meyers, 1966.

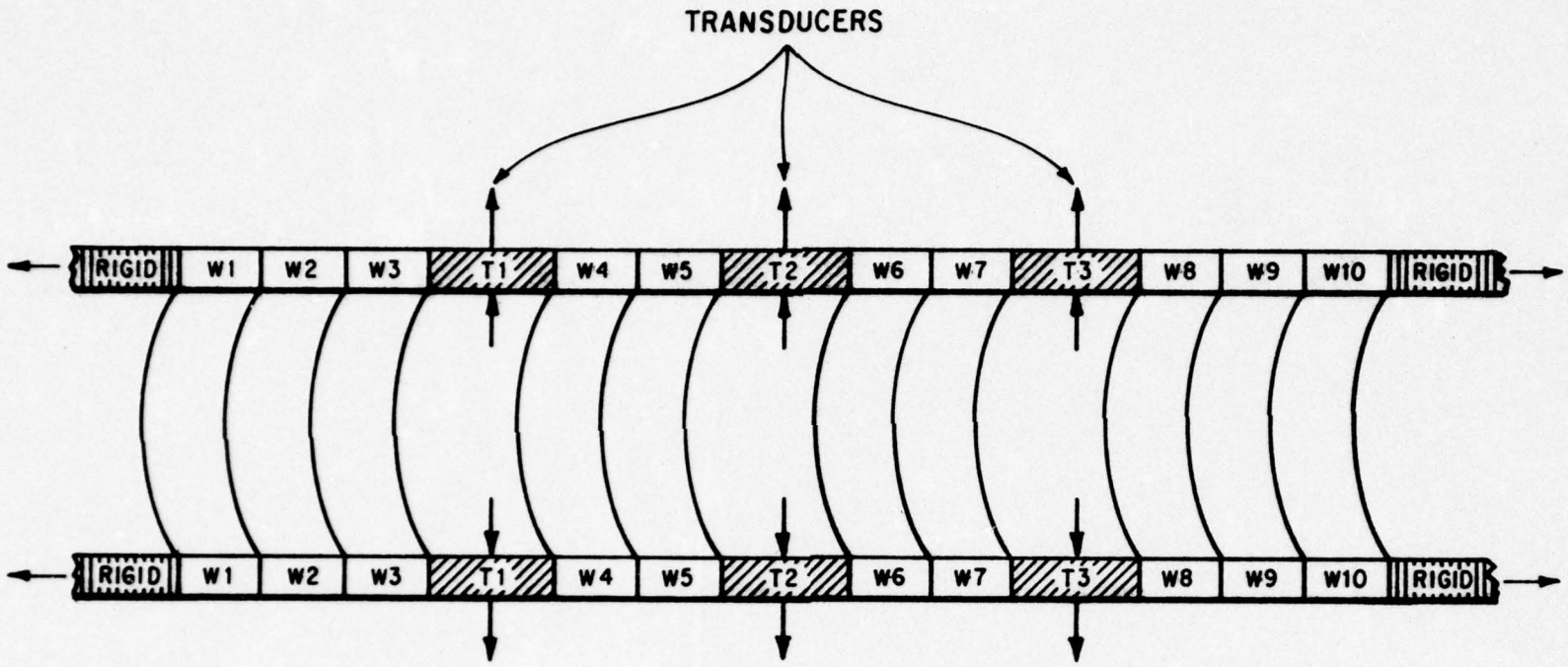

2 WATER RINGS/GAP
3 WATER RINGS/END

WATER RING MODEL FOR 3-RING ARRAY

FIGURE 1

$$\begin{bmatrix} F \end{bmatrix} = \begin{bmatrix} Z \end{bmatrix} \cdot \begin{bmatrix} V \end{bmatrix} \qquad (1)$$

$(M+N) \times 1 \qquad (M+N) \times (M+N) \qquad (M+N) \times 1$

$$\begin{bmatrix} V \end{bmatrix} = \begin{bmatrix} Z \end{bmatrix}^{-1} \cdot \begin{bmatrix} F \end{bmatrix} \qquad (2)$$

ARRAY EQUATIONS FOR MODEL WITH
M TRANSDUCER RINGS AND N WATER
RINGS

FIGURE 2

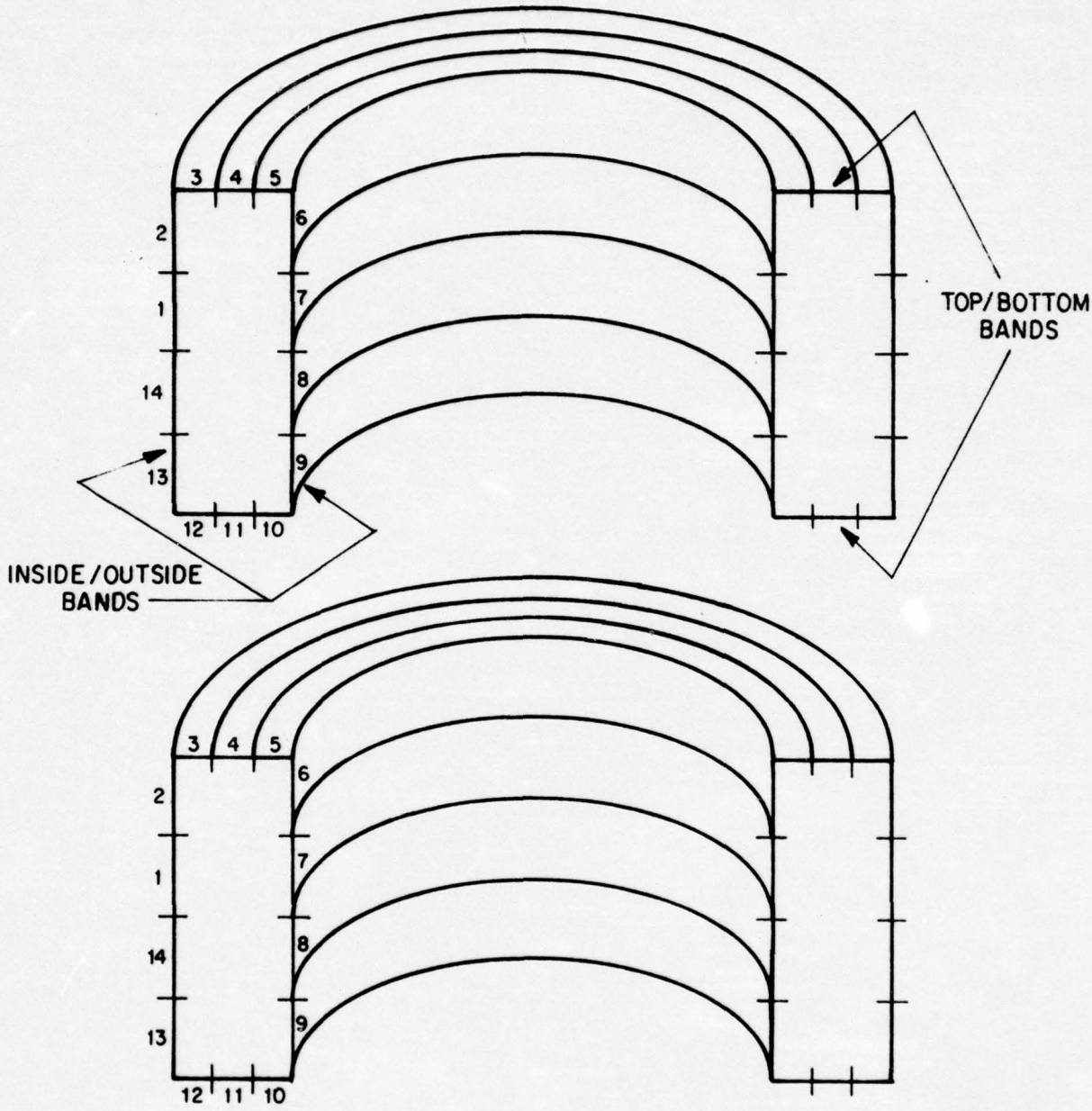

EACH RING IS ACOUSTICALLY SUBDIVIDED WITH 3 TOP/BOTTOM BANDS AND 4 INSIDE/OUTSIDE BANDS FOR ANALYSIS USING HELMHOLTZ INTEGRAL PROGRAM.

CROSS SECTION OF 2-RING ARRAY

FIGURE 3

PORTION OF MUTUAL IMPEDANCE
MATRIX FOR FOUR RING ARRAY
(Helmholtz Integral Method)
Frequency = 4 kHz

Top/Bottom Bands/Ring=I	Inside/Outside Bands/Ring=J	R_{11}	R_{12}	X_{11}	X_{12}
2	2	164	213	5586	2440
2	4	134	174	5170	2215
2	6	128	167	5076	2167
2	8	126	164	5040	2150
4	6	117	152	4972	2062
4	8	113	147	4918	2032

kg/sec

FIGURE 4

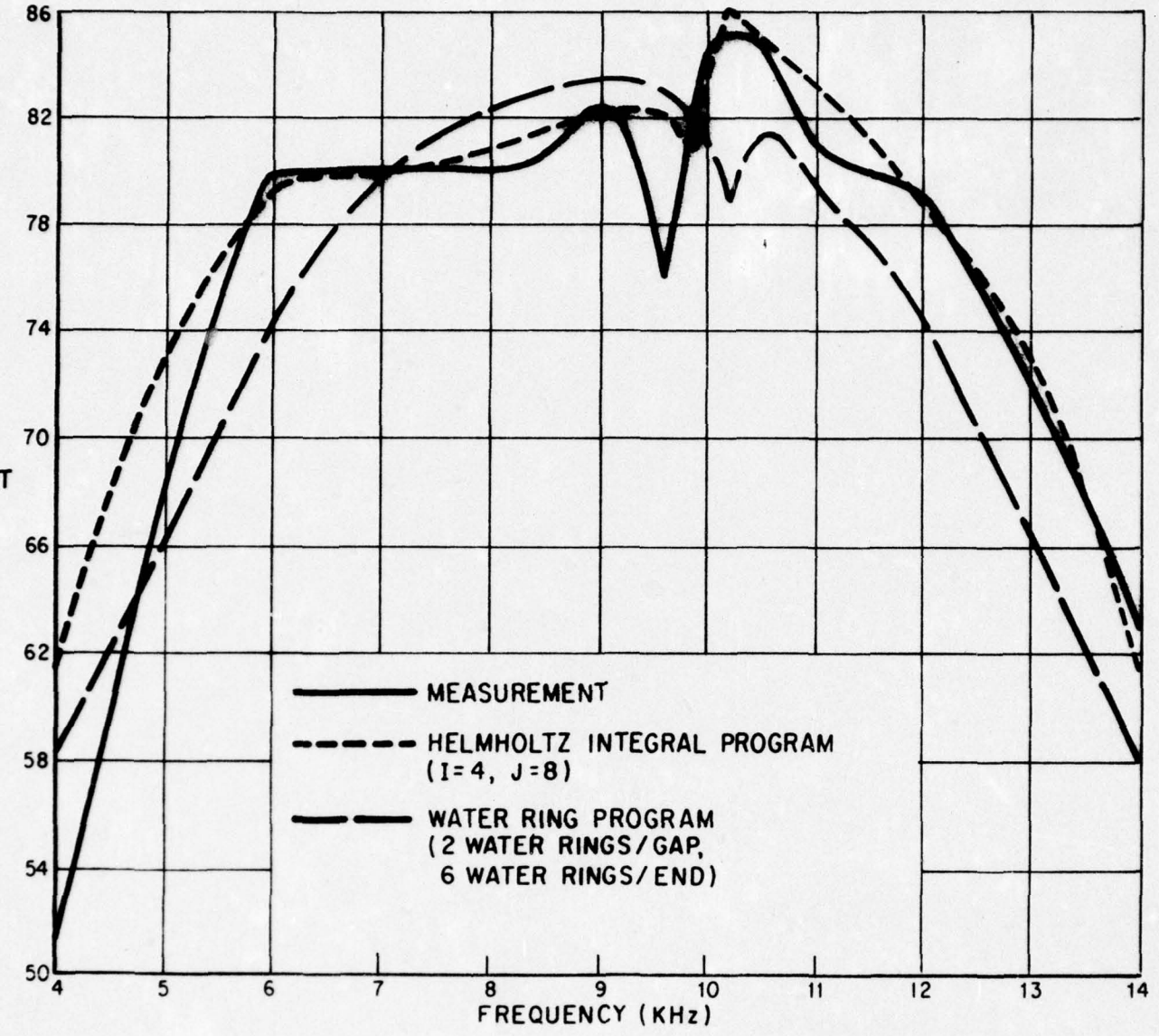

TRANSMIT CURRENT RESPONSE FOR A 4-RING ARRAY

FIGURE 5

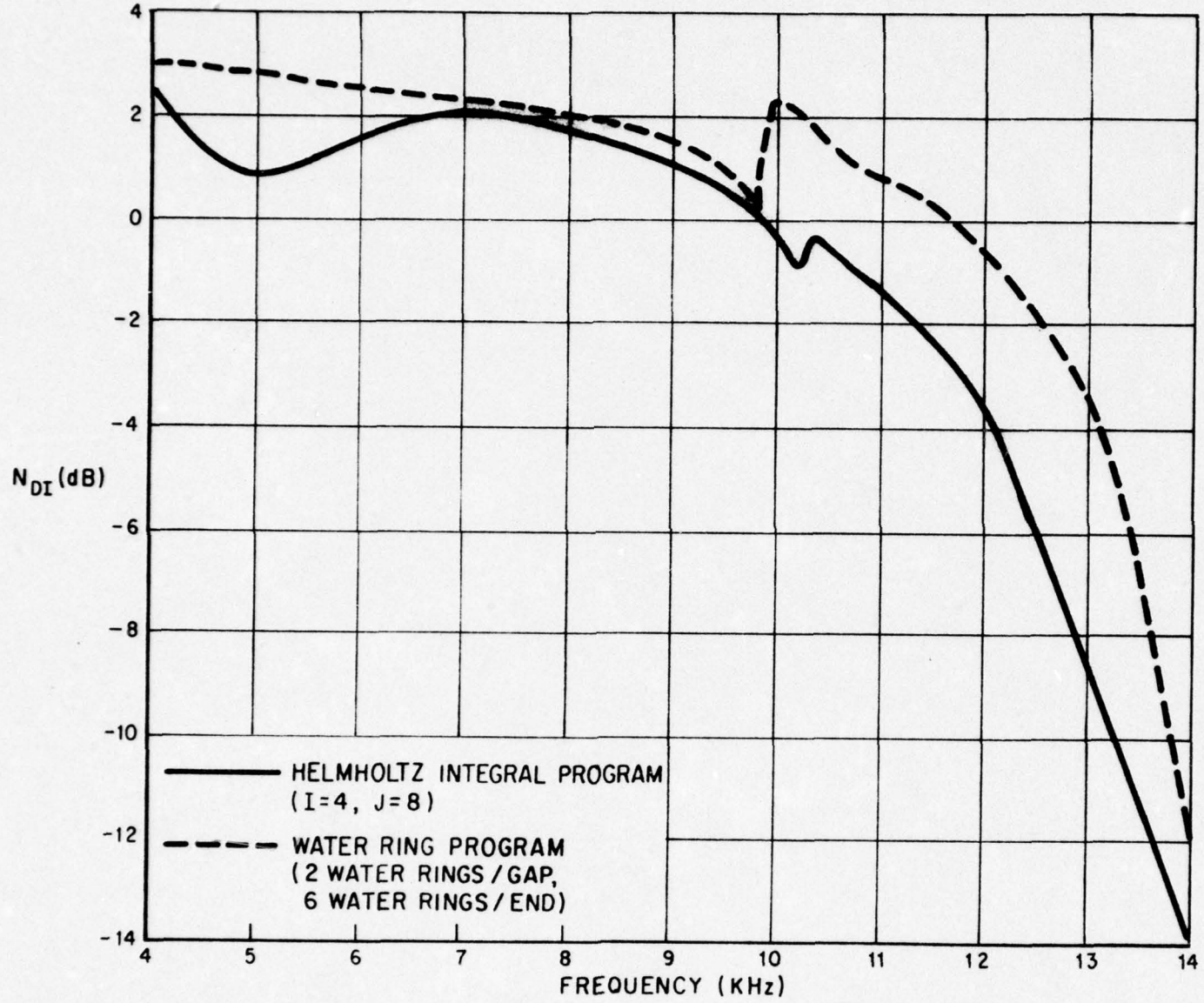

DIRECTIVITY INDEX FOR A 4-RING ARRAY

FIGURE 6

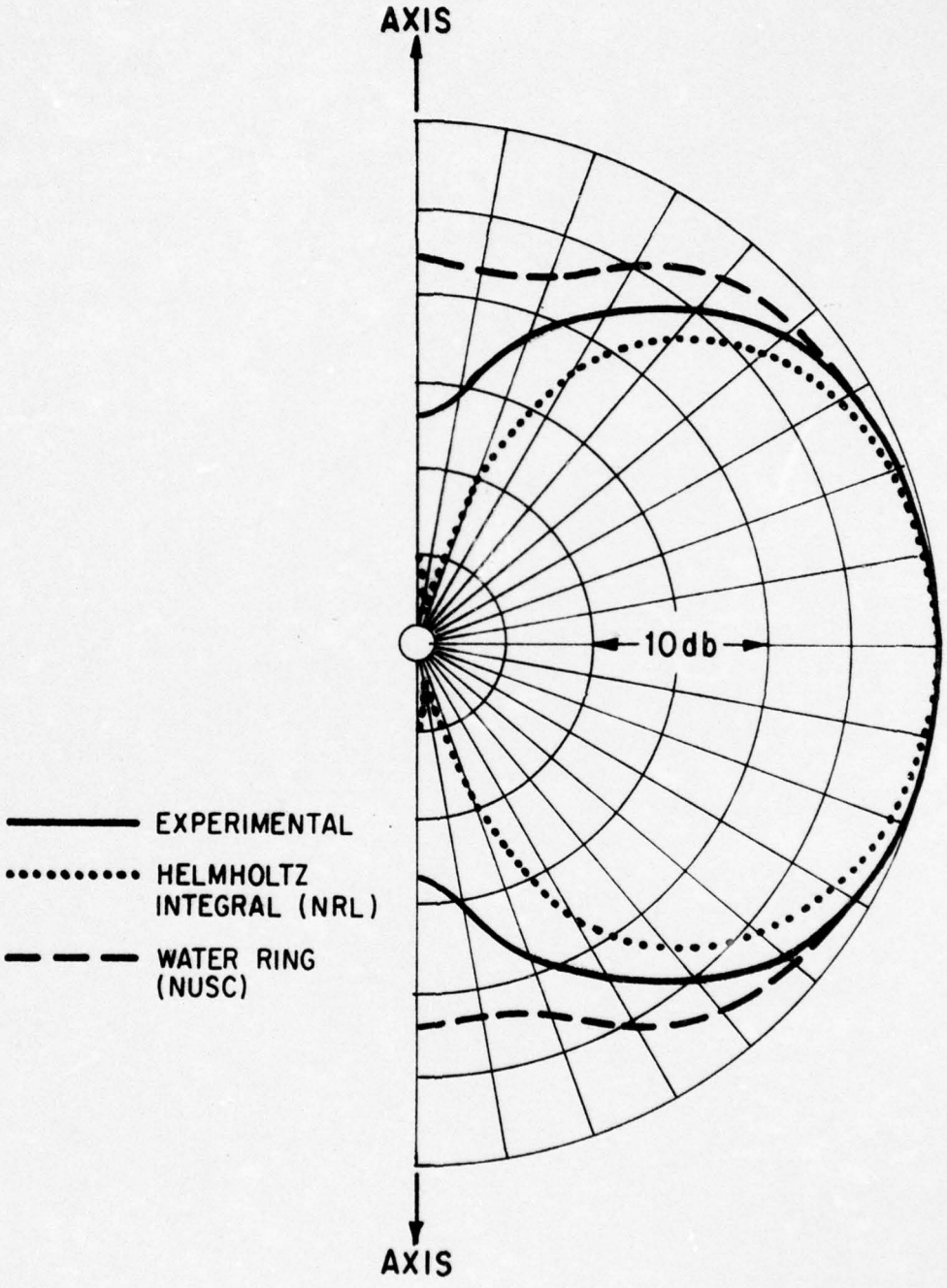

RADIATED PATTERNS FOR 4-RING ARRAY – 6 KHz

FIGURE 7

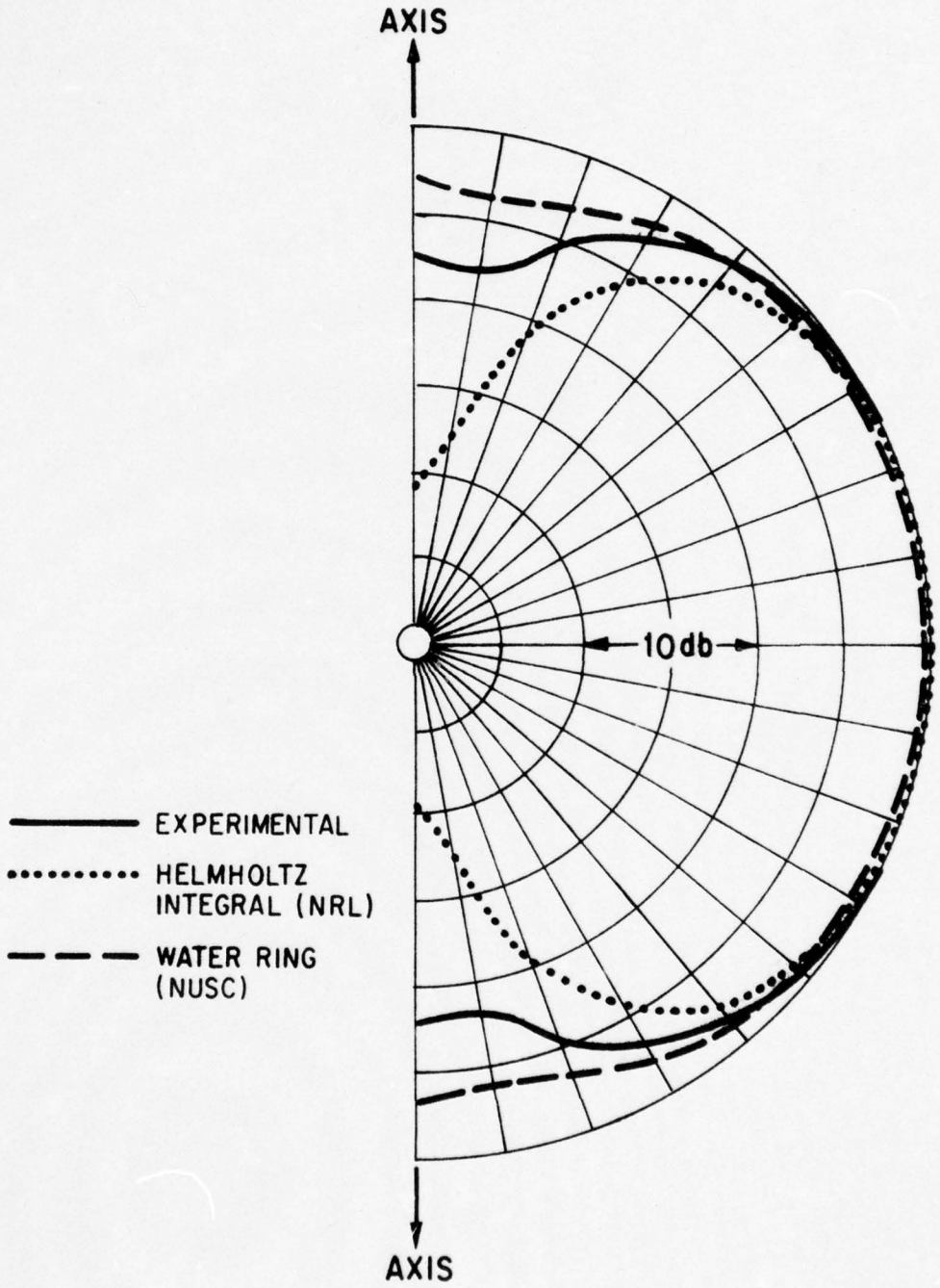

RADIATED PATTERNS FOR 4-RING ARRAY – 9.5 KHz

FIGURE 8

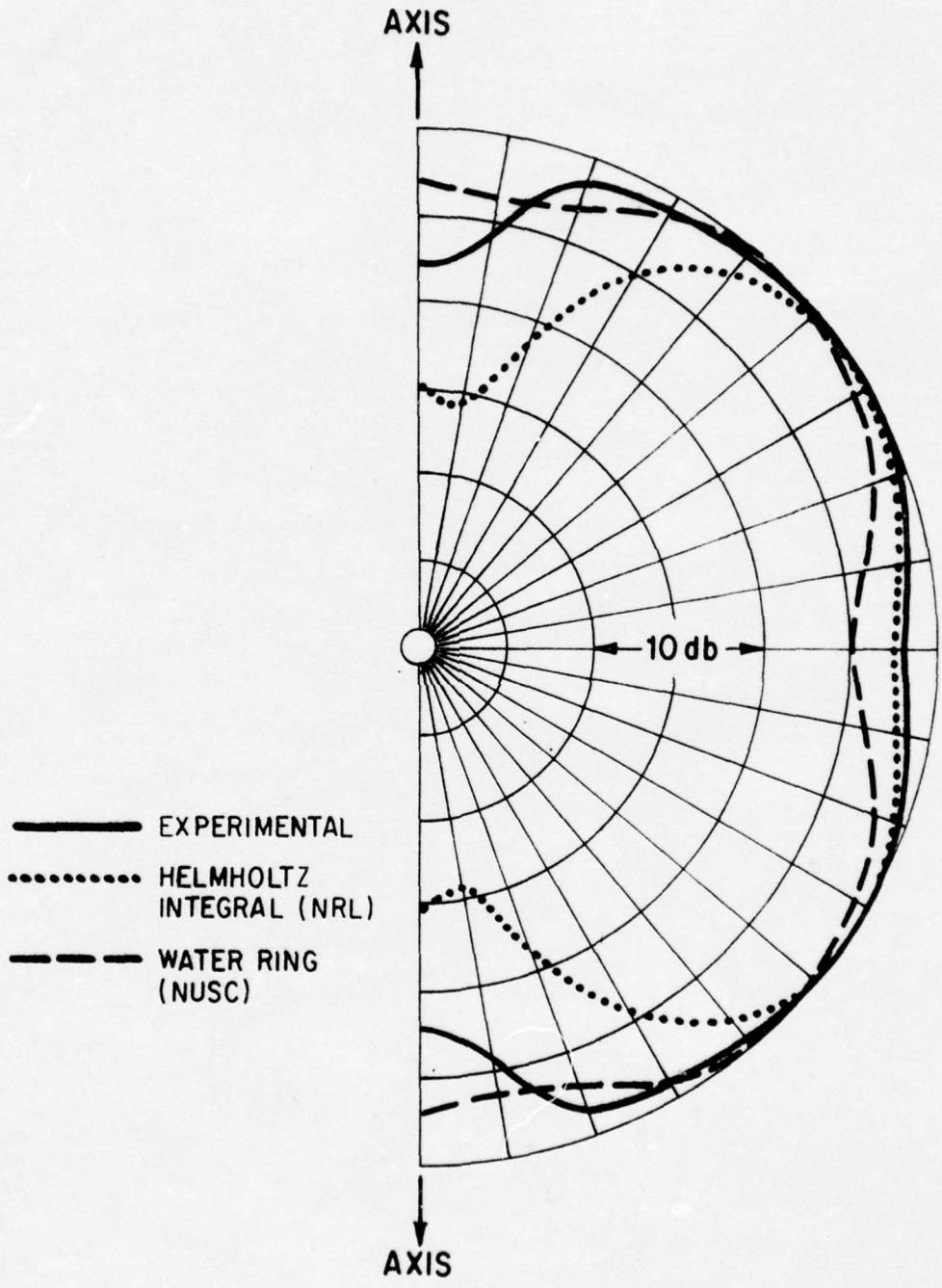

RADIATED PATTERNS FOR 4-RING ARRAY – 12 KHz

FIGURE 9

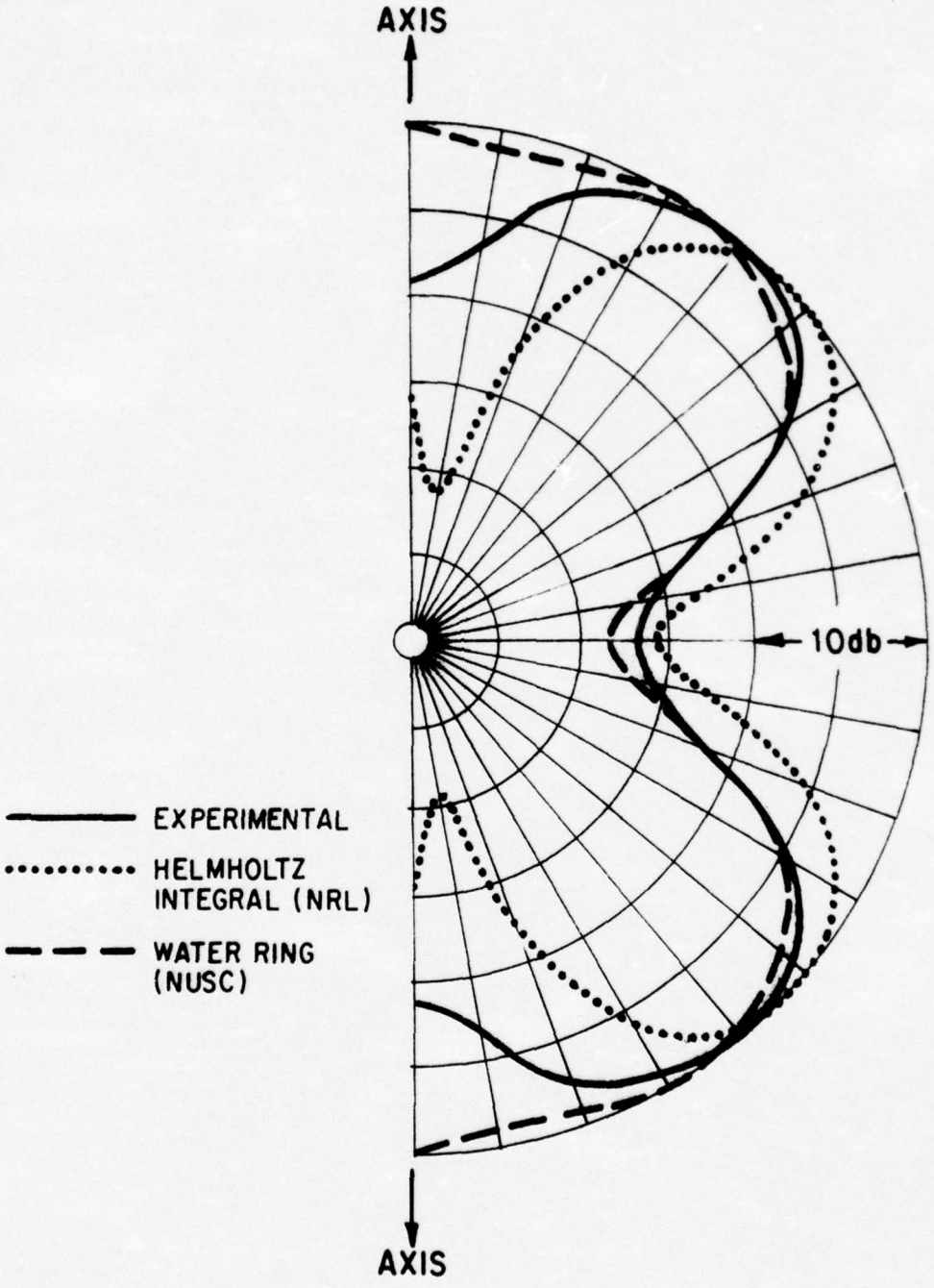

RADIATED PATTERNS FOR 4-RING ARRAY — 14 KHz

FIGURE 10

AREAS OF USEFULNESS OF
HELMHOLTZ INTEGRAL AND WATER
RING PROGRAMS

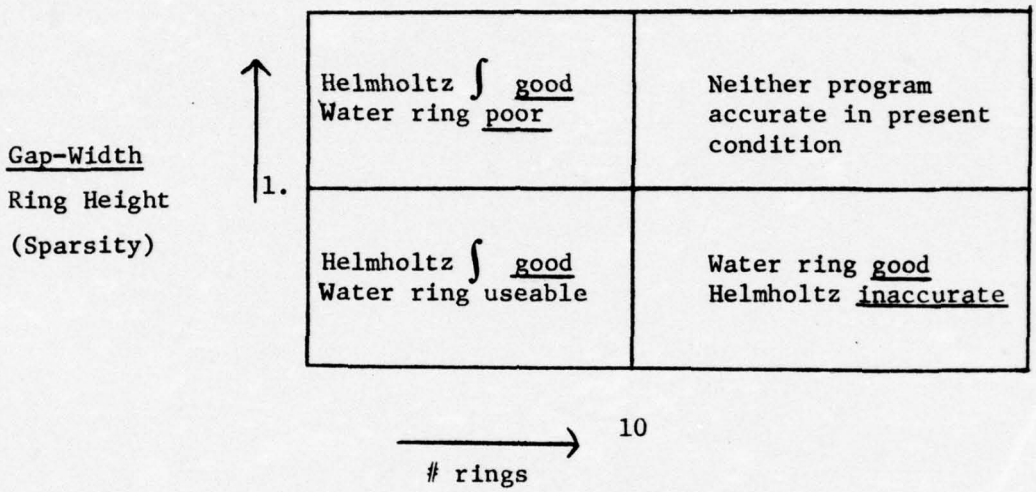

FIGURE 11

MECHANICAL ACOUSTIC RADIATOR

M.L. Rumerman
Naval Ship Research and Development Center

This paper outlines the analysis of a mechanically-driven acoustic radiator. The ultimate goal is to provide a guide by which the device can be designed to operate broadband over a specified frequency range.

The radiator consists of a thin cylindrical shell and the mechanical excitation is generated by diametrically-opposed flatted rollers (Figure 1), which are made to traverse the circumference of the inner surface of the shell at constant angular speed. When a flat comes down upon the shell, an impulsive force is delivered, and the vibration thus generated results in sound radiated into the acoustic medium.

Were the rollers to move without slipping on the shell, only discrete frequencies would be generated, due to the kinematic regularity. Slipping results in a continuous spectrum. Let $\overline{\Delta}$ be the average interval between successive impacts. Then $\overline{\Delta} = \Delta + \overline{\zeta}$ where Δ is the deterministic time between impacts (dependent upon geometry and speed) and $\overline{\zeta}$ is the average slip time between successive impacts. It can be shown that when $\overline{\zeta} > \frac{1}{f_{min}}$, where f_{min} is the lowest frequency of interest, then the impacts can be considered uncorrelated and the resulting spectral density of radiated power, $S(\omega)$, can be given by

$$S(\omega) = \frac{F(\omega)}{\overline{\Delta}} \qquad \omega > 2\pi f_{min}$$

where $F(\omega)$ is the average spectral density of total energy radiated by a single impact.

$F(\omega)$ can be calculated by a modal analysis of the shell vibration and radiation. It is found that the spectral density of the excitation will be broadband when $2\pi f_{max} \varepsilon < 1$, where f_{max} is the highest frequency of interest and ε is the duration of an impact. The radiated power spectrum will then be broadband if the shell can be made to respond uniformly over the frequency range.

Figure 2 represents idealized modal transfer functions - from excitation spectrum to radiated power spectrum - as a function of frequency. Assuming that the peaks are equal and that adjacent curves cross at their mutual 3 dB down points and that adjacent modes are independent, it can be shown that the effect is to give a broadband response over the frequency range, as indicated by the dashed line. While it is impossible to design a shell having the acoustical features described above, something approaching it should be feasible and would provide efficient broadband response.

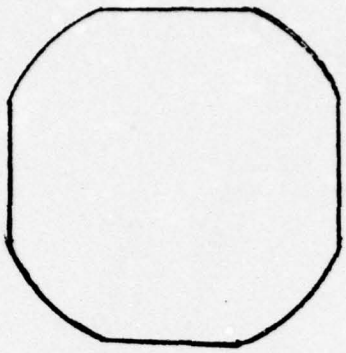

FIGURE 1

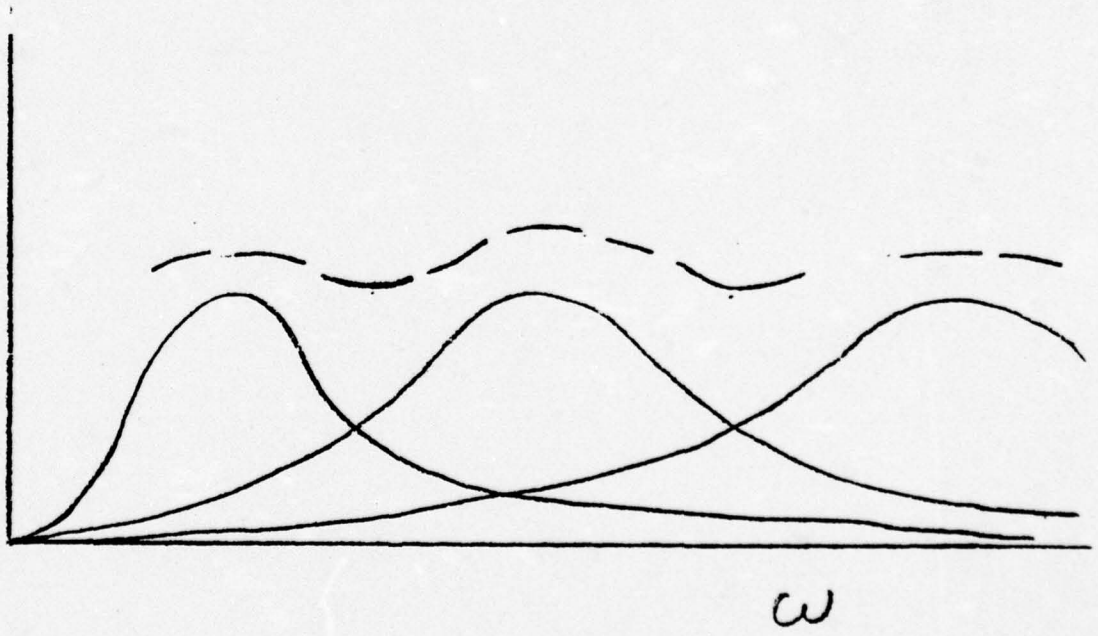

FIGURE 2

TWO METHODS FOR PREDICTING ARRAY DIRECTIVITY INDEX

D. T. Porter
Naval Underwater Systems Center

ABSTRACT

The first method is referred to as the pattern method. Pertinent equations are:

$$N_{DI} = 10 \log_{10}\left(\frac{\text{Intensity on M.R.A.}}{\text{Average Intensity}}\right) \quad (1)$$

and

$$\text{Average Intensity} = I_{AV} = \frac{\int_o^{2\pi}\int_o^{\pi} I(\theta,\phi) r^2 \sin\theta \, d\theta \, d\phi}{4\pi r^2} \quad (2)$$

Unfortunately, to accurately evaluate the integral of equation (2), a great many pattern points may be needed.

The second method is referred to as the radiated power method. If the array under consideration is a receiving array, we must mathematically concoct an analogous and reciprocal transmitting array. Pertinent equations are

$$\text{Source Level} = 71.6 + N_{DI} + 10 \log (\text{Acoustic Power}) \quad (3)$$

and

$$\text{Acoustic Power} = \sum_{j=1}^{n} R_j V_j^2 \quad (4)$$

We may find N_{DI} from (3) if we know the source level on the MRA, and the acoustic power radiated from each transducer. Knowledge of the source level requires the array's acoustic response at only one point, instead of many as in the pattern method. However, knowledge of the acoustic power requires solution of the array's coupled force - velocity - mutual coupling equations in order to get the radiation resistances and velocities

needed in equation (4). This in turn requires expressions for mutual coupling coefficients (Z_{ij}). The programming and debugging of these expressions may be very troublesome.

Provided the Z_{ij} can be obtained, the radiated power method gives exact results for N_{DI}. An example was shown where the computer time (Univac 1108) for a 1000 - element array's N_{DI} was 100 minutes for the pattern method and 22 minutes for the radiated power method.

COMPUTER TIME FOR UNIVAC 1108
TO CALCULATE N_{DI} VIA PATTERNS

$$T_{(min)} = \frac{N_p N_t}{36,000}$$

For 2-D Pattern, $N_p = N_\theta \cdot N_\phi$

$\therefore$

$$T_{(min)} = \frac{N_\theta N_\phi N_t}{36,000}$$

For $N_\theta = 180$, $N_\phi = 20$, and $N_t = 1000$

$T_{(min)} = 100$ minutes

(Same array required 22 minutes using

Radiated Power Method)

PATTERN METHOD OF OBTAINING N_{DI}

$$N_{DI} = 10 \log_{10}\left(\frac{I_{MRA}}{I_{AV}}\right) \tag{1}$$

$$I_{AV} = \frac{\int_0^{2\pi}\int_0^{\pi} I(\theta,\phi)\, r^2 \sin\theta \, d\theta d\phi}{4\pi r^2} \tag{2}$$

TYPICAL TWO DIMENSIONAL FAR FIELD PATTERN

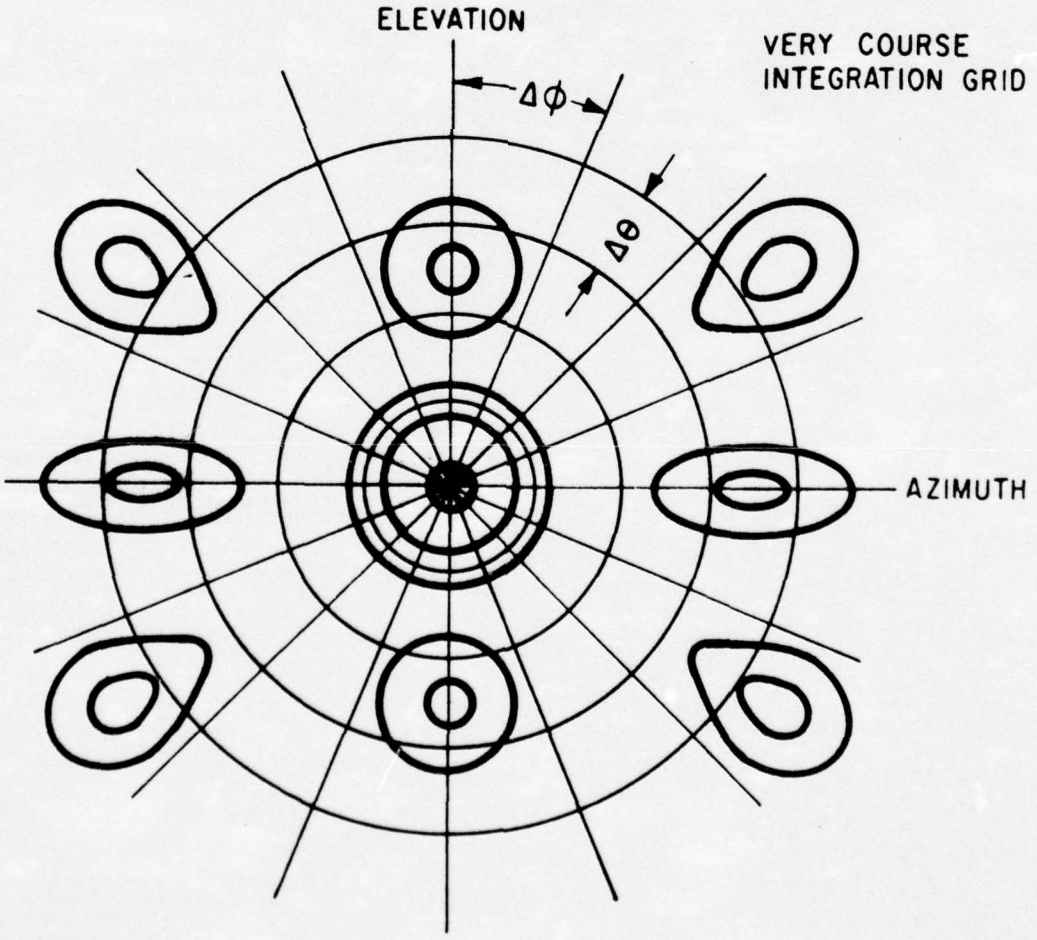

RADIATED POWER METHOD OF OBTAINING N_{DI}

$$L_s = 71.6 + N_{DI} + 10 \log P_{ACOUSTIC} \tag{3}$$

or

$$N_{DI} = L_S - 71.6 - 10 \log P_{ACOUSTIC} \tag{4}$$

$$P_{ACOUSTIC} = \sum_{j=1}^{n} P_{AC_j} = \sum_{i=1}^{n} R_j V_j^2 \tag{5}$$

$$R_i = \text{Real } (Z_{RAD_j}) \tag{6}$$

$$Z_{RAD_j} = \sum_{i=1}^{n} Z_{ij} \; V_i/V_j \tag{7}$$

$$\underset{1xN}{\left[F \right]} = \underset{NxN}{\left[Z \right]} \cdot \underset{1xN}{\left[V \right]} \tag{8}$$

$$\left[V \right] = \left[Z \right]^{-1} \cdot \left[F \right] \tag{9}$$

SOLUTION OF $\left[F \right] = \left[Z \right] \cdot \left[V \right]$

BY ITERATION

$$F_{TH_j} = \sum_{i=1}^{n} \underline{Z_{ij}} \; V_i, \quad \underline{Z_{ij}} = Z_{ij}, \quad i \neq j \tag{10}$$

$$\underline{Z_{ij}} = Z_{jj} + Z_{TH_j}, \quad i = j$$

$$F_{TH_j} = V_j \sum_{i=1}^{n} Z_{ij} \; V_i/V_j \tag{11}$$

$$V_j^{(n+1)} = \frac{F_{TH_j}}{\sum_{i=1}^{n} Z_{ij} \; \frac{V_i^{(n)}}{V_j^{(n)}}} \tag{12}$$

A FINITE ELEMENT APPROACH TO ACOUSTIC RADIATION FROM ELASTIC STRUCTURES

M. Knittel
J. Hunt
D. Barach
Naval Undersea Center

Past mathematical models of vibrating structures immersed in an infinite fluid medium have not been entirely successful because of the difficulties involved in combining the vibrational aspects of the structure with the acoustic radiation properties of the medium. In cases where this interaction has been successfully treated, such as in a combination of a finite element program (MARTSAM) with a Helmholtz Integral radiation program (CHIEF), the necessity for evaluating numerous and expensive integrals limits the usefulness of these methods. Near and far field pressures are calculated at a minimum number of field points for a limited number of frequencies. The approach that we have taken to acoustic radiation from elastic structures avoids this difficulty; calculation of the near and far fields for numerous frequencies is an inexpensive process and thus allows the calculation of the pressure at enough points to draw contour plots of the pressure field.

The problem chosen for analysis with this method was the behavior of a tangentially poled, piezoelectric, ceramic cylinder immersed in an infinite fluid medium (Figure 1). This free-flooded cylinder was chosen because it is a simple, axisymmetric body in which circular harmonics other than m=0 can easily be electrically excited; that is a voltage that varies as cosine mØ can be applied around the cylinder. These non-zero

harmonics are important in scattering from a single cylinder because all circular harmonics will be excited when the incident wave does not propagate down the symmetry axis. The non-zero harmonics are also important in the design of non-coaxial arrays of cylinders since interactions between them will excite non-zero harmonics of the individual cylinders.

Finite element techniques were used to model one-half of a double stave of the cylinder and the appropriate boundary conditions applied (Figure 2). Each nodal point has three displacement degrees of freedom and an electrical degree of freedom. The coordinate axes of the structure were transformed from rectangular to a cylindrical coordinate system and the degrees of freedom condensed down to an axisymmetric representation. Cosine mØ voltage dependence was applied around the cylinder, and cos mØ and sine mØ displacement dependence was assumed. Below 20 kHz, our calculations have shown that this reduction is valid.

The fluid immediately surrounding the cylinder was modeled using finite element techniques out to a sphere that just encloses the structure. This was done because for spherical surfaces, the acoustic radiation Green's function for steady-state problems separates when expanded in spherical harmonics. A closed form solution for the radiation impedance that is associated with each spherical harmonic can be found that consists of merely a ratio of Hankel functions. The finite element fluid sphere surface forces, pressures, and normal velocities can be expanded in approximations to spherical harmonics through a simple transformation to a finite set of spherical harmonic base vectors. The spherical harmonic components of the pressure at any point outside the finite element fluid

sphere can be calculated in terms of the sphere surface pressure components and ratios of two Hankel functions.

Forty-nine acoustic fluid elements were used to model one-quarter of the fluid sphere in the x-y plane (Figure 3); these axisymmetric elements are triangular in cross section with six nodes per element. Each node has one degree of freedom, the pressure. A connection or compatability matrix was formed that relates the normal displacements of the structure to the pressures in the fluid on the common surfaces. This gives a total of about 150 degrees of freedom. However, by solving the interior problems of the free vibrations of the combined structure - fluid sphere with zero sphere surface pressure, the number of degrees of freedom can be reduced down to about twenty-five. In addition, solving the equations in this manner avoids singularities that occur for frequencies near eigenfrequencies of the interior problem. Therefore, once the finite element mass and stiffness matrices are formed and assembled and the interior problem solved once, only matrices of the order of 25x25 need to be solved for each driving frequency. No acoustic radiation integrals are numerically evaluated, and the pressures at a large number of field points for numerous frequencies can be inexpensively calculated.

Figure 4. m=0 complex electrical impedance. The real part of the impedance is proportional to the acoustic power radiated into the water. Choosing a frequency of 3,000 Hz.

Figure 5. Structural displacements show breathing mode.

Figure 6. Vertical directivity pattern.

Figure 7. Near field pressure contour plot out to 0.4 meters at one time step.

Figure 8. Contour plot extending out into the far field to 3.6 meters. Far field begins at about 2.5 meters.

Figure 9. m=1 complex electrical impedance. In performing the experiments, it was found that fiberglassing the cylinder lowered the resonant frequencies. Difficulties were also encountered in measuring the magnitude and phase of the electrical impedance accurately while driving the cylinder in the non-zero circular harmonics. In addition, the material parameters used in our model are loss-less parameters whose values in some cases are probably not too accurate. All of this contributes to the discrepancies between theory and experiment. Look at 4,500 Hz.

Figure 10. Structural displacements show cosine 1Ø dependence.

Figure 11. Vertical directivity pattern.

Figure 12. Horizontal directivity pattern showing two nodes.

Figure 13. Near field pressure contour plot in Ø=0 plane showing central nodal line.

Figure 14. Pressure contour plot extending out into the far field.

Figure 15. m=2 complex electrical impedance.

Figure 16. Structural displacements at 8,750 Hz.

Figure 17. Vertical directivity pattern.

Figure 18. Horizontal directivity pattern showing four nodes.

Figure 19. Near field pressure contour plot in Ø=0 plane again showing central nodal line.

Figure 20. Pressure contour plot extended out into the far field.

The next application for which we hope to use this method is the receive or scattering problem using a free-flooded cylinder or some other structure. We also hope that this formulation will offer a feasible method to solve the combined equations of motion in the time domain. In addition, we will probably use this method to design a free-flooded cylinder for optimum performance. We are also looking at new and more informative ways to display the generated data, perhaps such as a movie of lines or surfaces of constant pressure that change with time and use continuously varying colors to represent magnitudes of pressure. In addition, we are trying display methods that will show both the structural displacements and the pressure field and how they vary with time in one changing display.

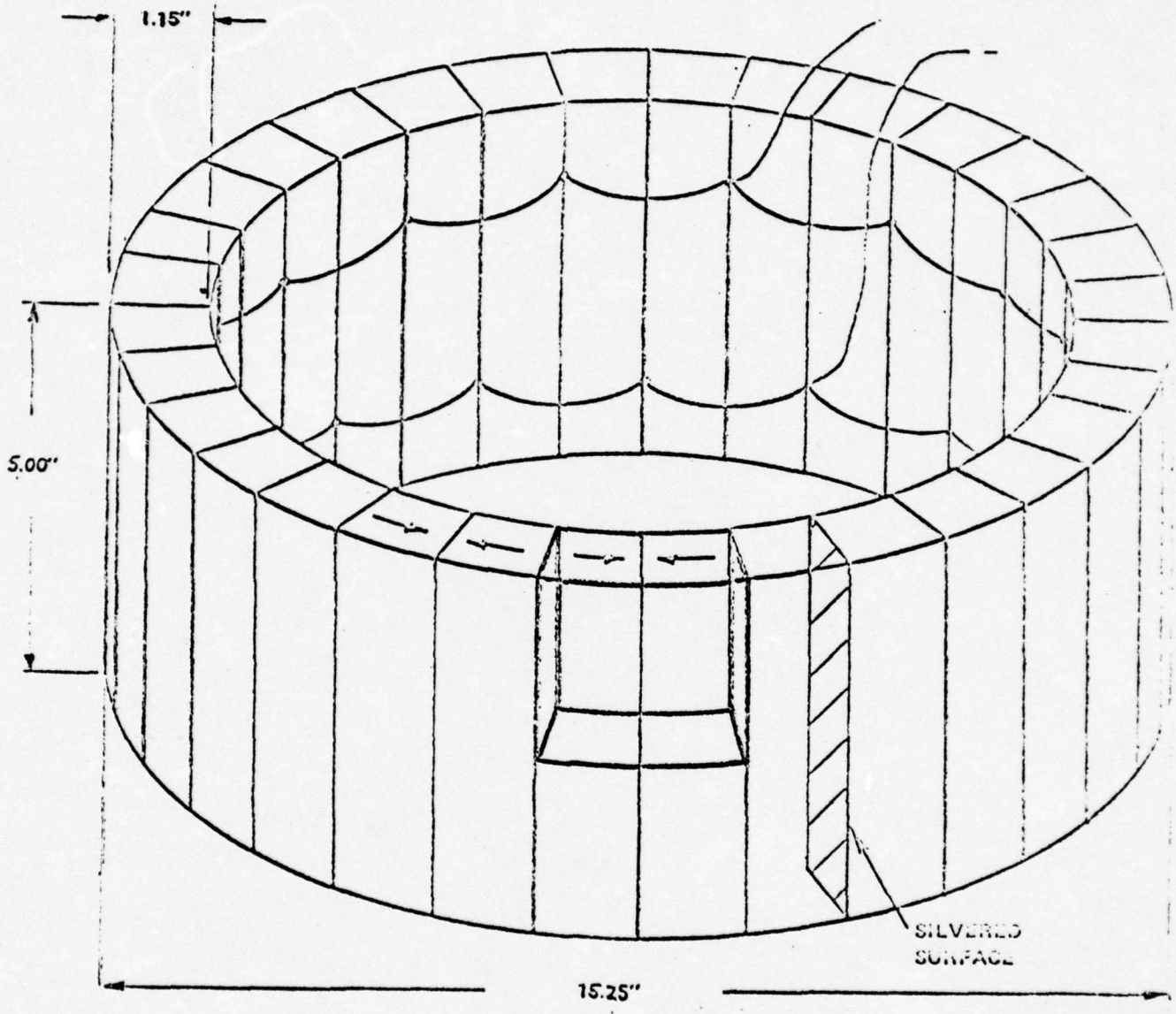

FREE-FLOODED CYLINDER

FIGURE 1

noc

FINITE ELEMENT IDEALIZATION FOR ONE-HALF DOUBLE STAVE OF CYLINDER

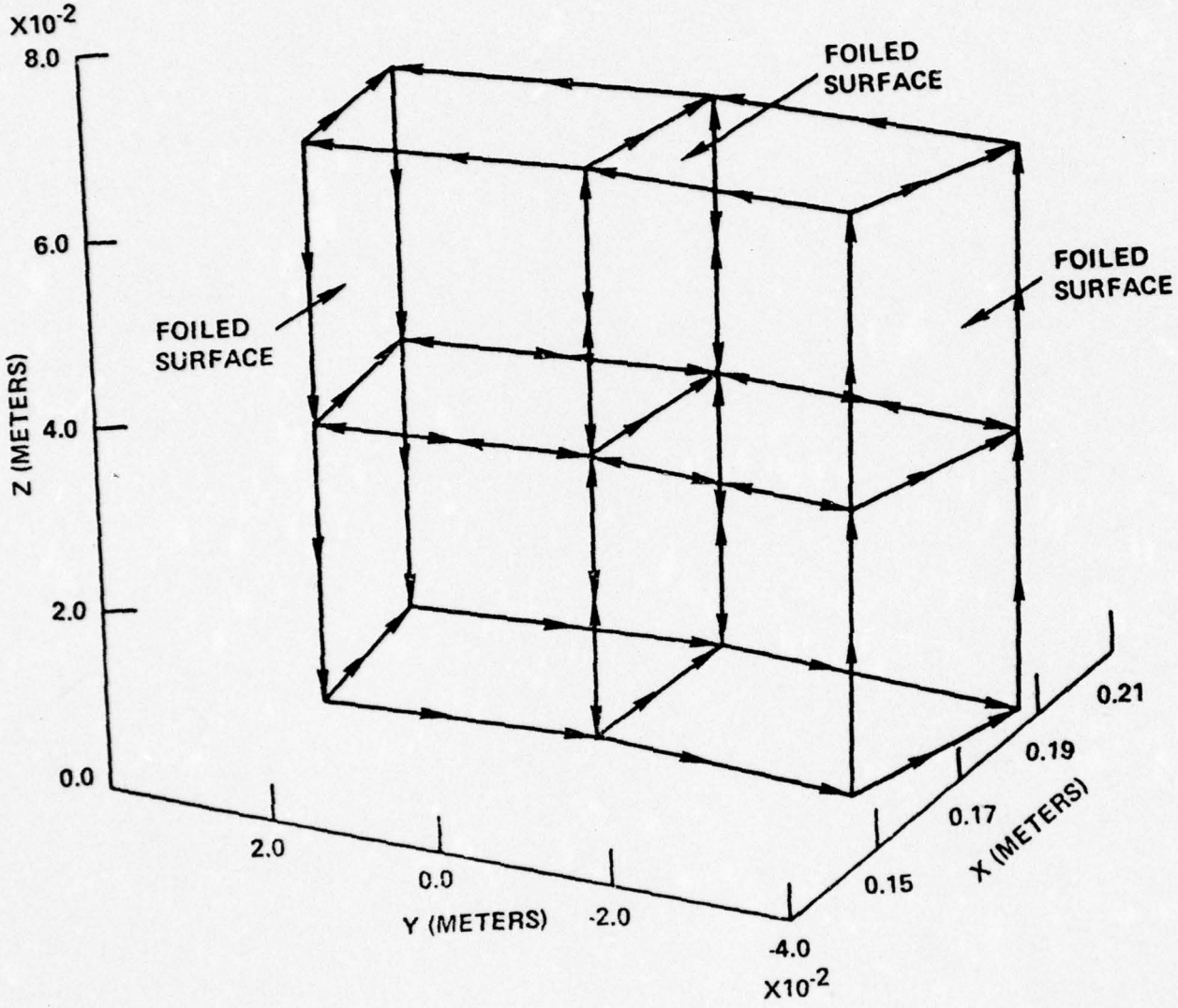

FIGURE 2

NOC

FINITE ELEMENT IDEALIZATION FOR ONE-QUARTER OF THE ACOUSTIC SPHERE WITHOUT THE STRUCTURE

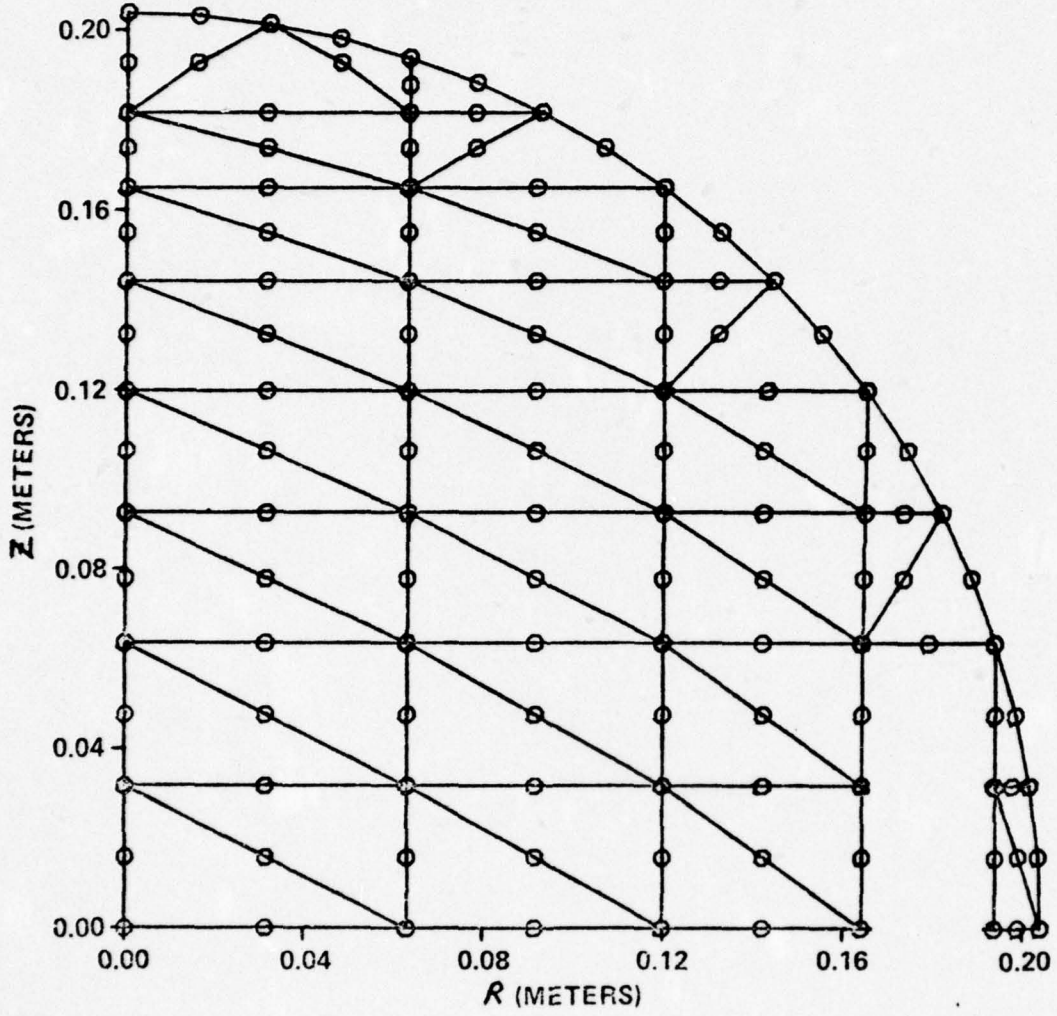

FIGURE 3

NUC

IN WATER COMPLEX ELECTRICAL IMPEDANCE PLOT

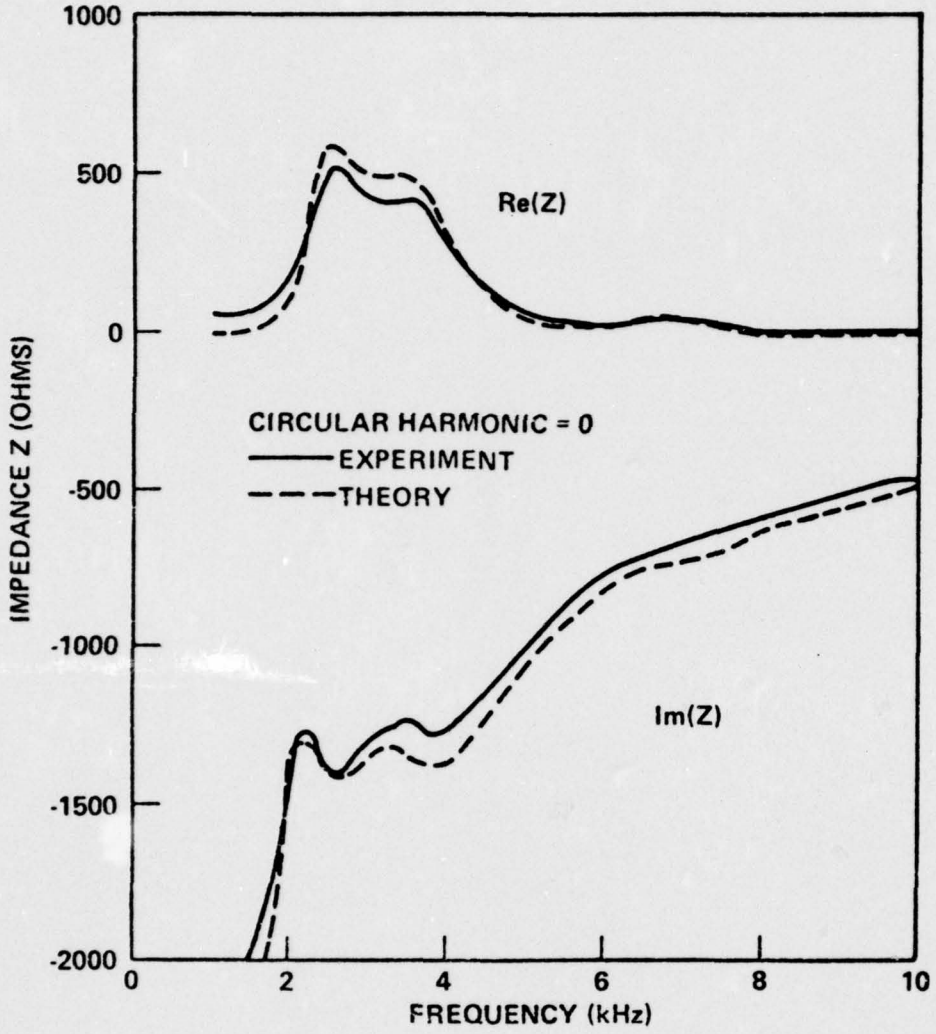

FIGURE 4

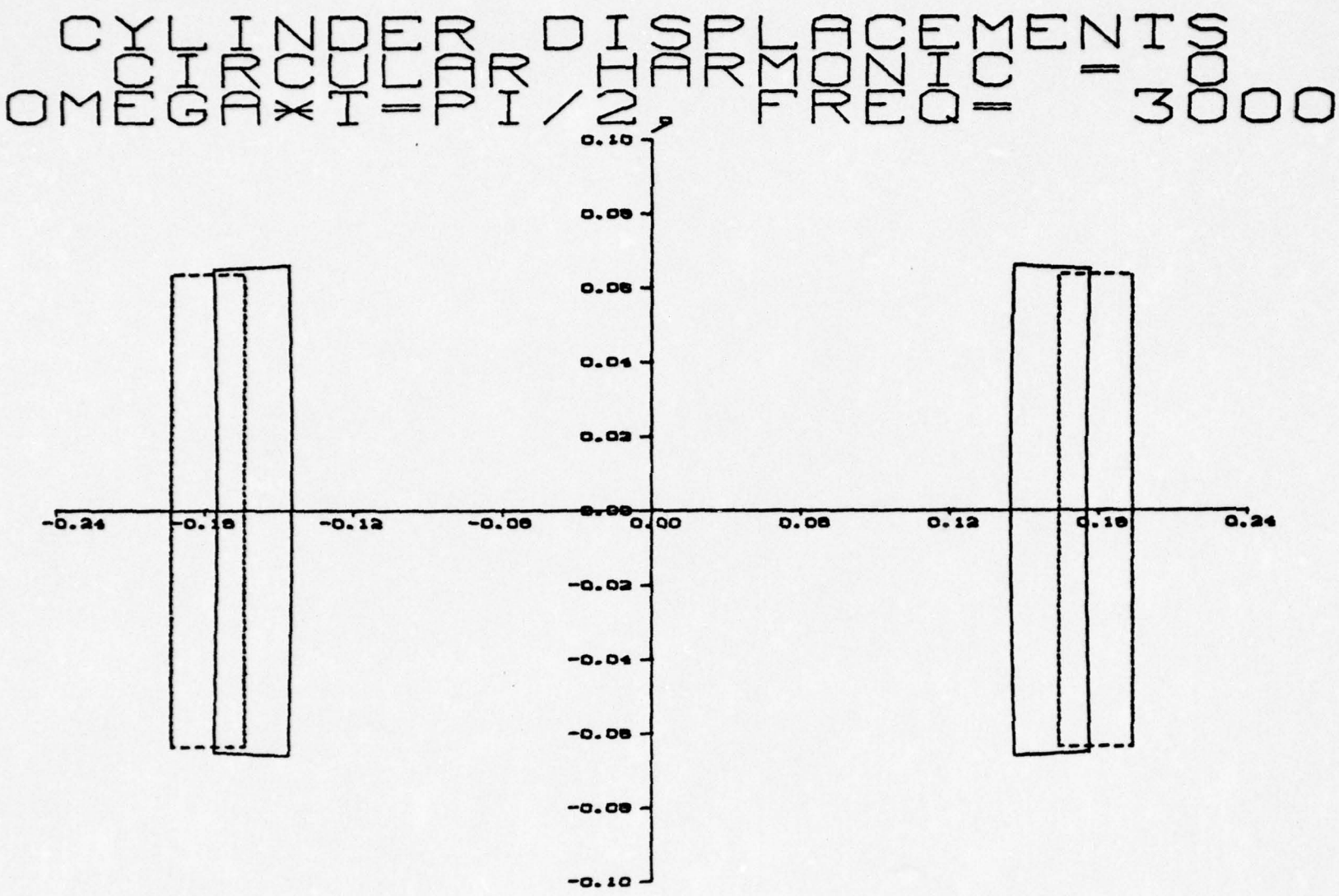
CYLINDER DISPLACEMENTS
CIRCULAR HARMONIC = 0
OMEGA*T=PI/2, FREQ= 3000
0.10
0.08
0.06
0.04
0.02
0.00
-0.02
-0.04
-0.06
-0.08
-0.10
-0.24
-0.18
-0.12
-0.06
0.00
0.06
0.12
0.18
0.24

FIGURE 5

noc

VERTICAL DIRECTIVITY PATTERN

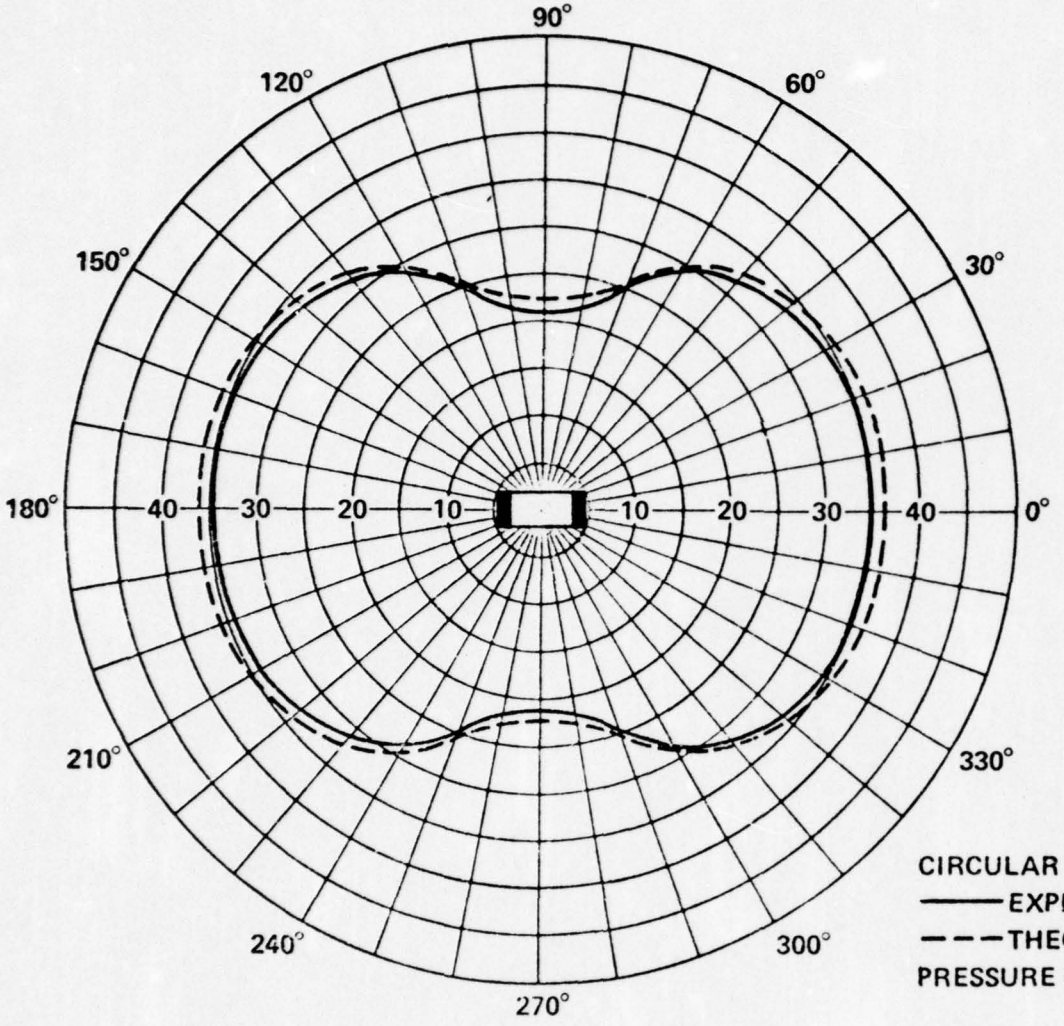

CIRCULAR HARMONIC = 0
——— EXPERIMENT AT 3000 Hz
– – – THEORY AT 3000 Hz
PRESSURE UNIT = 1 dB re 1 μbar/volt at 1 meter

FIGURE 6

nuc

RADIATED PRESSURE PATTERN FROM A TANGENTIALLY POLED CYLINDER (NEAR FIELD)

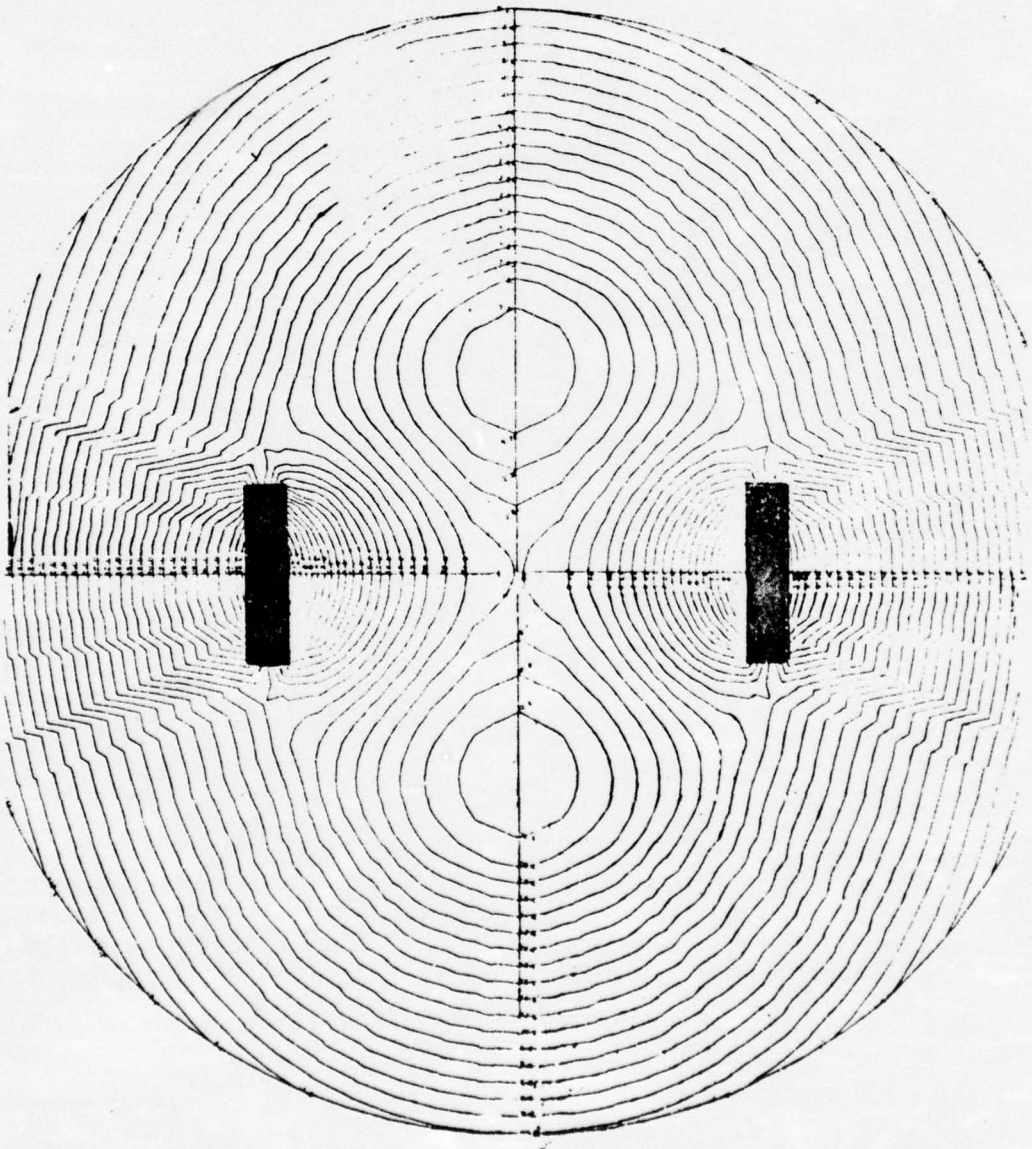

CIRCULAR HARMONIC = 0
FREQUENCY = 3000 Hz
WT = $\pi/2$
PRESSURE UNIT = 1 NEWTON/(METER)^2

FIGURE 7

NUC

RADIATED PRESSURE PATTERN FROM A TANGENTIALLY POLED CYLINDER (FAR FIELD)

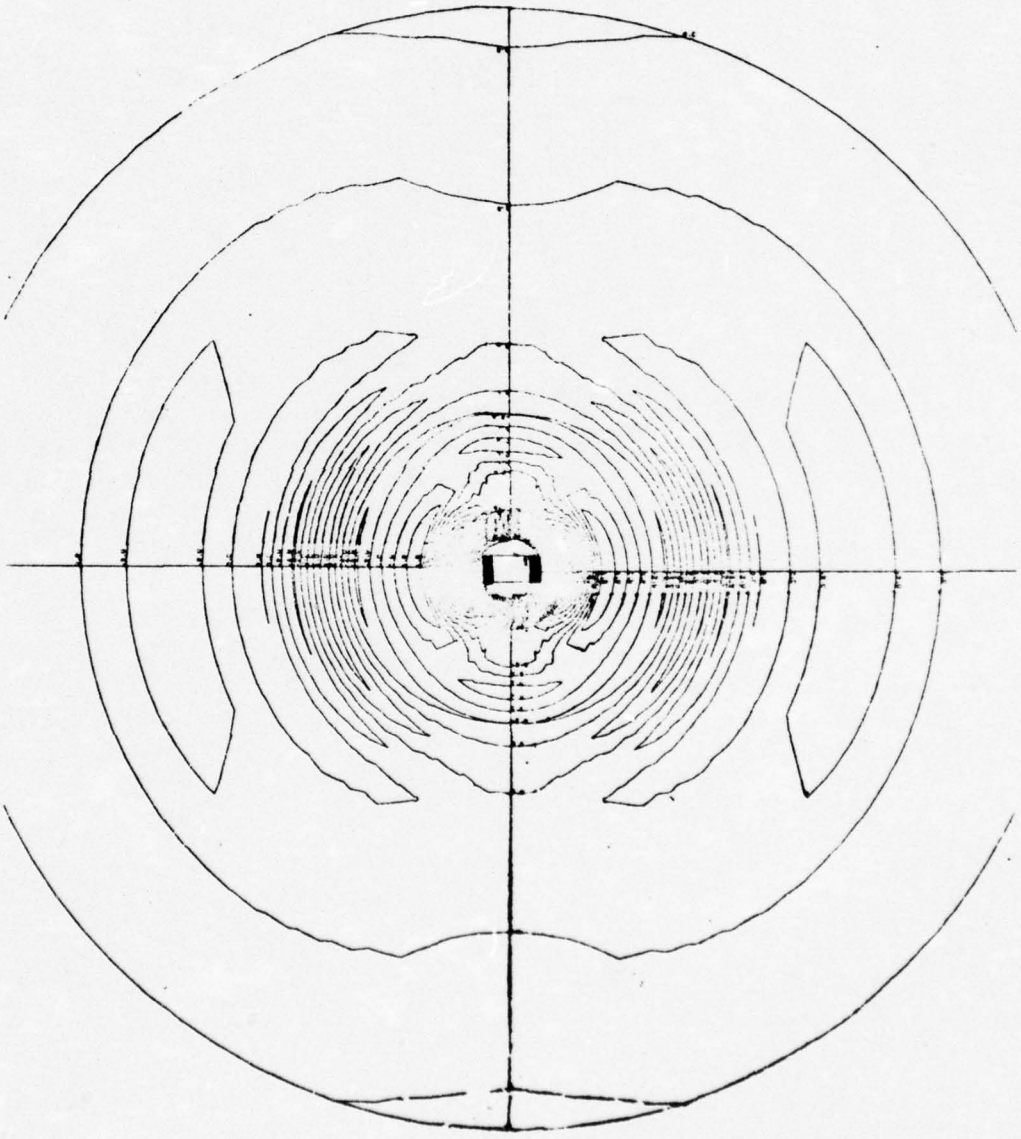

CIRCULAR HARMONIC = 0
FREQUENCY = 3000 Hz
WT = $\pi/2$
PRESSURE UNIT = 1 NEWTON/(METER)^2

FIGURE 8

#2

noc

IN WATER COMPLEX ELECTRICAL IMPEDANCE PLOT

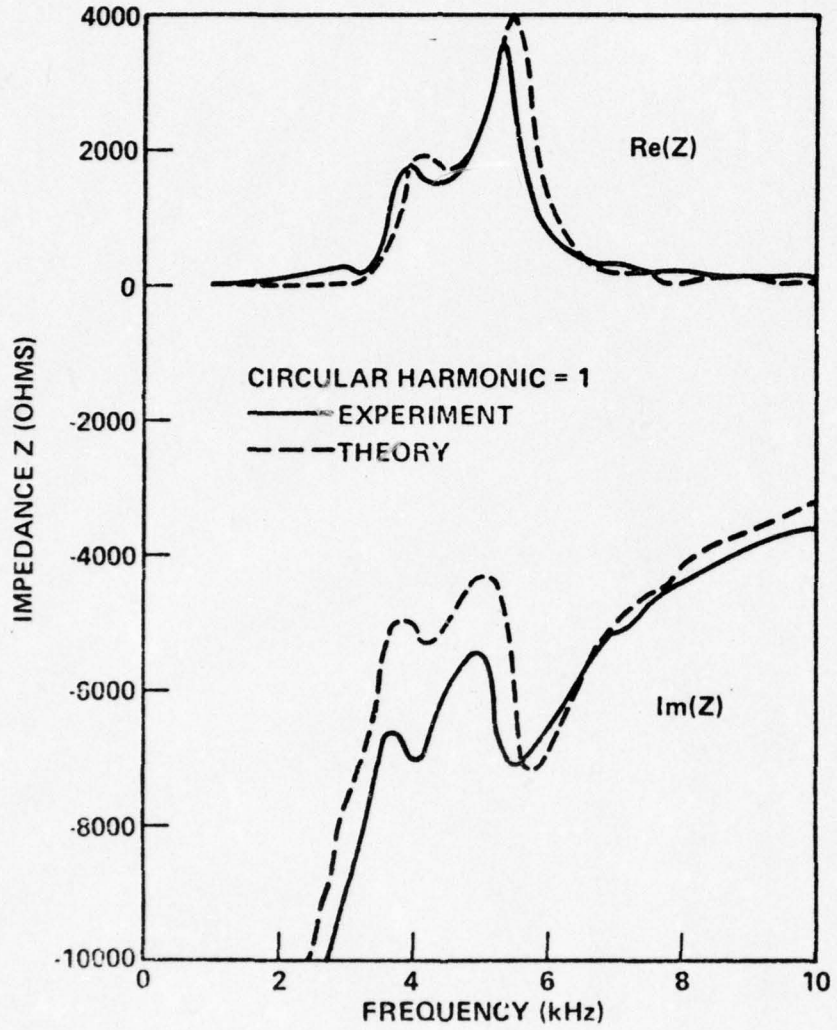

FIGURE 9

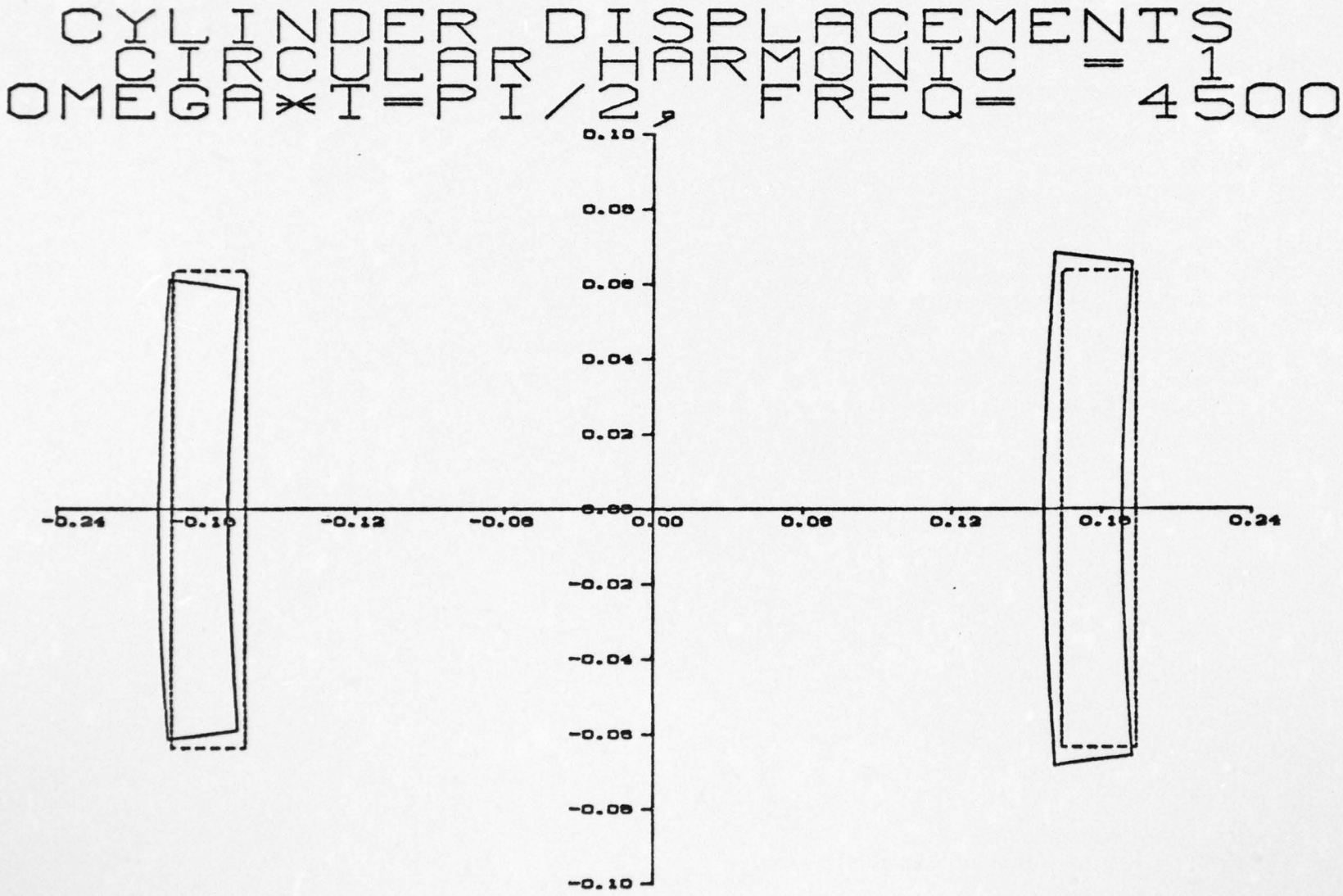
CYLINDER DISPLACEMENTS
CIRCULAR HARMONIC = 1
OMEGA*T=PI/2, FREQ= 4500
0.10
0.08
0.06
0.04
0.02
0.00
-0.02
-0.04
-0.06
-0.08
-0.10
-0.24
-0.18
-0.12
-0.06
0.00
0.06
0.12
0.18
0.24

FIGURE 10

VERTICAL DIRECTIVITY PATTERN

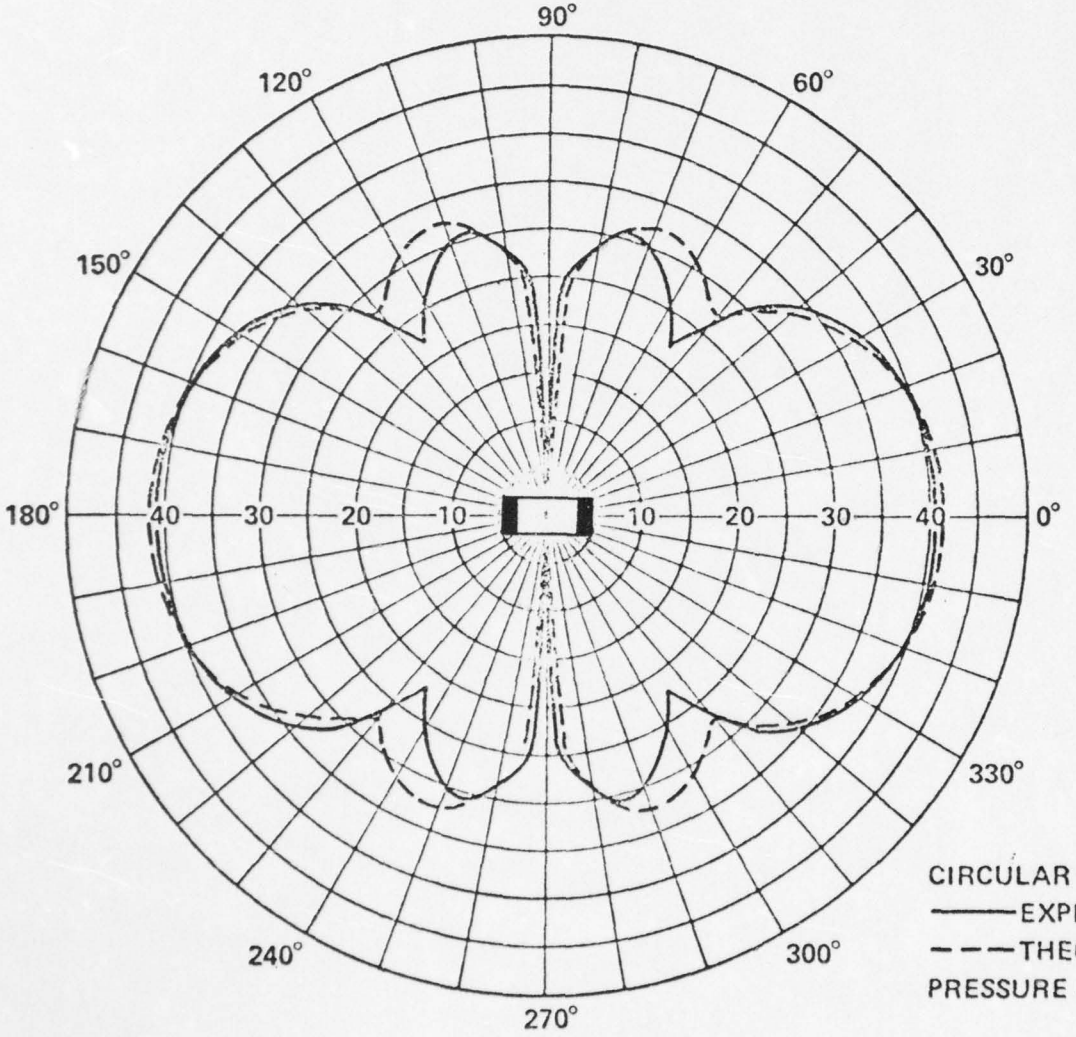

CIRCULAR HARMONIC = 1

——— EXPERIMENT AT 4250 Hz

– – – THEORY AT 4500 Hz

PRESSURE UNIT = 1 dB re 1 μbar/volt at 1 meter

HORIZONTAL DIRECTIVITY PATTERN

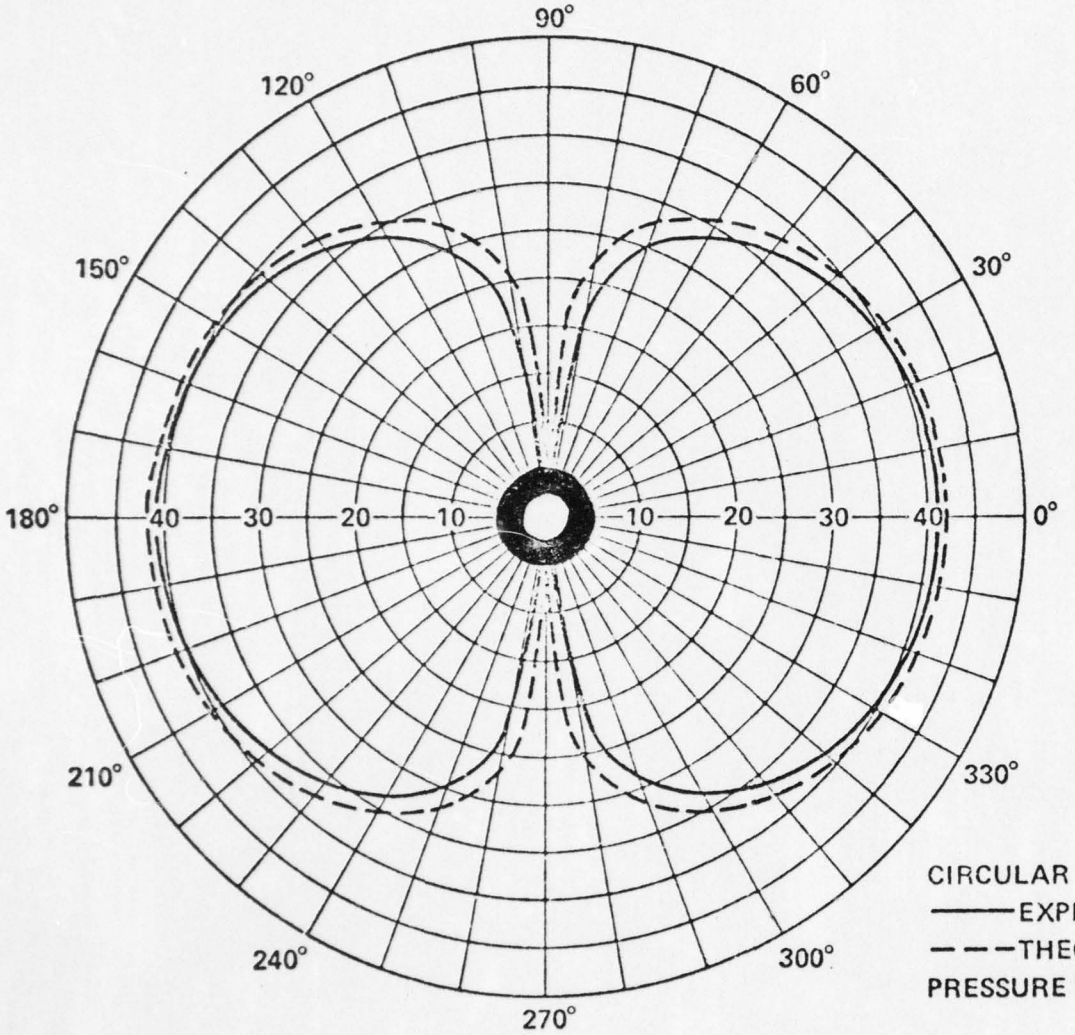

CIRCULAR HARMONIC = 1
——— EXPERIMENT AT 4250 Hz
– – – THEORY AT 4500 Hz
PRESSURE UNIT = 1 dB re 1 μbar/volt at 1 meter

FIGURE 12

NUC

RADIATED PRESSURE PATTERN FROM A TANGENTIALLY POLED CYLINDER (NEAR FIELD)

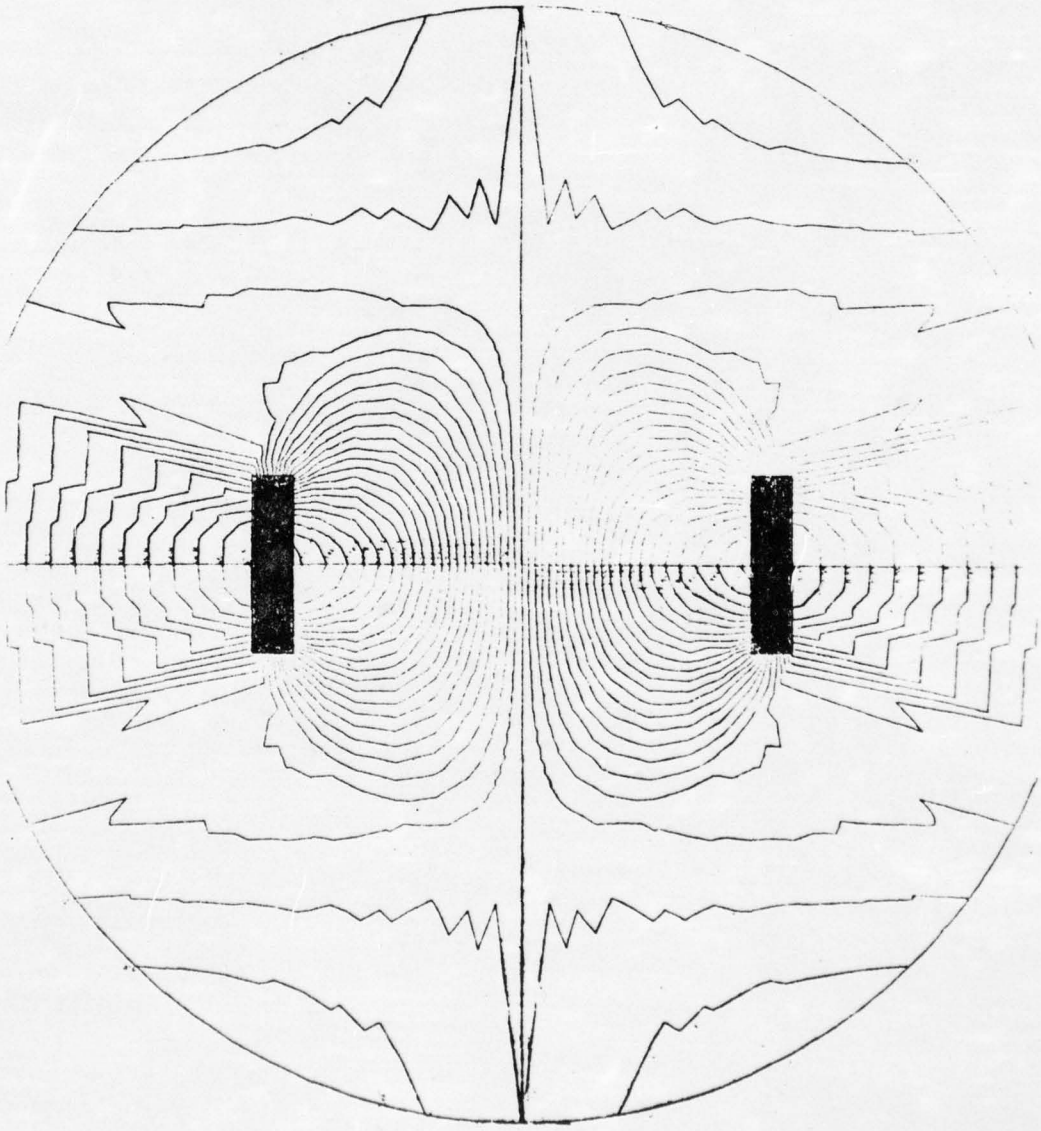

CIRCULAR HARMONIC = 1
FREQUENCY = 4500 Hz
WT = $\pi/2$
PRESSURE UNIT = 1 NEWTON/(METER)^2

FIGURE 13

#5

NUC

RADIATED PRESSURE PATTERN FROM A TANGENTIALLY POLED CYLINDER (FAR FIELD)

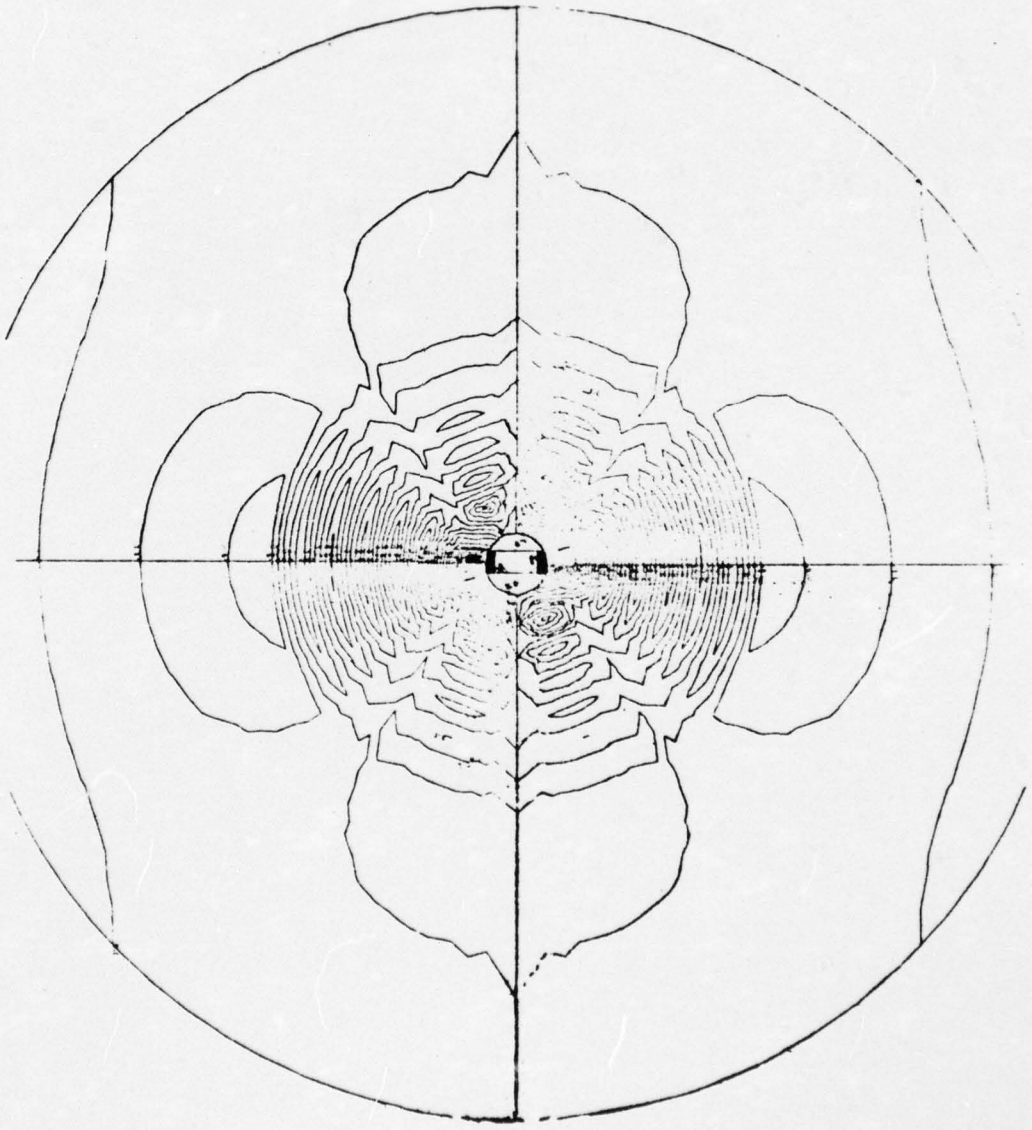

CIRCULAR HARMONIC = 1
FREQUENCY = 4500 Hz
WT = $\pi/2$
PRESSURE UNIT = 1 NEWTON/(METER)^2

FIGURE 14

nac

IN WATER COMPLEX ELECTRICAL IMPEDANCE PLOT

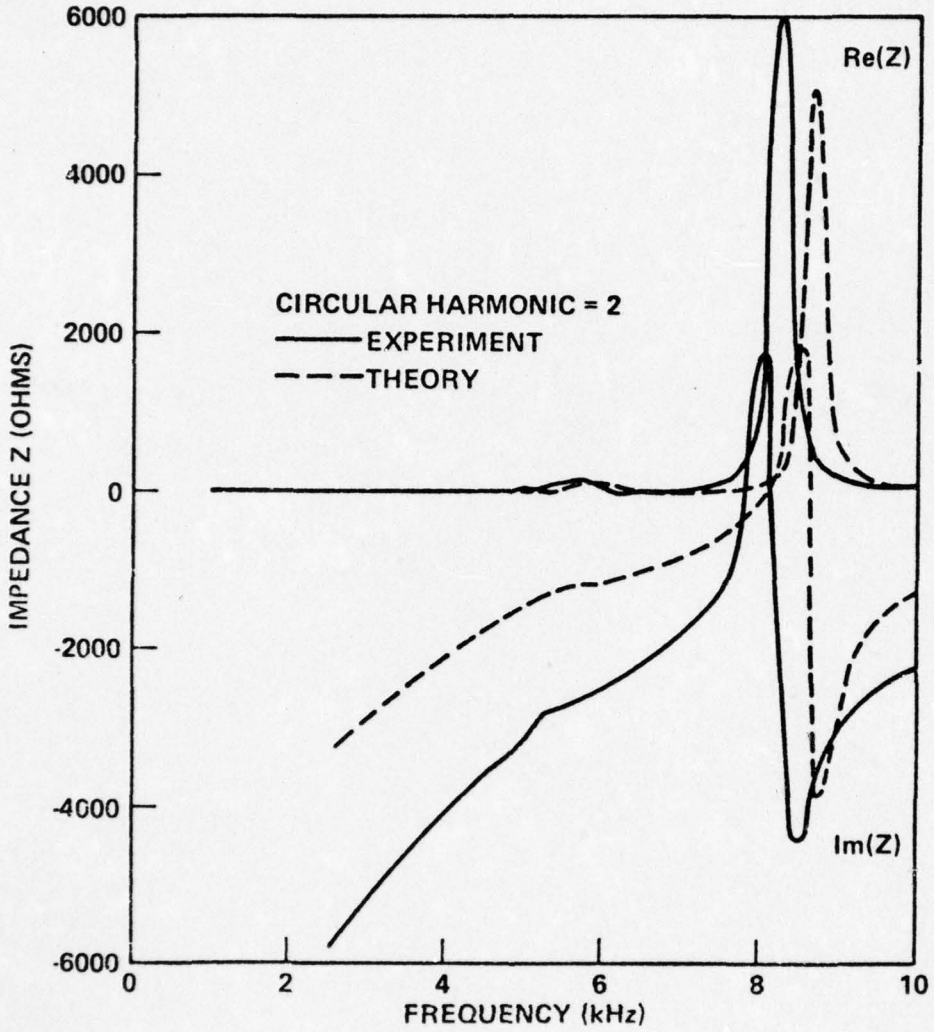

FIGURE 15

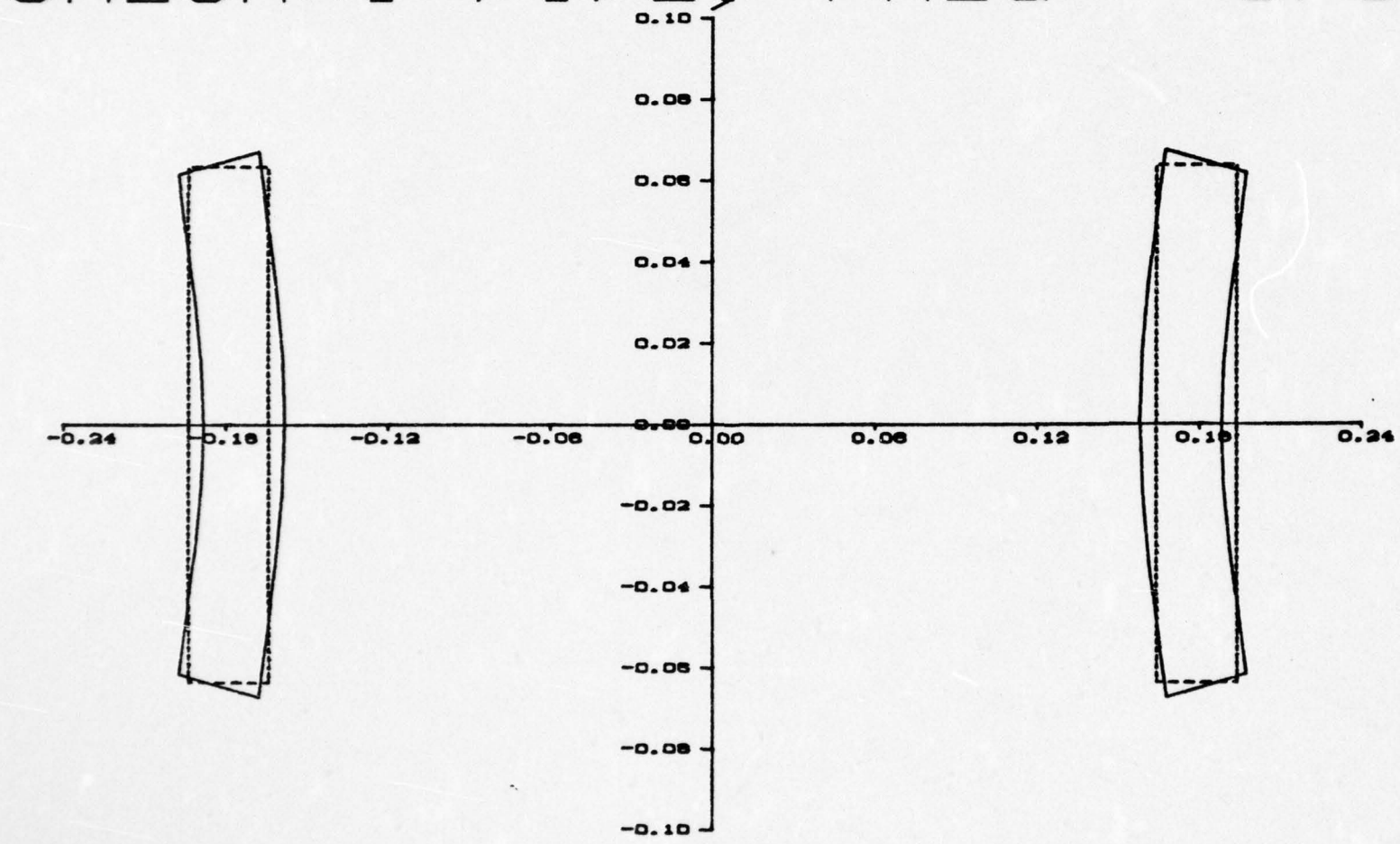
CYLINDER DISPLACEMENTS
CIRCULAR HARMONIC = 2
OMEGA*T=PI/2, FREQ= 8750
0.10
0.08
0.06
0.04
0.02
0.00
-0.02
-0.04
-0.06
-0.08
-0.10
-0.24
-0.18
-0.12
-0.06
0.00
0.06
0.12
0.18
0.24

FIGURE 16

noc

VERTICAL DIRECTIVITY PATTERN

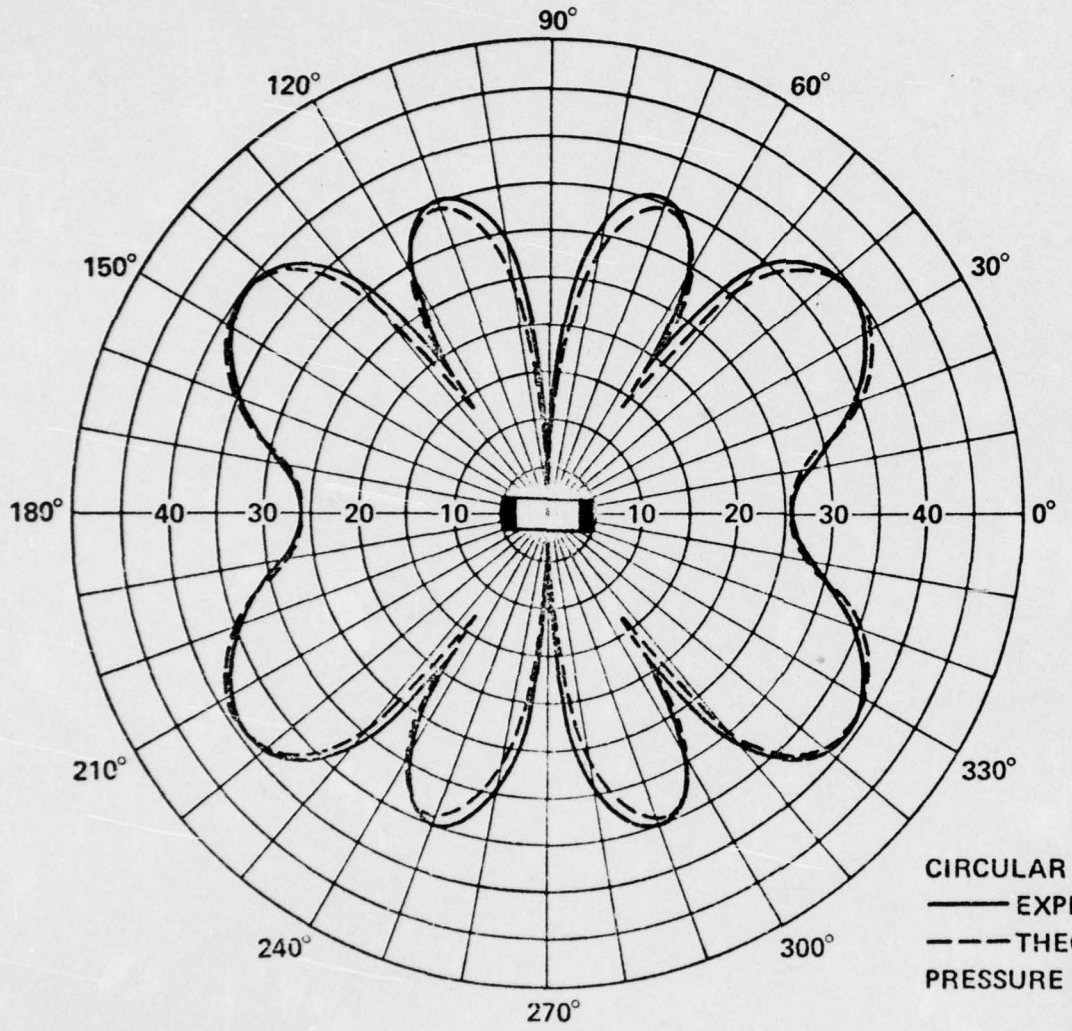

CIRCULAR HARMONIC = 2
——— EXPERIMENT AT 8250 Hz
– – – THEORY AT 8750 Hz
PRESSURE UNIT = 1 dB re 1 μbar/volt at 1 meter

FIGURE 17

HORIZONTAL DIRECTIVITY PATTERN

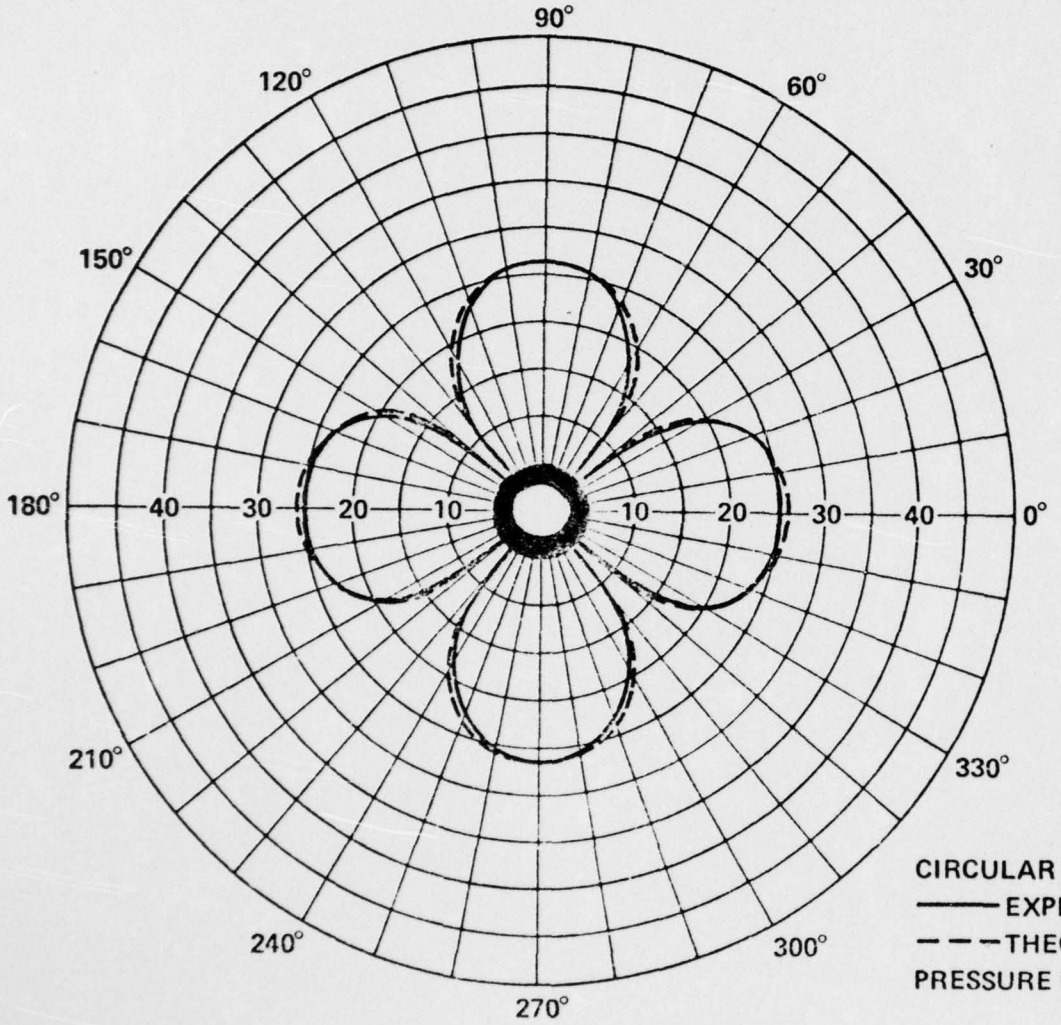

CIRCULAR HARMONIC = 2
——— EXPERIMENT AT 8250 Hz
– – – THEORY AT 8750 Hz
PRESSURE UNIT = 1 dB re 1 μbar/volt at 1 meter

FIGURE 18

NUC

RADIATED PRESSURE PATTERN FROM A TANGENTIALLY POLED CYLINDER (NEAR FIELD)

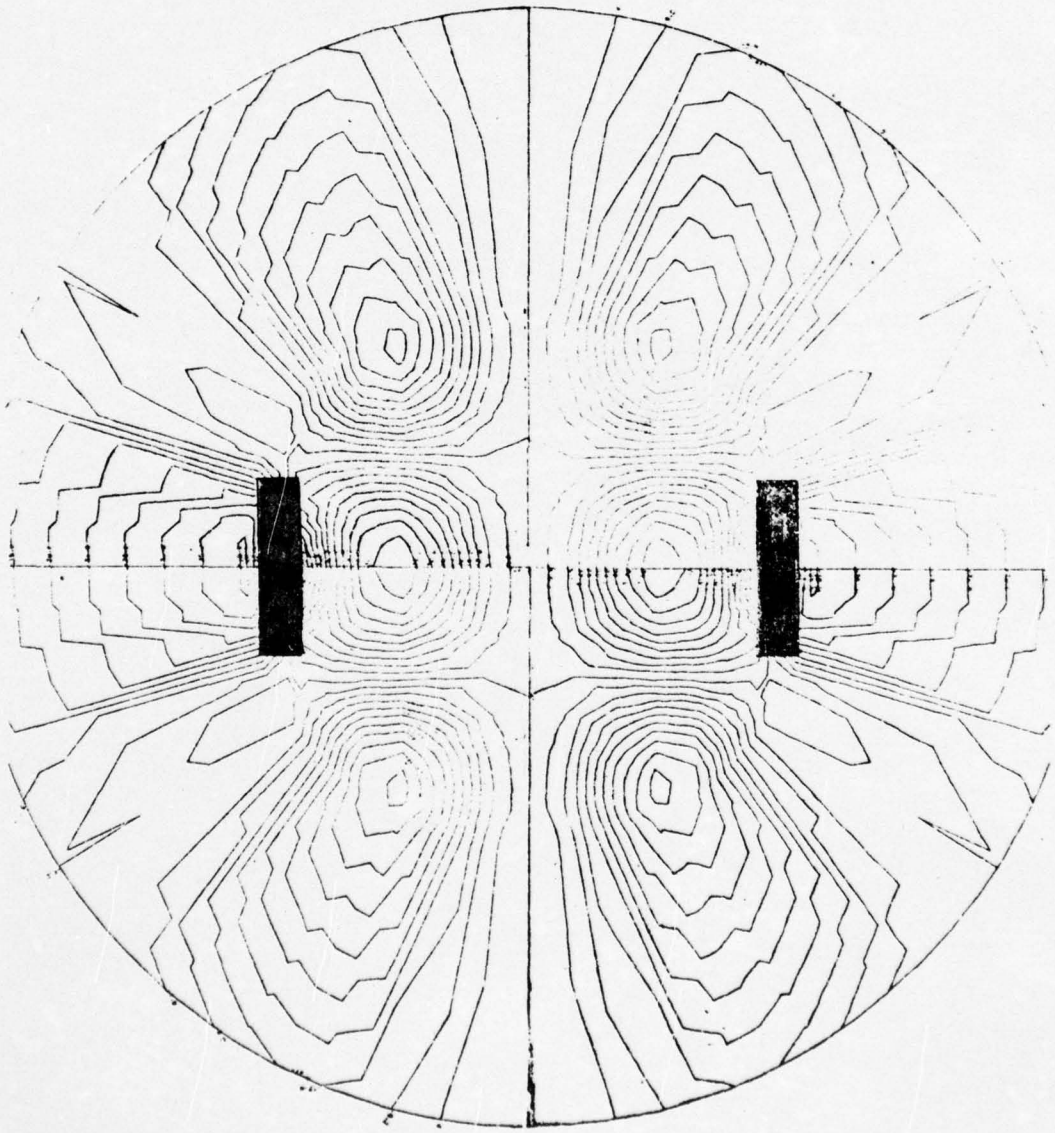

CIRCULAR HARMONIC = 2
FREQUENCY = 8750 Hz
WT = $\pi/2$
PRESSURE UNIT = 1 NEWTON/(METER)^2

FIGURE 19

#13

NUC

RADIATED PRESSURE PATTERN FROM A TANGENTIALLY POLED CYLINDER (FAR FIELD)

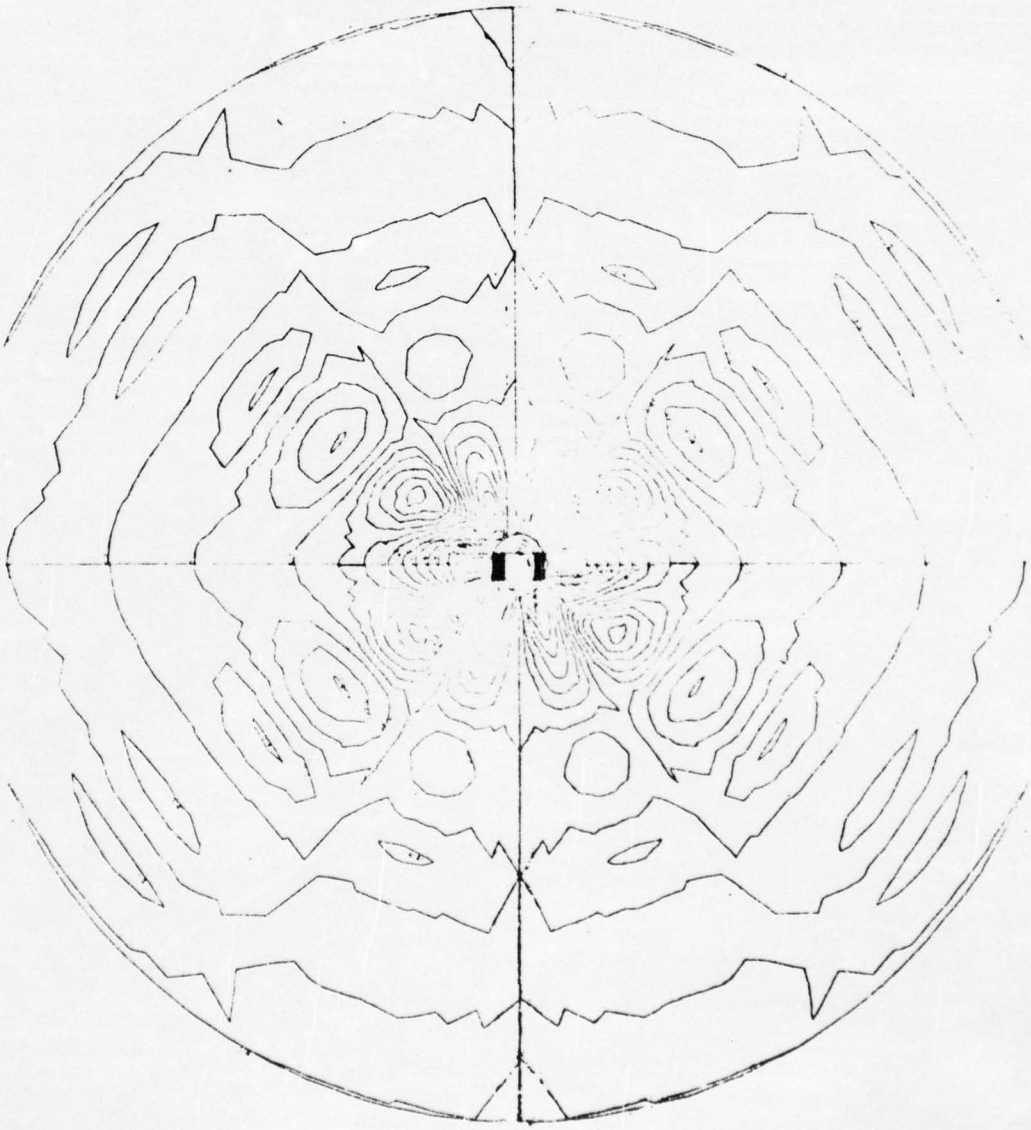

CIRCULAR HARMONIC = 2
FREQUENCY = 8750 Hz
WT = $\pi/2$
PRESSURE UNIT = 1 NEWTON/(METER)^2

FIGURE 20

APPLICATIONS OF THE FINITE ELEMENT METHOD AND COMPUTER GRAPHICS TO A TRANSDUCER ELEMENT

J.T. Hunt, R.R. Smith, D. Barach, L. McCleary
Naval Undersea Center

SUMMARY

Although many mathematical models have been developed for the longitudinal vibration type element discussed in this report, they have only partially succeeded in predicting its free vibrational response. The difficulty has been the large flexural interaction between the non-axisymmetric radiating head and the electrically driven axisymmetric tube, which results in a strong coupling between the circular harmonics of the piezoelectric tube. The inability to predict this effect has been the primary deficiency of earlier mathematical models. General Dynamics/ Electric Boat Division, in close cooperation with NUC, has used the finite-element method to develop a three-dimensional model in which this deficiency has been corrected. This mathematical model is representative of the most advanced techniques which describe the vibratory characteristics of an electromechanical sonar transducer. In this paper, the mathematical model is used to predict the deformation of the composite transducer in terms of the free vibrational modes of its component parts. Two types of computer-generated displays - contour plots of the predicted deformations and three-dimensional continuously shaded plots of these predicted deformations - are used to graphically illustrate the physical meaning of the model's numerical predictions. The contour plots are arranged so that they can be directly compared with the deformations experimentally measured by holographic interferometry. Predicted deformations are found to agree

closely with those measured experimentally.

The geometrical symmetry of the transducer consists of two reflection planes and a 180-deg rotation axis. By exploiting this geometrical symmetry, one can show that by modeling only one quarter of the transducer, i.e., that portion of the transducer situated between the two symmetry planes, and by applying the correct boundary conditions to nodal points located in the symmetry planes the correct vibrational response of the system can be obtained.

Although exploitation of the symmetry decreases the size of the numerical problem by almost a factor of four, the resulting eigenvalue problem still has 1135 displacement degrees of freedom. Hence, each eigenvector (or the deformation of the one-quarter model of the transducer at resonance) results in 1135 pieces of data, while the deformation of the entire transducer is represented by nearly 4000 numbers. Therefore, an understanding of the physical meaning of this large block of computer-generated data can be achieved only through its graphic display. We have used two different types of computer-generated data displays to depict the eigenvectors of the system.

SELF AND MUTUAL ACOUSTIC RADIATION IMPEDANCES FOR TWO COPLANAR UNBAFFLED DISKS

A.L. Van Buren and B.J. King
Naval Research Laboratory

SUMMARY

The self and mutual acoustic radiation impedances for two coplanar unbaffled disks are calculated using an eigenfunction expansion in terms of oblate spheroidal wave functions. Terms representing outgoing waves from both disks are included. One disk is assumed to be vibrating with a rotationally symmetrical normal velocity distribution, and the other disk is assumed to be stationary. The determination of the expansion coefficients from these boundary conditions is facilitated by the use of an addition theorem which expresses spheroidal wave functions with reference to one coordinate frame in terms of spheroidal wave functions with reference to a second coordinate frame. Numerical results for the special cases where the vibrating disk is either oscillating uniformly or vibrating uniformly on only one side are presented and discussed.

INTRODUCTION

The surface of a disk is the natural coordinate surface $\xi = 0$ in oblate spheroidal coordinates (ξ,η,ϕ). Thus the acoustic radiation from a disk vibrating harmonically with a known normal velocity distribution can be calculated by use of an eigenfunction expansion in terms of oblate spheroidal wave functions. The calculation can be extended to include a second, coplanar, vibrating disk by adding an expansion of spheroidal wave functions about the second disk. An addition theorem [1] which expresses spheroidal wave functions with reference to one coordinate frame in terms of spheroidal wave functions with reference to a second coordinate frame can be used to facilitate application of the boundary conditions on each disk.

By linear superposition, the acoustic radiation field of the two vibrating disks is equal to the sum of the field produced when the first disk is vibrating and the second disk is stationary and the field produced when the second disk is vibrating and the first disk is stationary. Thus no generality is lost by restricting the analysis to the case where the second disk is stationary.

This paper is concerned with both the self acoustic radiation impedance of the vibrating disk and the mutual acoustic radiation impedance between the vibrating disk and the stationary disk. The formulas necessary to evaluate the self and the mutual acoustic radiation impedances are developed in Sec. 2. It is assumed that the normal velocity distribution of the vibrating disk is rotationally symmetrical. In Sec. 3, numerical results calculated for the special cases where the first disk is either oscillating uniformly or vibrating uniformly on only one side are presented and

AD-A031 915 NAVAL SHIP SYSTEMS COMMAND WASHINGTON D C F/G 9/1
REPORT OF THE MATHEMATICAL MODEL WORKING GROUP, MEETING REPORT --ETC(U)
APR 73

UNCLASSIFIED NL

2 OF 2
AD
A031915

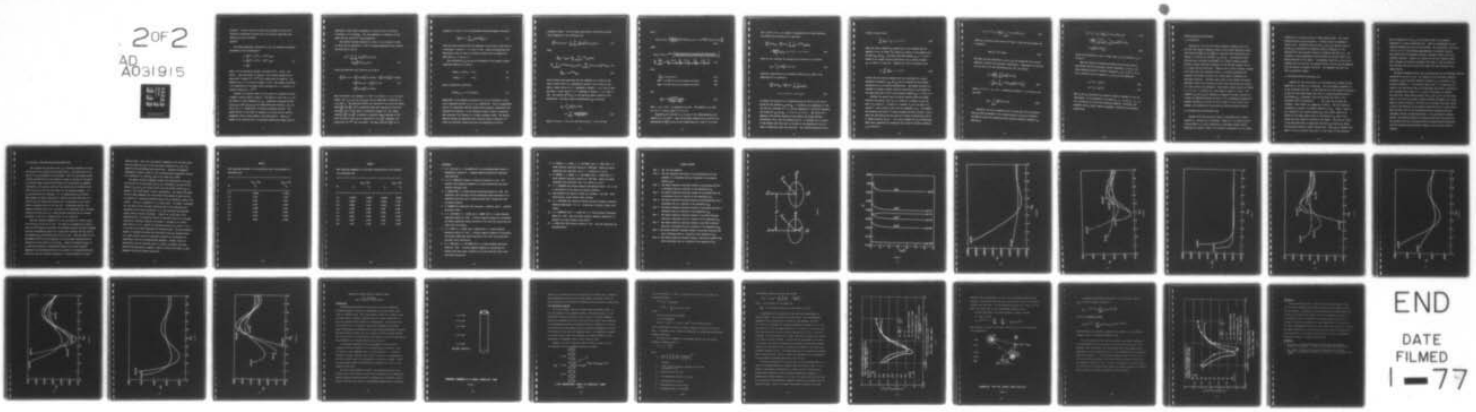

END
DATE FILMED
1-77

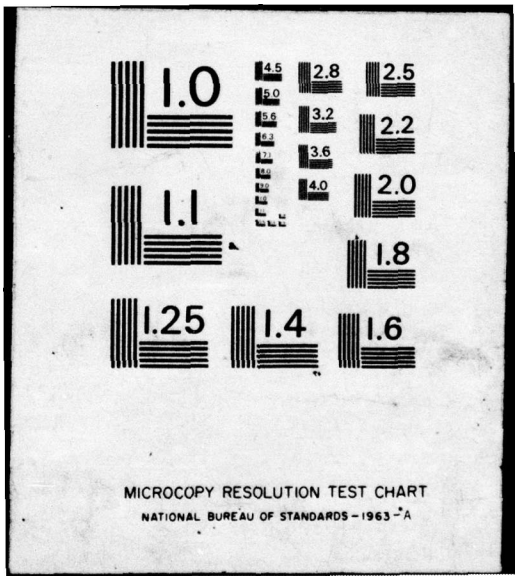
1.0
1.1
1.25
1.4
1.6
1.8
2.0
2.2
2.5
2.8
3.2
3.6
4.0
4.5
5.0
5.6
MICROCOPY RESOLUTION TEST CHART
NATIONAL BUREAU OF STANDARDS - 1963 - A

discussed. Previous results of Crane [2] and Hanish [3] which were obtained by approximate methods that do not involve spheroidal wave functions are also discussed.

ANALYSIS

The oblate spheroidal coordinates (ξ,η,ϕ) are related to Cartesian coordinates by the transformation

$$x = \frac{d}{2}(\xi^2 + 1)^{1/2}(1 - \eta^2)^{1/2} \cos\phi \ ,$$
$$y = \frac{d}{2}(\xi^2 + 1)^{1/2}(1 - \eta^2)^{1/2} \sin\phi \ , \qquad (1)$$
$$z = \frac{d}{2}\xi\eta \ ,$$

where d is the interfocal distance, and where $0 \le \xi < \infty$, $-1 \le \eta \le 1$, and $0 \le \phi < 2\pi$. Here the surface of constant ξ is an oblate spheroid with a major axis of length $(\xi^2 + 1)^{1/2}d$ and a minor axis of length ξd. The spheroid for $\xi = 0$ is a disk of radius $a = d/2$. The surface of constant η is a hyperboloid of one sheet which intersects the $\xi = 0$ surface in a circle of radius $a(1 - \eta^2)^{1/2}$.

Consider two identical disks D_1 and D_2 which are coplanar and share a common x axis, as shown in Figure 1. The radius of each disk is a, and the center to center separation is r_{12}. Spheroidal coordinate systems $C_1(\xi_1,\eta_1,\phi_1)$ and $C_2(\xi_2,\eta_2,\phi_2)$ are established which contain D_1 $(\xi_1 = 0)$ and D_2 $(\xi_2 = 0)$, respectively, as natural coordinate surfaces. The region exterior to the disks is assumed to be filled with an infinite homogeneous fluid of mass density ρ and sound speed c. Disk D_1 is assumed to be vibrating with a rotationally symmetrical normal velocity

distribution whose spatial dependance is given by $v(\eta_1)$, and disk D_2 is assumed to be stationary. The time dependence is assumed to be harmonic with the factor $e^{i\omega t}$ being suppressed.

The acoustic pressure produced at a point r on or exterior to both D_1 and D_2 can be expressed as a sum of outgoing spheroidal waves originating from both D_1 and D_2:

$$p(r) = \sum_{\ell=0}^{\infty} \sum_{m=0}^{\ell} [A_{m\ell}\psi_{m\ell}^{(4)}(h;\xi_1,\eta_1,\phi_1) + B_{m\ell}\psi_{m\ell}^{(4)}(h;\xi_2,\eta_2,\phi_2)] , \quad (2)$$

where the spheroidal wave functions are given by

$$\begin{aligned}\psi_{m\ell}^{(4)}(h;\xi,\eta,\phi) &= R_{m\ell}^{(1)}(h,\xi)S_{m\ell}^{(1)}(h,\eta)\cos m\phi - iR_{m\ell}^{(2)}(h,\xi)S_{m\ell}^{(1)}(h,\eta)\cos m\phi \\ &= \psi_{m\ell}^{(1)}(h;\xi,\eta,\phi) - i\psi_{m\ell}^{(2)}(h;\xi,\eta,\phi) \quad (3) \\ &= R_{m\ell}^{(4)}(h,\xi)S_{m\ell}^{(1)}(h,\eta)\cos m\phi .\end{aligned}$$

Here the acoustic size parameter $h = kd/2 = ka$, where $k = \omega/c$ is the wavenumber, and (ξ_1,η_1,ϕ_1) and (ξ_2,η_2,ϕ_2) are the spheroidal coordinates of r in C_1 and C_2. The spheroidal radial wave functions of the first and second kinds $R_{m\ell}^{(1)}$ and $R_{m\ell}^{(2)}$ and the spheroidal angle wave functions of the first kind $S_{m\ell}^{(1)}$ used in this report are defined by Flammer [4]. The radial functions $R_{m\ell}^{(1)}$ and $R_{m\ell}^{(2)}$ correspond to spherical Bessel functions of the first and second kinds and are normalized so that $\psi_{m\ell}^{(4)}$ represents outgoing waves for $e^{i\omega t}$ time dependence. The angle functions $S_{m\ell}^{(1)}$ can be

expanded in a series in the corresponding associated Legendre functions:

$$S_{m\ell}^{(1)}(h,\eta) = \sum_{n=0,1}^{\infty}{}' d_n(h|m\ell) P_{m+n}^{m}(\eta) , \tag{4}$$

where the prime indicates that the summation is over even or odd values of n according to whether $\ell - m$ is even or odd. Terms involving $\sin m\phi$ have been omitted from (2) since the acoustic pressure must be symmetrical about both $\phi_1 = 0$ and $\phi_2 = 0$.

The coefficients $A_{m\ell}$ and $B_{m\ell}$ are determined by the Neumann boundary conditions imposed on D_1 and D_2 :

$$-\partial p/\partial n_1 = i\omega\rho v(n_1) , \text{ on } D_1 \tag{5}$$

$$\partial p/\partial n_2 = 0 , \qquad \text{on } D_2 \tag{6}$$

where in spheroidal coordinates

$$(\partial p/\partial n)_{\xi = 0} = (1/|\eta|a)\partial p/\partial \xi . \tag{7}$$

Application of the boundary conditions on D_1 or D_2 is difficult if $p(r)$ is not expressed entirely in C_1 or C_2, respectively. This is accomplished by use of a spheroidal addition theorem which expresses a spheroidal wave function with reference to one coordinate frame in terms of spheroidal wave functions with reference to a second coordinate frame. The general addition theorem for spheroidal wave functions which is derived in [1] allows for arbitrary relative position and orientation of the two

coordinate frames. For the present application, the addition theorem can be expressed in the following form:

$$\psi_{m\ell}^{(4)}(h;\xi_i,\eta_i,\phi_i) = \sum_{n=0}^{\infty} \sum_{u=0,1}^{n}{}' C_{m\ell un}^{ij} \psi_{un}^{(1)}(h;\xi_j,\eta_j,\phi_j) \ , \tag{8}$$

where

$$C_{m\ell un}^{12} \equiv C_{m\ell un} = \frac{2}{N_{un}} \sum_{r=m,m+1}^{\infty}{}' i^{r-\ell} d_{r-m}(h|m\ell)$$

$$\times \sum_{s=u,u+1}^{\infty}{}' [i^{s-n}/(2s+1)] d_{s-u}(h|un) \sum_{t=|r-s|}^{r+s}{}' D(s,t,r,u,m) h_t^{(2)}(kr_{12}), \tag{9}$$

$$C_{m\ell un}^{21} = (-1)^{m-u} C_{m\ell un} \ , \tag{10}$$

with the prime sign indicating that the summation is in steps of two, where u starts from 0 or 1 depending on whether ℓ-m-n is even or odd, where r starts from m or m + 1 depending on whether ℓ - m is even or odd, and where s starts from u or u +1 depending on whether n - u is even or odd. The function $h_t^{(2)}(kr_{12})$ is the spherical Hankel function of the second kind. The angle function normalization N_{un} is given by

$$N_{un} = \int_{-1}^{1} [S_{un}^{(1)}(h,\eta)]^2 d\eta$$

$$= 2 \sum_{r=0,1}^{\infty}{}' \frac{(r+2u)!\, d^2(h|un)}{r!(2r+2u+1)} \ , \tag{11}$$

where r = 0,2,4,... if n-u is even and r=1,3,5,... if n-u is odd.

Also,

$$D(s,t,r,u,m) = \frac{\epsilon_u}{2}\left[\frac{(s+u)!}{(s-u)!}\,P_t^{m-u}(0)a(s,t,r,u,m) + (-1)^u P_t^{m+u}(0)a(s,t,r,-u,m)\right], \tag{12}$$

where

$$a(s,t,r,u,m) = i^{s+t-r}\left\{\frac{(2s+1)(2t+1)(s-u)!(t-m+u)!(r+m)![(s+t+r)/2]!}{[(r+t-s)/2]![(r+s-t)/2]![(s+t-r)/2]!(s+t+r+1)!}\right\}$$

$$\times \sum_{w=wmin}^{wmax} (-1)^w \binom{s+t-r}{[s+t-r)/2]+w}\binom{t+r-s}{[t+r-s)/2]+m-u+w}\binom{s+r-t}{[s+r-t)/2]-u+w}, \tag{13}$$

with

$$\binom{a}{b} = a!/[b!(a-b)!]\,, \tag{14}$$

$$wmin = 1/2\ [Max\ (r-s-t, s-r-t-2m+2u, t-s-r+2u)], \tag{15}$$

$$wmax = 1/2\ [Min\ (s+t-r, r+t-s-2m+2u, r+s-t+2u)], \tag{16}$$

and

$$P_p^q(0) = \frac{(-1)^{(p-q)/2}\ (p+q)!}{2^p(\frac{p-q}{2})!\ (\frac{p+q}{2})!}\,, \tag{17}$$

since $p-q \equiv t-m+u$ is required to be even. The quantity ϵ_u is equal to 1 if $u = 0$ and is equal to 2 if $u \neq 0$.

Expressing $p(r)$ entirely in C_1 by use of (8), differentiating with respect to ξ_1 in order to apply the boundary condition on D_1 given by (5), multiplying by $S_{qp}^{(1)}(h,\eta)\cos q\phi$ and integrating over η from -1 to +1 and

over ϕ from 0 to 2π , the ranges of orthogonality for these functions, one obtains the following set of equations:

$$\dot{R}^{(4)}_{qp}(h,0)A_{qp} + \dot{R}^{(1)}_{qp}(h,0) \sum_{\ell=0}^{\infty} \sum_{m=0}^{\ell} (-1)^{m-q} C_{m\ell qp} B_{m\ell}$$

$$= -\left(\frac{i\omega\rho a}{N_{0p}}\right) \delta_{q0} I_{0p}, \quad p = 0 \text{ to } \infty , \quad q = 0 \text{ to } p , \tag{18}$$

where the dot indicates the derivative with respect to ξ and where

$$I_{0p} = \int_{-1}^{1} v(\eta) S^{(1)}_{0p}(h,\eta) |\eta| d\eta . \tag{19}$$

Similarly, application of the boundary condition on D_2 leads to the additional set of equations:

$$\dot{R}^{(4)}_{qp}(h,0)B_{qp} + \dot{R}^{(1)}_{qp}(h,0) \sum_{\ell=0}^{\infty} \sum_{m=0}^{\ell} C_{m\ell qp} A_{m\ell}$$

$$= 0 , \quad p = 0 \text{ to } \infty , \quad q = 0 \text{ to } p . \tag{20}$$

In theory, the infinite set of equations given by (18) plus (20) can be solved for the unknowns $A_{m\ell}$ and $B_{m\ell}$. In practice, the summations in (18) and (20) are truncated at $\ell = L$, and the remaining $T = (L+1)(L+2)$ equations are solved for $A_{m\ell}$ and $B_{m\ell}$, $\ell = 0$ to L, $m = 0$ to ℓ . The choice for L depends on the desired accuracy of the results, the normal velocity distribution $v(\eta_1)$, and the acoustic size ka. An estimate for L is given by the highest order that must be retained in the expansion of $v(\eta_1)$ in terms of spheroidal angle wave functions. The truncated equations can be

written in matrix form

$$\sum_{r=1}^{T} M_{qr} b_r = g_q \ , \ q = 1 \text{ to } T \ , \tag{21}$$

where the matrix elements M_{qr} depend only on the frequency and the geometry of the two disks, the elements b_r consist of the unknown coefficients $A_{m\ell}$ and $B_{m\ell}$, the right hand side elements g_q, q = 1 to T/2, depend on the normal velocity distribution $v(\eta_1)$, and the elements g_q, q = T/2+1 to T are zero. Equation (21) can be inverted to give

$$b_r = \sum_{q=1}^{T} M_{rq}^{-1} g_q \ , \ r = 1 \text{ to } T \ , \tag{22}$$

so that once the inverse elements have been calculated for a given frequency and geometry, $A_{m\ell}$ and $B_{m\ell}$ can be obtained for any velocity distribution on D_1 by matrix multiplication. The method can easily be extended to include a nonzero velocity distribution on D_2 by modifying the right hand side of (20) to give nonzero elements g_q, q = T/2+1 to T.

Consider the special case of uniform vibration where the normal velocity distribution $v(\eta_1)$ on D_1 is equal to a constant V_1 over the part of D_1 called S^+ , is equal to a constant $-V_1$ over the part of D_1 called S^- , and is equal to zero over the remainder of D_1. For example, the pulsating disk has an S^+ region covering the entire surface $-1 \le \eta_1 \le 1$, while the oscillating disk has both an S^+ region covering $0 \le \eta_1 \le 1$ and an S^- region covering $-1 \le \eta_1 < 0$. It is still assumed that D_2 is stationary. Under these conditions the normalized self acoustic radiation impedance z_s is defined by

$$z_s = r_s + ix_s = \frac{1}{\rho c V_1 A_1} \int_{S^+ + S^-} p(\eta_1, \phi_1) dS(\eta_1, \phi_1) , \tag{23}$$

where A_1 is the sum of the areas of S^+ and S^-, where the area element dS is given by

$$dS(\eta, \phi) = a^2 |\eta| d\eta d\phi , \tag{24}$$

and where the real quantities r_s and x_s are the normalized self acoustic radiation resistance and reactance, respectively. Expressing p(r) entirely in C_1 by use of (8) and substituting into (23), one obtains

$$z_s = \frac{2\pi a^2}{\rho c V_1 A_1} \sum_{\ell=0}^{\infty} \left[A_{0\ell} R_{0\ell}^{(4)}(h,0) I'_{0\ell} + \sum_{m=0}^{\ell} B_{m\ell} \sum_{n=0,1}^{\infty'} (-1)^m C_{m\ell 0n} R_{0n}^{(1)}(h,0) I'_{0n} \right] , \tag{25}$$

where n = 0, 2,4... or 1,3,5... depending on whether $\ell - m$ is even or odd, and where

$$I'_{0\ell} = \int_{S^+ + S^-} S_{0\ell}^{(1)}(h,\eta) |\eta| d\eta . \tag{26}$$

Similarly, the force produced by p(r) on that part of the stationary disk D_2 which corresponds to the vibrating area on D_1 can be calculated and used to obtain the normalized mutual acoustic radiation impedance z_m. This gives

$$z_m = r_m + ix_m = \frac{1}{\rho c V_1 A_1} \int p(\eta_2,\phi_2) dS(\eta_2,\phi_2) \tag{27}$$

$$= \frac{2\pi a^2}{\rho c V_1 A_1} \sum_{\ell=0}^{\infty} \left[\sum_{m=0}^{\ell} A_{m\ell} \sum_{n=0,1}^{\infty\,\prime} C_{m\ell 0n} R_{0n}^{(1)}(h,0) I'_{0n} \right.$$

$$\left. + B_{0\ell} R_{0\ell}^{(4)}(h,0) I'_{0\ell} \right] , \tag{28}$$

where the integration is over the same range in η_2 as covered by η_1 in S^+ and S^-.

When both disks are vibrating uniformly with the same velocity distribution and with individual velocity amplitudes, V_1 and V_2, the total normalized acoustic radiation impedances z_1 for D_1 and z_2 for D_2 can be obtained from the impedances z_s and z_m by the expressions

$$z_1 = z_s + z_m V_2/V_1 , \tag{29}$$

$$z_2 = z_s + z_m V_1/V_2 . \tag{30}$$

Thus z_s and z_m characterize the acoustic radiation impedance of the two disk system. In the remainder of the paper z_s, r_s, x_s and z_m, r_m, x_m will be referred to as the self radiation impedance, resistance, and reactance and the mutual radiation impedance, resistance and reactance, respectively.

NUMERICAL RESULTS AND DISCUSSION

a. Introduction

Calculation of the self and mutual radiation impedances by use of (25) and (28) requires numerical values for the oblate spheroidal radial wave functions $R_{m\ell}^{(1)}(h,0)$ and $R_{m\ell}^{(2)}(h,0)$ and their first derivatives with respect to ξ and for the integrals $I_{0\ell}$ and $I'_{0\ell}$. The necessary radial functions were calculated using OBRAD [5], a Fortran computer program written in double precision arithmetic for the CDC 3800 computer at the U. S. Naval Research Laboratory. OBRAD is one of several computer programs [6,7] which have been developed recently to evaluate spheroidal wave functions with greater accuracy over a wider range of parameter than previously available. Extensive tables [8,9] of both oblate and prolate spheroidal radial wave functions and their first derivatives with respect to ξ have recently been published. These tables contain entries for values of $m = 0,1,2$; $\ell = m(1)m+49$ for a wide range of values of ξ and h. The integrals $I_{0\ell}$ and $I'_{0\ell}$ were evaluated by expanding the angle functions in a series of Legendre functions as given in (4), subsequently expanding the Legendre functions in a series in $\cos r\theta$, where $\theta = \cos^{-1}\eta$ and r is an integer, and evaluating in closed form the resulting simple integrals.

b. Pulsating Disk and Stationary Disk

Consider first the case where disk D_1 is pulsating with a normal velocity V_1, and disk D_2 is stationary. Since the $z = 0$ plane exclusive of the surface of D_1 can be replaced by a stationary surface without affecting the acoustic fields, the situation is equivalent to the uniform

vibration of a circular piston in a rigid infinite plane. This latter problem has been solved previously. A detailed review by Bouwkamp is found in [10]. Extensive tables of both z_s and z_m for various values of ka and kr_{12} calculated from expressions given by Rayleigh [11] and Pritchard [12] were published recently by Berkowitz and Baier [13]. The existence of these independent results provides an accurate check on the method described in this report. Corresponding values for z_s and z_m were obtained from (25) and (28) for numerous values of ka and kr_{12} and compared with the results of Berkowitz and Baier. The agreement was never less than 3 significant figures.

c. Oscillating Disk and Stationary Disk

Consider the case where disk D_1 is oscillating with a normal velocity amplitude V_1, and disk D_2 is stationary. The self radiation impedance of D_1 was calculated from (25). It was found that the self radiation reactance x_s does not vary significantly from that of a single oscillating disk as the spacing kr_{12} is decreased from over 200, where the effect of the stationary disk is negligible, to 2ka, where the two disks are touching. These results are summarized in Table 1. The self radiation resistance r_s, however, is somewhat sensitive to kr_{12}. Figure 2 shows r_s as a function of the relative spacing r_{12}/a for several values of ka. Because of the large dynamic range of the values for r_s, some of the curves have been scaled as indicated in the figure. Note that the effect of the stationary disk is significant when both r_{12}/a and ka are small, but decreases rapidly as either becomes large. When r_{12}/a is greater than about 4.0 or ka is greater than about 1.5, the effect of the stationary

disk is negligible so that r_s is very nearly equal to the radiation resistance of a single oscillating disk. Crane [2] investigated the self radiation impedance for this two disk problem. His calculations, restricted to ka = 0.3 to 1.0 and involving approximations of uncertain validity, also showed that the stationary disk has a negligible effect on the self radiation reactance. However, his results for the self radiation resistance, although in qualitative agreement with Figure 2, show an effect of the stationary disk that is many times larger than that obtained by the present method.

The mutual impedance between the oscillating disk and the stationary disk was calculated by the use of (28). The behavior of both the mutual radiation resistance r_m and the mutual radiation reactance x_m as a function of kr_{12} is shown in Figures 3 - 6 for several values of ka. It is seen that the effect of the oscillating disk on the stationary disk tends to increase as ka is increased until about ka = 2.5 when it then begins to decrease. Note that point dipole theory predicts that r_m and x_m will be identically equal to zero since the acoustic pressure vanishes throughout the z plane. Thus the initial increase in the effect as ka increases from small values is due to the deviation of the pressure field from that of a point dipole. Both the finite size of the oscillating disk and scattering from the stationary disk are contributing factors. As ka continues to increase, however, the competing effects of increased directivity associated with the radiation from the oscillating disk and increased phase cancellation over the stationary disk eventually dominate, and the effect begins to decrease.

d. One-Sided Vibrating Disk and Stationary Disk

Now consider the case where disk D_1 is vibrating uniformly over only its top half with a normal velocity amplitude V_1. The bottom half of D_1 and all of D_2 are assumed to be stationary. Note that the surface normal velocity distribution for this problem is equal to one half of the sum of the surface normal velocity distributions for the previous two examples. Consequently, the acoustic field for this problem can be obtained as one half of the sum of the acoustic fields for the separate problems: (a) D_1 oscillating and D_2 stationary (b) D_1 pulsating and D_2 stationary. This example of linear superposition, known as the Gutin principle [14] results from the linear wave equation and is represented in the linear nature of equations such as (19) and (22). As mentioned earlier, the acoustic radiation from (b) is equivalent to the radiation from a uniformly vibrating circular piston in a rigid infinite plane and can be evaluated accurately by the use of formulas given in the literature.

The self radiation impedance of D_1 was calculated for several values of ka and kr_{12} by the use of (25). The results are summarized in Table 2. Both the self radiation resistance and reactance remained virtually unchanged from the corresponding values for a single disk vibrating from one side as the spacing kr_{12} is decreased from over 200 to 2ka. Thus the effect of the stationary disk on the self impedance of the one-sided vibrating disk is negligible for all values of ka and kr_{12}. Crane [2] presented values for r_s that were obtained by combining his values for the self radiation impedance of an oscillating disk in the presence of a stationary disk with values for the self radiation impedance of a circular piston in a rigid

infinite plane. Note that the radiation impedance of the circular piston does not depend on kr_{12}, so that the entire variation of r_s with kr_{12} comes from the oscillating-disk contribution. Therefore the apparent inaccuracy in Crane's values for the oscillating-disk contribution results in a variation of r_s with kr_{12} that is too large (up to 20%).

The mutual radiation impedance between the vibrating half of D_1 and the top half of the stationary disk D_2 was calculated by the use of (28). Values of r_m and x_m for various values of ka are plotted versus kr_{12} in Figures 7 and 8 and Figures 9 and 10, respectively. The results for small ka are in good agreement with calculations using monopole theory where D_1 is replaced by a uniformly pulsating sphere with an equivalent volume acceleration, and D_2 is considered to be a single point. For small, increasing ka, the effect of the one-sided vibrating disk on the stationary disk increases as the volume acceleration of D_1 also increases and produces a larger acoustic pressure everywhere. However, as in the case of the oscillating disk, the competing factors of increased directivity and phase cancellation eventually dominate and produce a decrease in the effect above about ka = 2.0. Hanish [3] calculated values of r_m for ka = 0.1 to 1.0 by use of the linear superposition described above. He used Pritchard's formula to evaluate accurately the contribution from the circular piston in a rigid infinite plane but neglected scattering in calculating the contribution from the oscillating-disk component. However, since the contribution from the circular piston is usually far greater than that from the oscillating-disk component, Hanish's results are usually in good agreement with those obtained using (28).

TABLE 1

Self radiation reactance of an oscillating disk in the presence of a stationary disk

ka	$kr_{12} = 2ka$ x_s	$kr_{12} = 200$ x_s
0.1	0.0426	0.0425
0.3	0.130	0.130
0.5	0.224	0.223
1.0	0.514	0.515
1.5	0.888	0.904
2.0	1.035	1.001
2.5	0.519	0.533
3.0	0.225	0.226

TABLE 2

Self radiation impedance of a one-sided vibrating disk in the presence of a stationary disk

	$kr_{12} = 2ka$		$kr_{12} = 200$	
ka	r_s	x_s	r_s	x_s
0.1	0.00250	0.0636	0.00250	0.0636
0.3	0.0223	0.189	0.0223	0.189
0.5	0.0611	0.310	0.0610	0.310
1.0	0.234	0.580	0.232	0.581
1.5	0.524	0.784	0.529	0.792
2.0	0.976	0.785	0.977	0.768
2.5	1.196	0.421	1.190	0.428
3.0	1.114	0.192	1.117	0.193

REFERENCES

1. B. J. KING and A. L. VAN BUREN 1973, to be published, SIAM Journal on Mathematical Analysis 4. A general addition theorem for spheroidal wave functions.

2. P. H. G. CRANE 1970 Journal of Sound and Vibration 11, 115. The Acoustic self-radiation impedance of a rigid oscillating disk near a similar stationary disk.

3. S. HANISH 1960 U. S. Naval Research Laboratory Report No. 5538. The mechanical self resistance and the mechanical mutual resistance of an unbaffled rigid disk (ka<1) radiating sound from a single face into an acoustic medium.

4. C. FLAMMER 1957 Spheroidal Wave Functions. Stanford, Calif.: Stanford University Press.

5. A. L. VAN BUREN, R. V. BAIER, and S. HANISH 1970 U. S. Naval Research Laboratory Report No. 6959. A fortran computer program for calculating the oblate spheroidal radial functions of the first and second kind and their first derivatives.

6. B. J. KING, R. V. BAIER, and S. HANISH 1970 U. S. Naval Research Laboratory Report No. 7012. A fortran computer program for calculating the prolate spheroidal radial functions of the first and second kind and their first derivatives.

7. B. J. KING and A. L. VAN BUREN 1970 U. S. Naval Research Laboratory Report No. 7161. A fortran computer program for calculating the prolate and oblate angle functions of the first kind and their first and second derivatives.

8. S. HANISH, R. V. BAIER, A. L. VAN BUREN, and B. J. KING 1970 U. S. Naval Research Laboratory Reports No. 7088-7090. Tables of radial spheroidal wave functions, vols. 1 - 3, prolate, m = 0,1,2.

9. S. HANISH, R. V. BAIER, A. L. VAN BUREN, and B. J. KING 1970 U. S. Naval Research Laboratory Reports No. 7091-7093. Tables of radial spheroidal wave functions, vols. 4-6, oblate m = 0,1,2.

10. C. J. BOUWKAMP 1946 Philips Research Laboratories Report 1 No. 4, 251. A contribution to the theory of acoustic radiation.

11. LORD RAYLEIGH 1877 Theory of Sound (two volumes). New York: Dover Publications, second edition, 1945 re-issue.

12. R. L. PRITCHARD 1951 Harvard University Acoustics Research Laboratory Technical Memorandum. No. 21. Directivity of Acoustic Linear Point Arrays.

13. R. L. BERKOWITZ and R. V. BAIER 1971 U. S. Naval Research Laboratory Report No. 7008. Self and mutual acoustic radiation impedances for pistons in a plane infinite rigid baffle.

14. L. GUTIN 1937 USSR Technical Physics 4, 404. Uber das schallfeld der kolbenstrahlern.

FIGURE CAPTIONS

Fig. 1 The two disk geometry.

Fig. 2 The self radiation resistance of an oscillating disk in the presence of a stationary disk as a function of the relative spacing r_{12}/a.

Fig. 3 The mutual radiation resistance between an oscillating disk and a stationary disk as a function of the separation kr_{12}.

Fig. 4 The mutual radiation resistance between an oscillating disk and a stationary disk as a function of the separation kr_{12}.

Fig. 5 The mutual radiation reactance between an oscillating disk and a stationary disk as a function of the separation kr_{12}.

Fig. 6 The mutual radiation reactance between an oscillating disk and a stationary disk as a function of the separation kr_{12}.

Fig. 7 The mutual radiation resistance between a one-sided vibrating disk and a stationary disk as a function of the separation kr_{12}.

Fig. 8 The mutual radiation resistance between a one-sided vibrating disk and a stationary disk as a function of the separation kr_{12}.

Fig. 9 The mutual radiation reactance between a one-sided vibrating disk and a stationary disk as a function of the separation kr_{12}.

Fig. 10 The mutual radiation reactance between a one-sided vibrating disk and a stationary disk as a function of the separation kr_{12}.

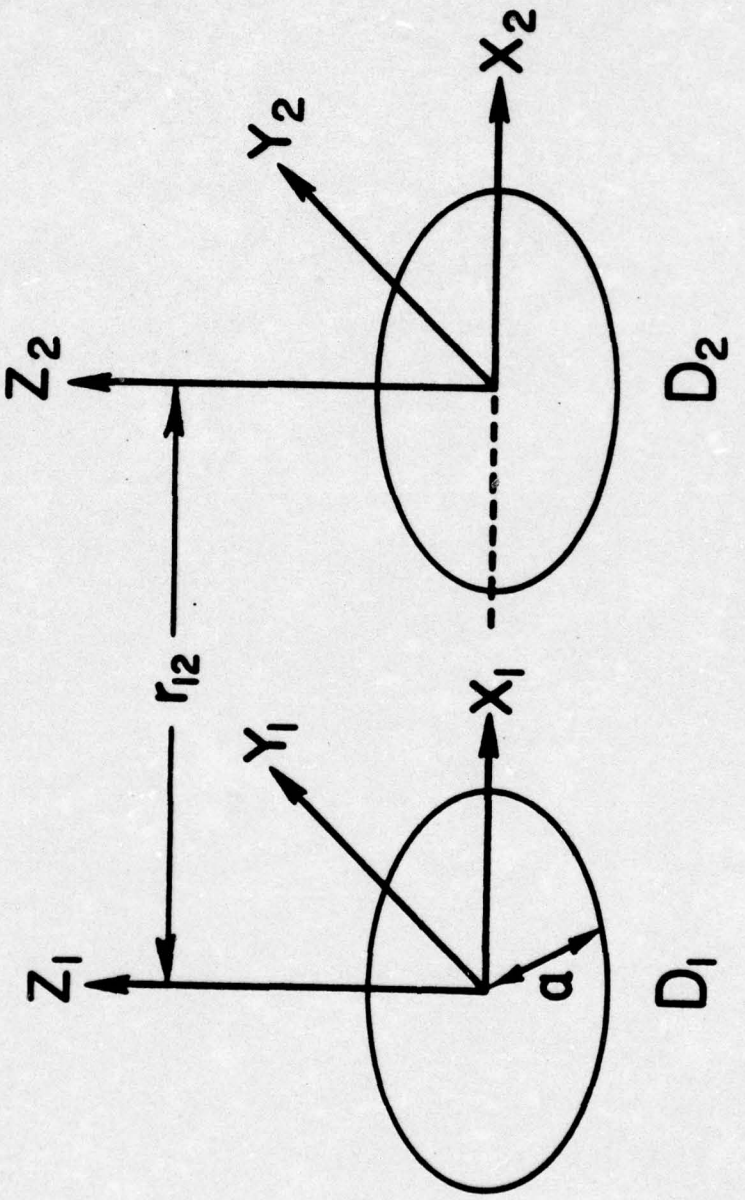

FIGURE 1

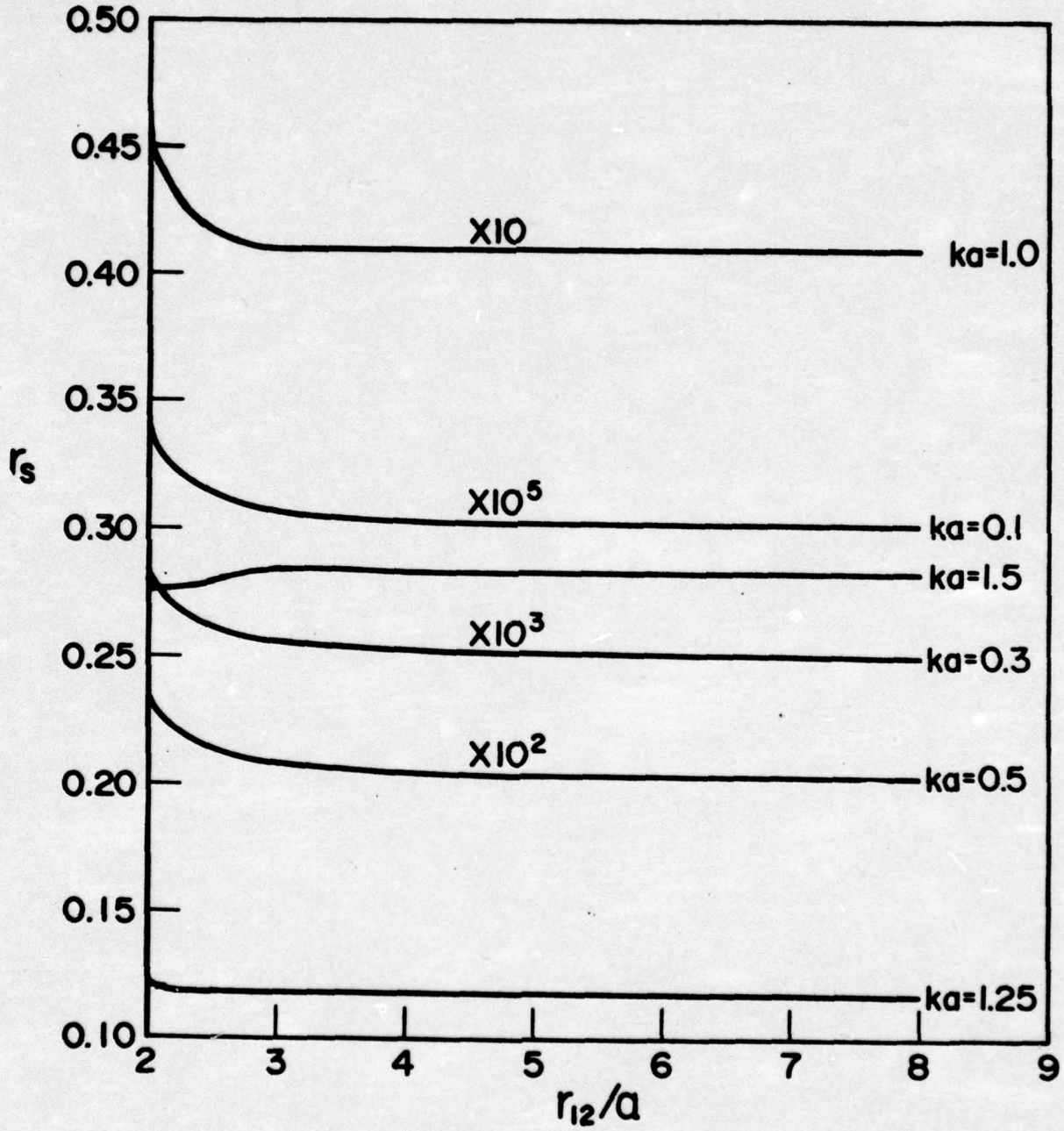
0.50
0.45
0.40
0.35
0.30
0.25
0.20
0.15
0.10
r_s
X10
ka=1.0
$X10^5$
ka=0.1
ka=1.5
$X10^3$
ka=0.3
$X10^2$
ka=0.5
ka=1.25
2
3
4
5
6
7
8
9
r_{12}/a

FIGURE 2

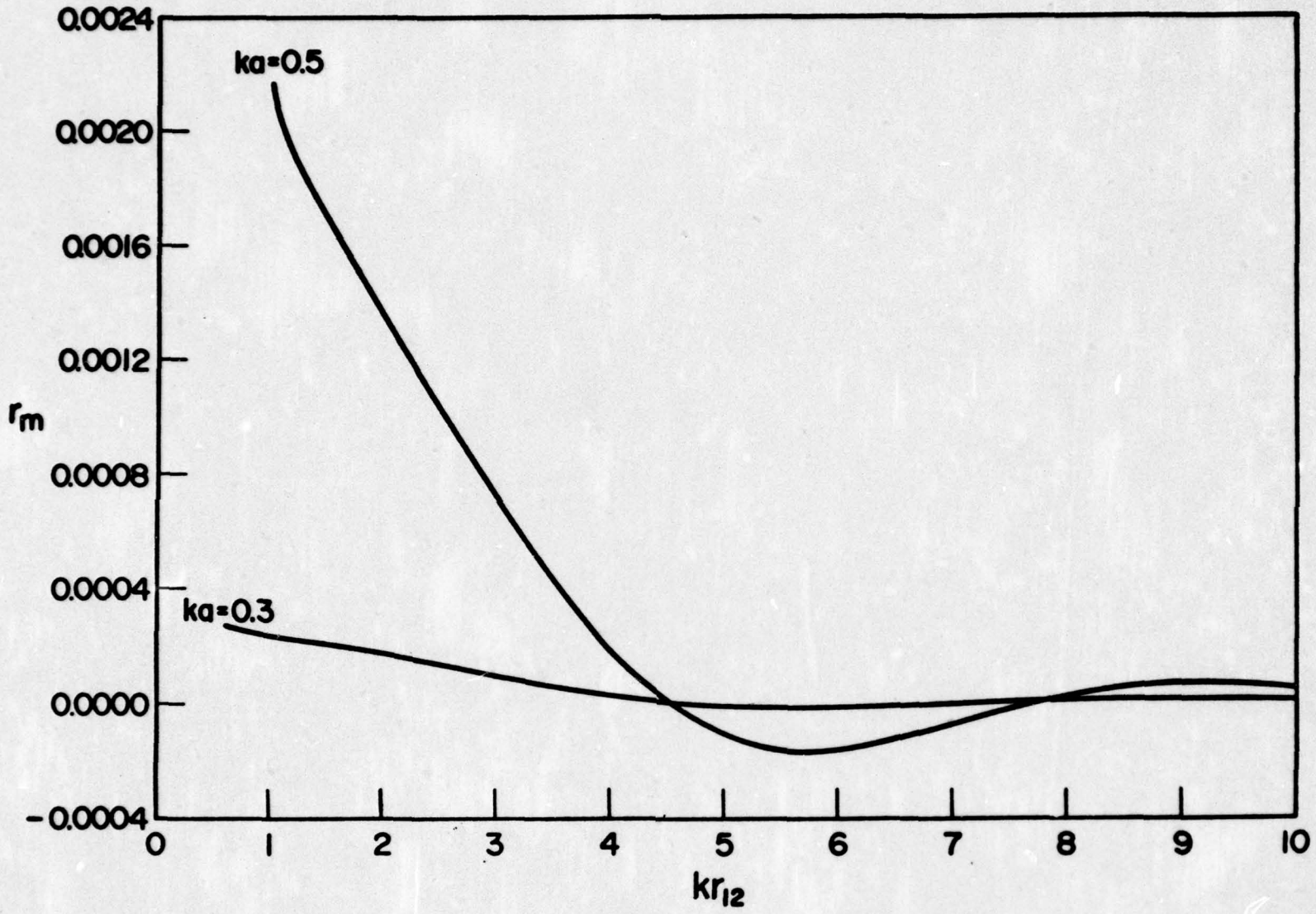
0.0024
0.0020
0.0016
0.0012
0.0008
0.0004
0.0000
-0.0004
r_m
ka=0.5
ka=0.3
0
1
2
3
4
5
6
7
8
9
10
kr_{12}

FIGURE 3

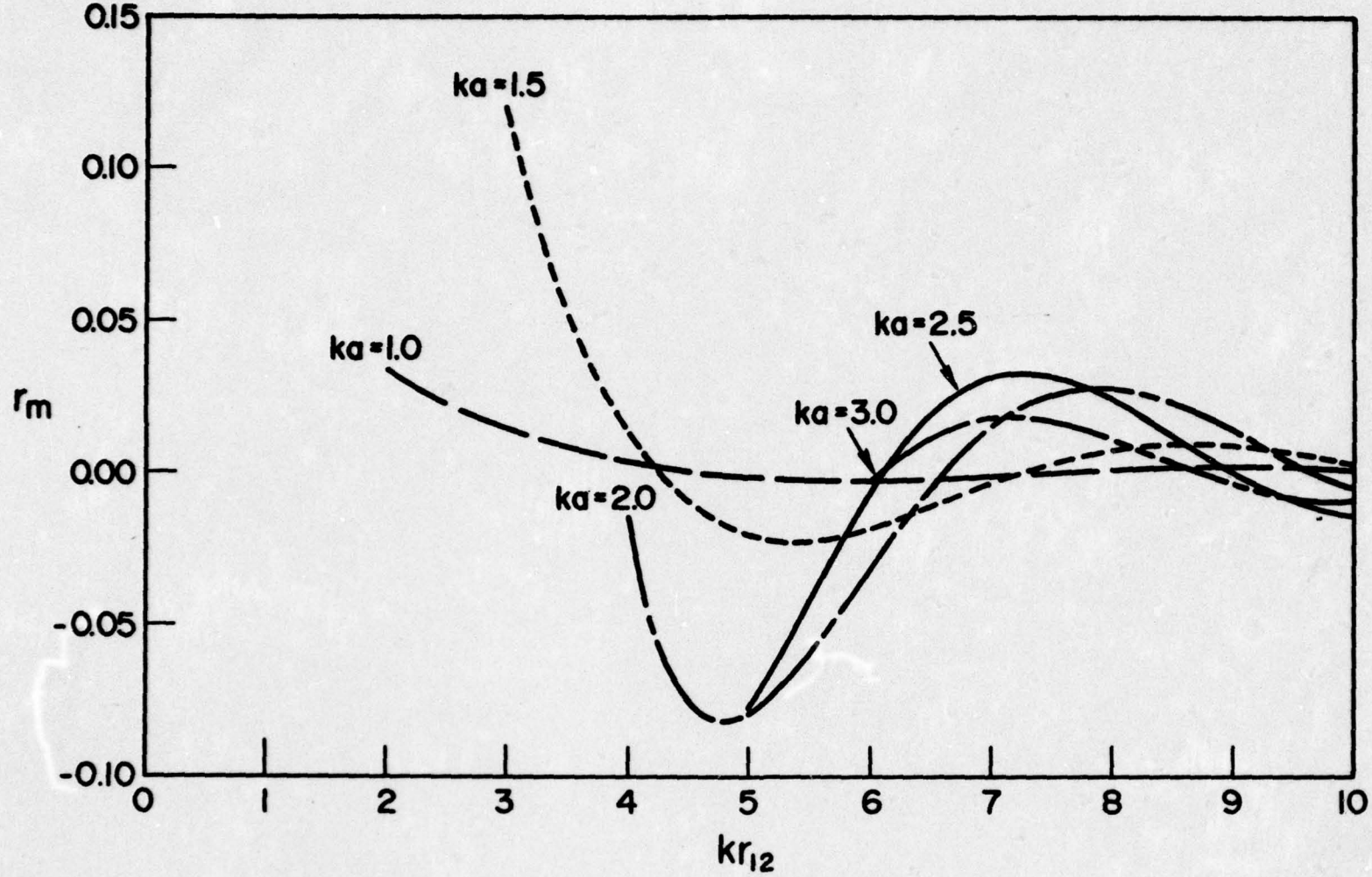
0.15
0.10
0.05
0.00
-0.05
-0.10
r_m
ka=1.5
ka=1.0
ka=2.5
ka=3.0
ka=2.0
0
1
2
3
4
5
6
7
8
9
10
kr_{12}

FIGURE 4

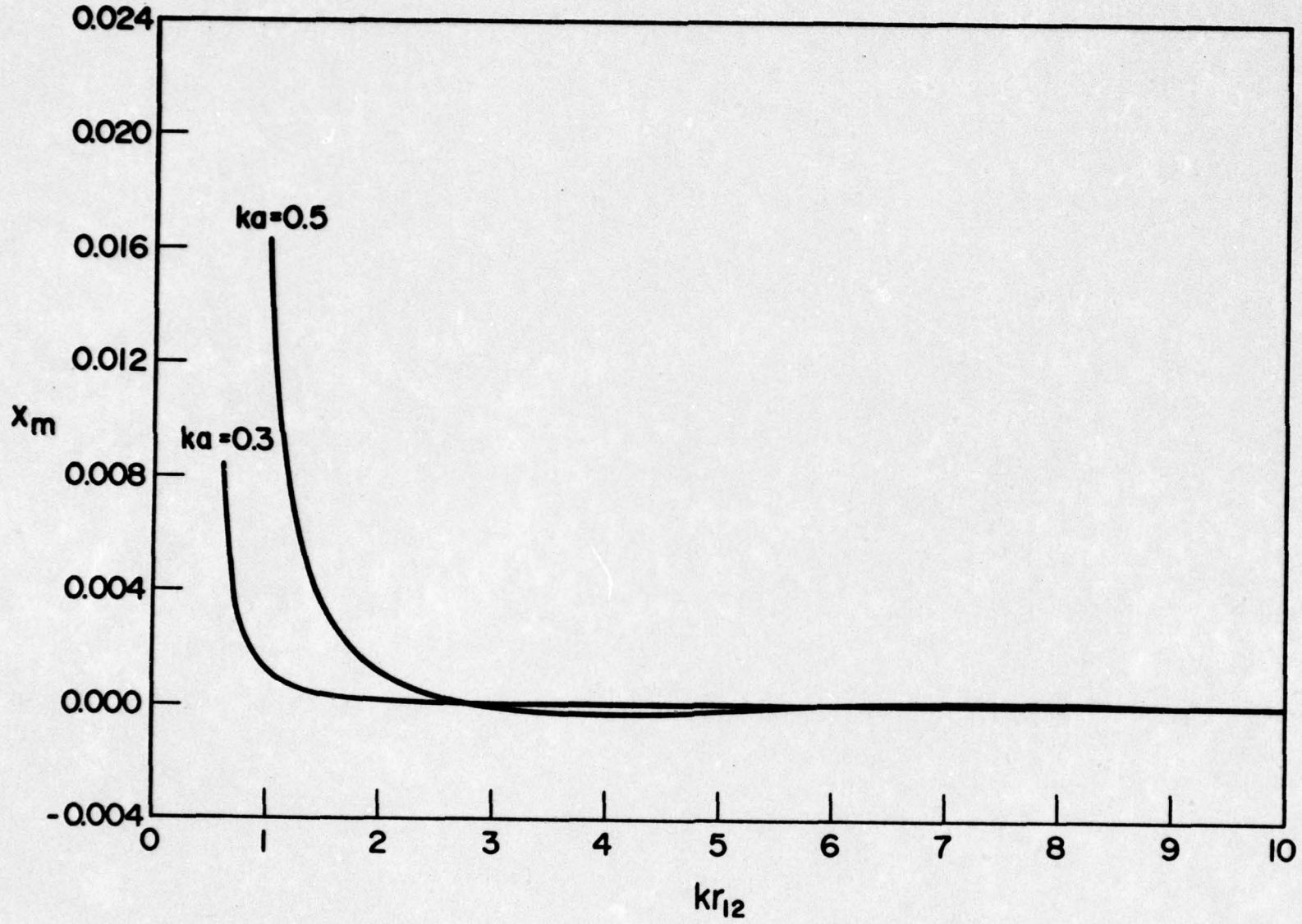
0.024
0.020
0.016
0.012
0.008
0.004
0.000
-0.004
X_m
ka=0.5
ka=0.3
0
1
2
3
4
5
6
7
8
9
10
kr_{12}

FIGURE 5

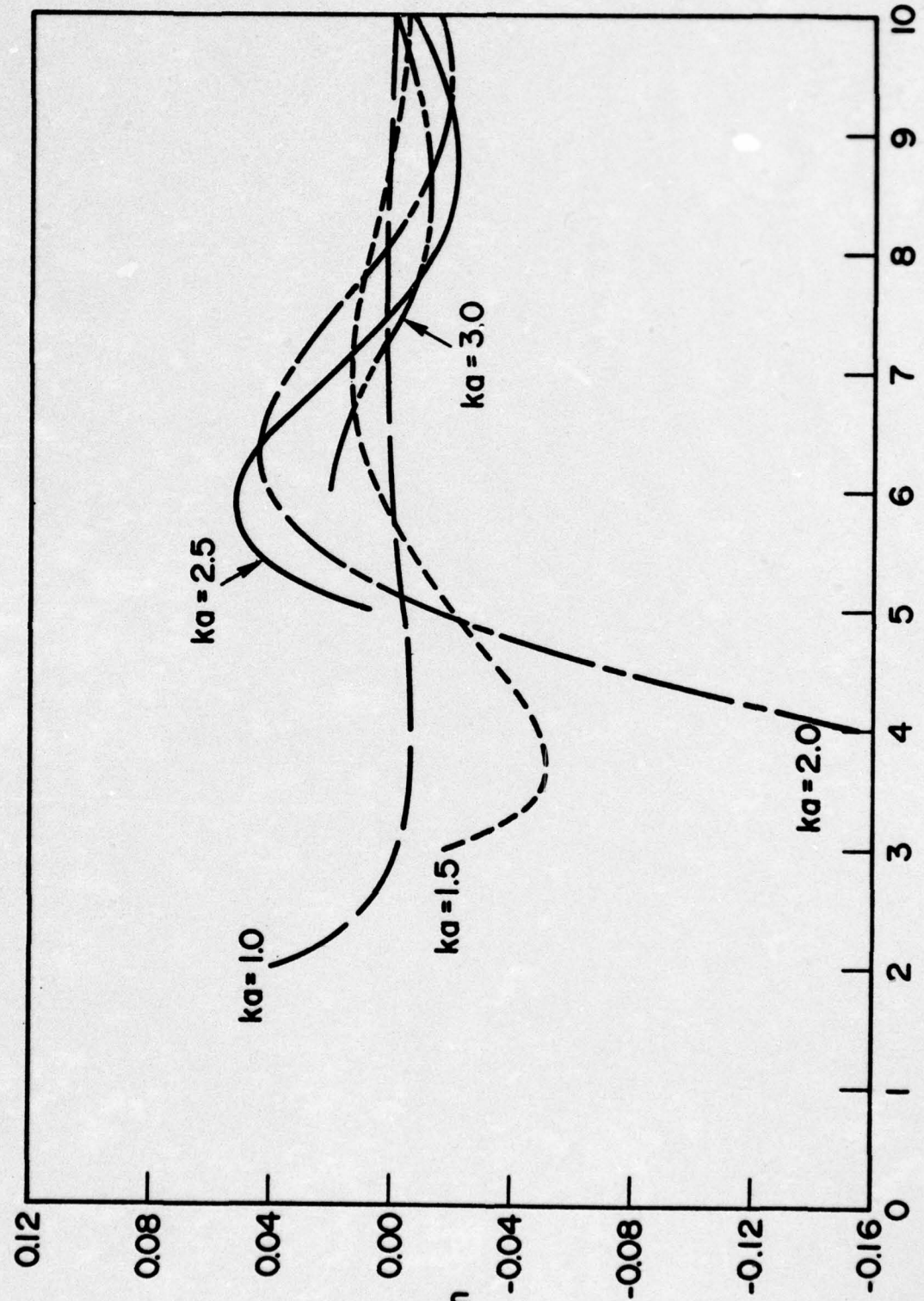
0.12
0.08
0.04
0.00
-0.04
-0.08
-0.12
-0.16
x_m
0
1
2
3
4
5
6
7
8
9
10
kr_{12}
ka=1.0
ka=1.5
ka=2.0
ka=2.5
ka=3.0

FIGURE 6

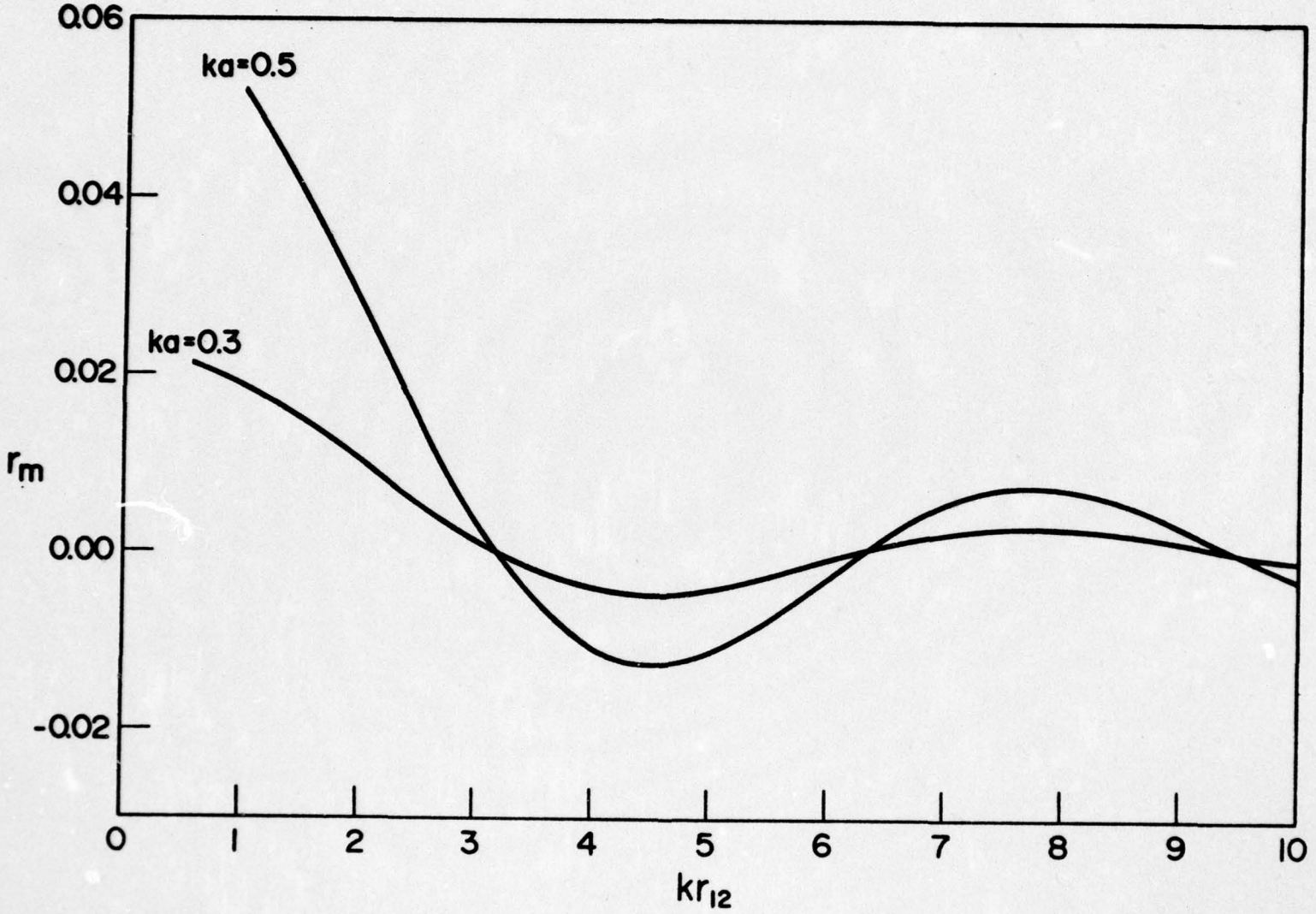

FIGURE 7

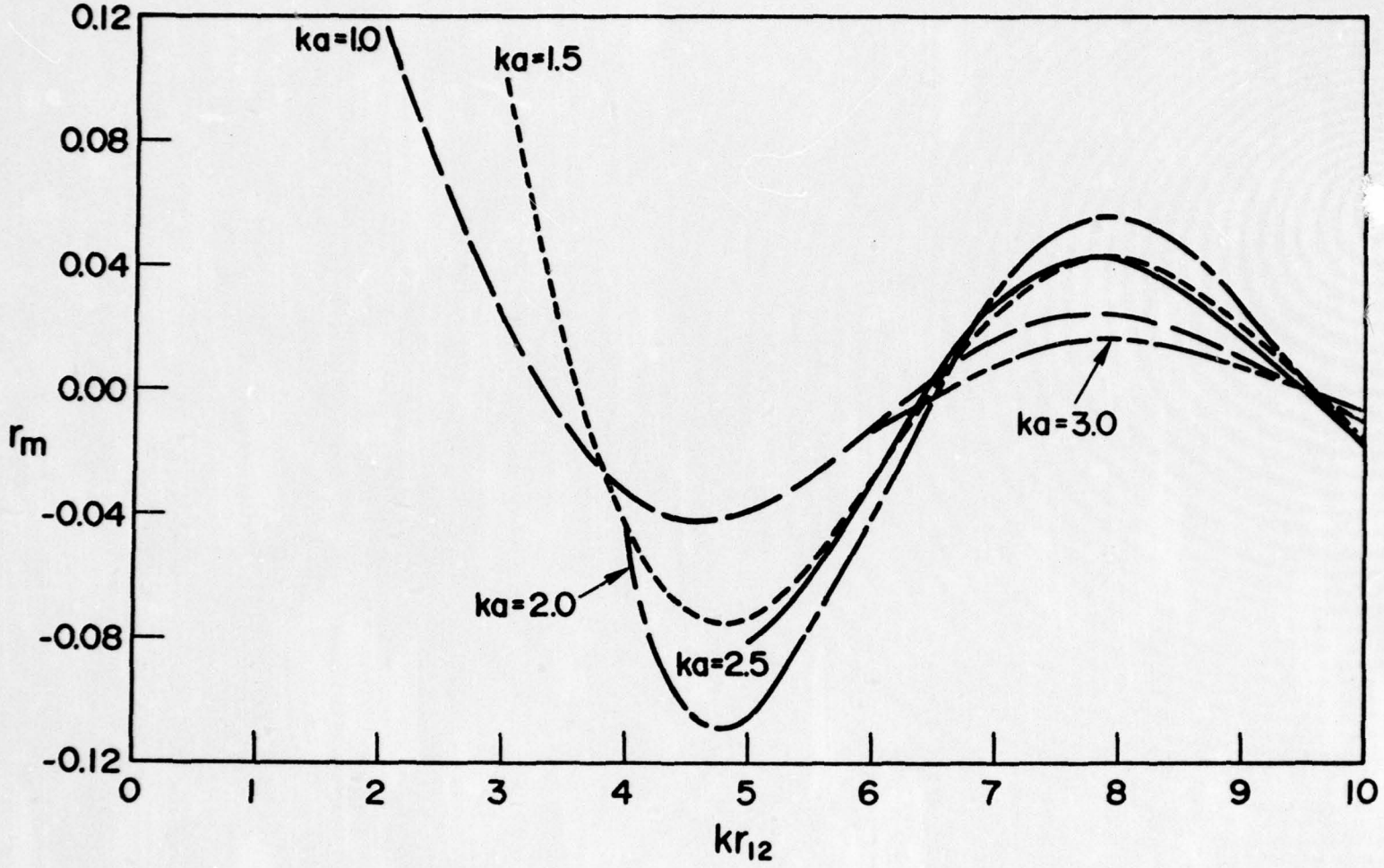
0.12
0.08
0.04
0.00
-0.04
-0.08
-0.12
r_m
0
1
2
3
4
5
6
7
8
9
10
kr_{12}
ka=1.0
ka=1.5
ka=2.0
ka=2.5
ka=3.0

FIGURE 8

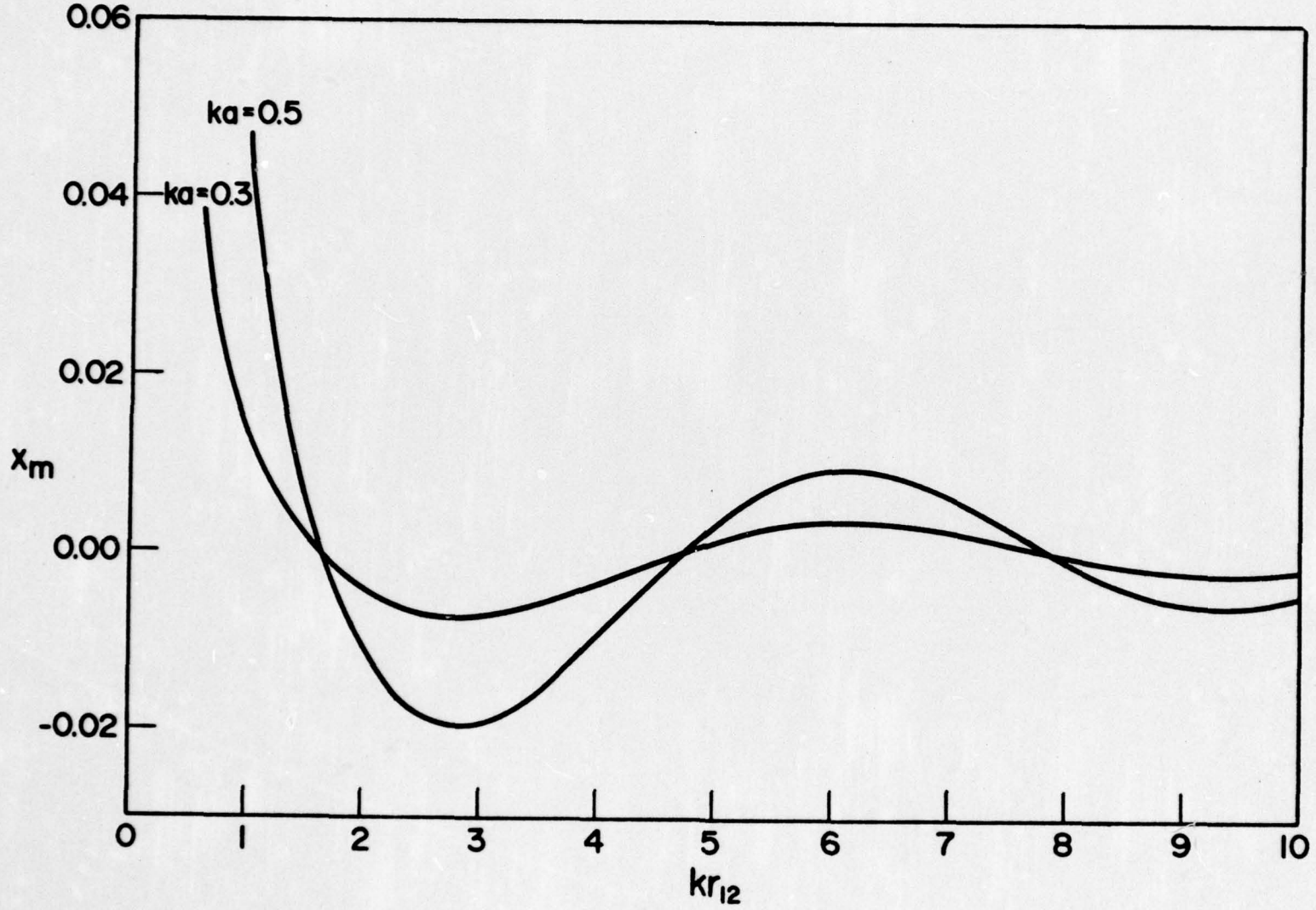

FIGURE 9

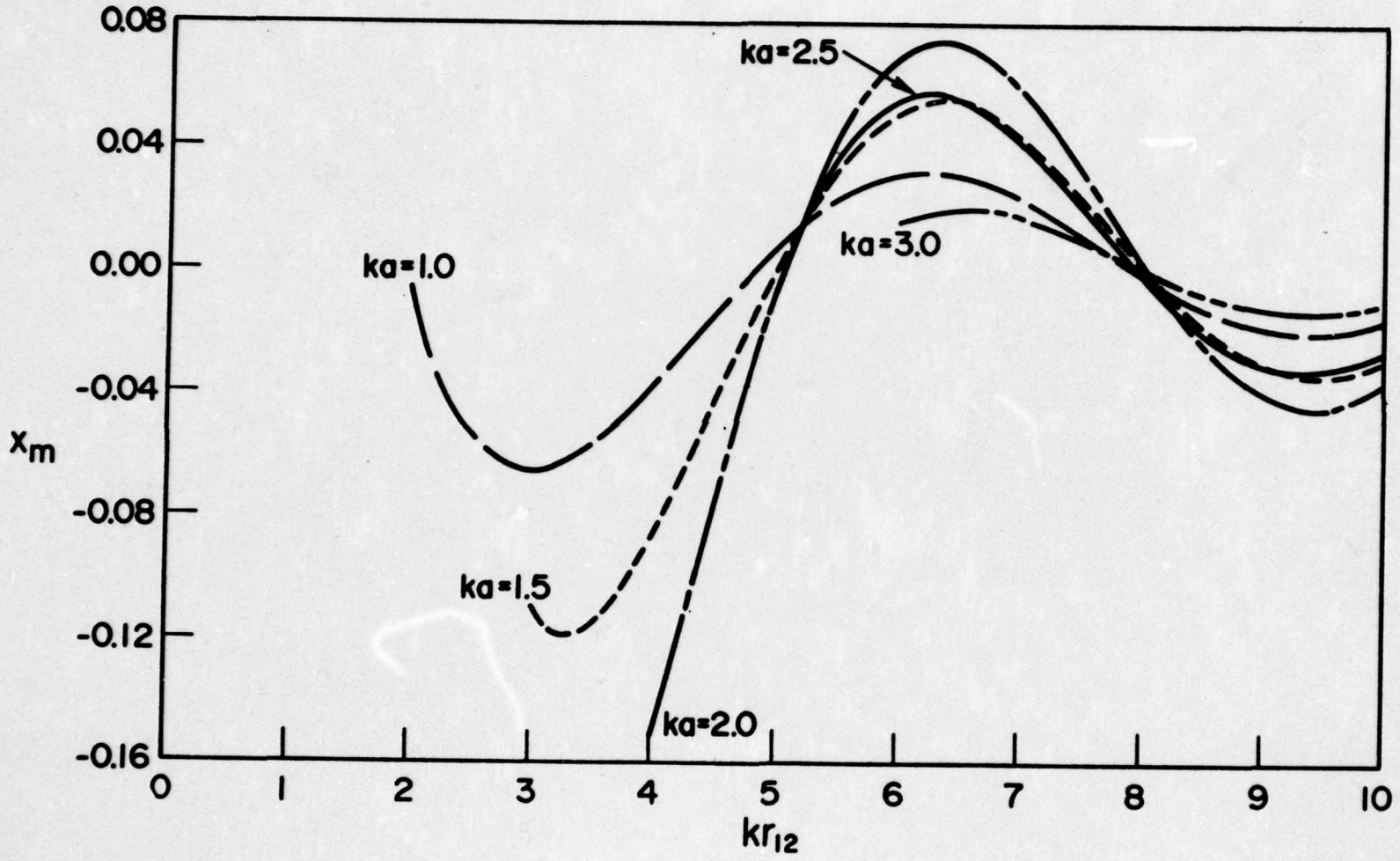
0.08
0.04
0.00
-0.04
-0.08
-0.12
-0.16
x_m
ka=2.5
ka=3.0
ka=1.0
ka=1.5
ka=2.0
0
1
2
3
4
5
6
7
8
9
10
kr_{12}

FIGURE 10

MODELING OF FINITE ARRAYS OF COMPLIANT TUBES

R.P. Radlinski
Naval Underwater Systems Center

INTRODUCTION

The modeling described here concerns the use of two dimensional multibody programs to predict the performance of a finite width, plane array of compliant tubes. The current plans at NUSC are to imbed at least one planar array of plastic compliant tubes in a rubber blanket and to test this composite when attached to a flexing plate. The two-fold task of the baffle is to (1) provide a noise free environment for outboard mounted hydrophones by reflecting near field radiation generated by flexural wave back toward the plate, and (2) to reduce the level of sound radiated into the far field. In this portion of the report, we will be investigating the performance of an isolated planar array of tubes.

An individual compliant tube can be designed to have its first transverse flexural resonance in the frequency band of interest. Thus, the tubes are truly compliant only in a finite bandwidth. A schematic diagram of a single compliant tube is shown in Figure 1. Mathematically, the tube is often taken to be rectangular or elliptical in shape. Toulis had considerable success by analyzing the performance of a tube as a bar clamped at both ends.[1]

The first tubes designed by Toulis[2] were metallic and used in an acoustic lens. Metal tubes were also used as reflectors in the NUSC-North American Autonetics AFAR system now in operation near the Azores Islands. Plastic tubes have been used in a Johns-Hopkins Applied Physics Laboratory-

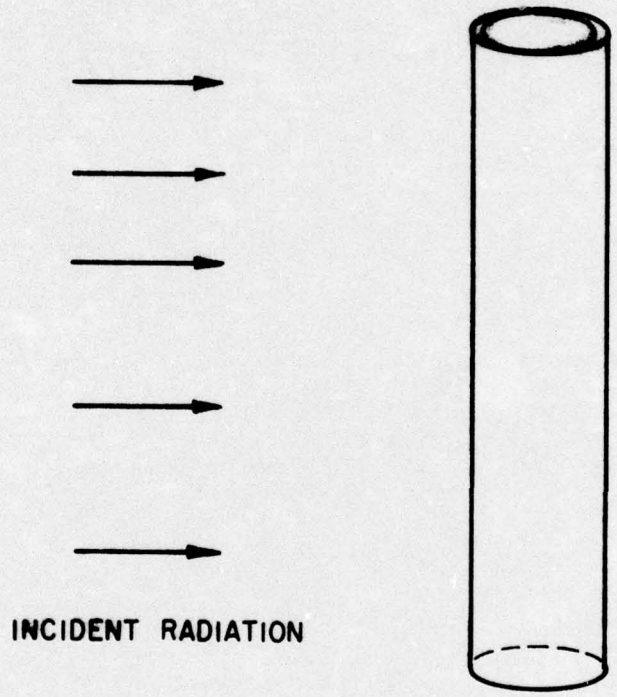

SCHMATIC DIAGRAM OF A SINGLE COMPLIANT TUBE

FIGURE 1

Autonetics collaboration of the construction of a Luneburg lens. Compliant tube technology has been pursued at NUSC largely through the efforts of Gerald Brigham who was formerly associated with the Autonetics collaborations.

TWO DIMENSIONAL MODELING

Let us now consider modeling a finite array of compliant tubes. At the last meeting of this committee at NRL, I described the use of a two dimensional arbitrary body model which was used to calculate radiation patterns and impedances for line arrays near finite width, soft reflectors. A two dimensional analysis was possible because the lengths of the interacting bodies were long compared with the acoustic wavelengths of interest. The situation is the same with compliant tubes. By extending the program to include incident plane wave radiation, it becomes feasible to study reflection or transmission from a finite array of tubes.

Consider an array of compliant tubes, as shown in Figure 2, where the individual tube is considered elliptical in shape.

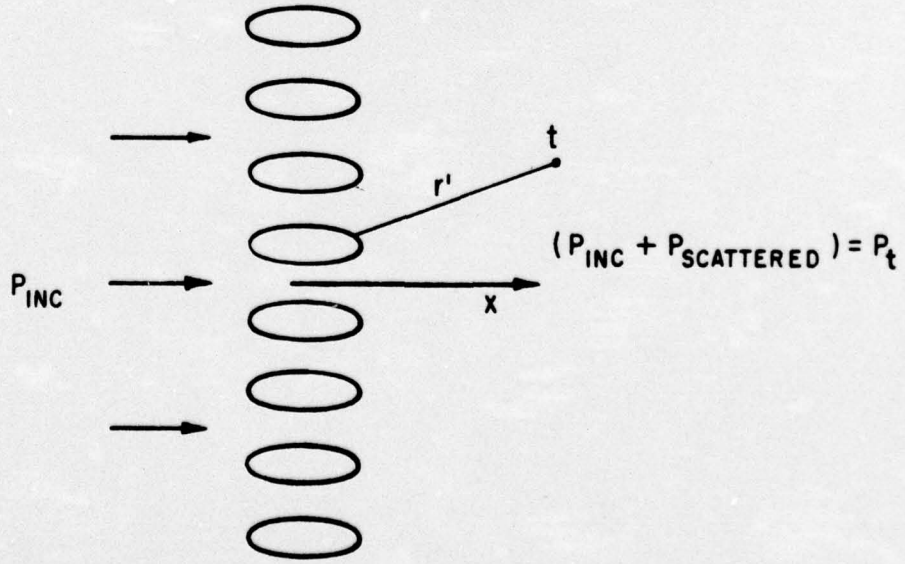

A TWO DIMENSIONAL ARRAY OF COMPLIANT TUBES

FIGURE 2

The total pressure at a point t is given by the sum of the incident and scattered pressure.

$$P_t = P_{inc} + P_{scattered}$$

$$= e^{ikx} + \int_o A(s',k)\ \phi\ (s',t)\ d\vec{l}$$

where

A(s',k) is the source strength

k is the wavenumber

$\phi(s',t) = J_o(kr') + i\ Y_o(kr')$ (zeroth order Hankel function)

In this formulation, the source strength integral describes the scattered wave. The unknown source strength is determined by satisfying the prescribed boundary conditions.

The tubes will be assumed to be resonance devices with an average mechanical impedance given by

$$Z_t = Z_{t_o}\ (1 - \frac{f^2}{f_o^2})$$

where

$$Z_{t_o} = \frac{-iB_t}{2\pi f}\left[\frac{A_t}{V_t}\right] \cong \frac{-iB_t}{2\pi f}\left[\frac{2(a^2+b^2)}{a^2b^2}\right]^{1/2}$$

f - Frequency

f_o - First flexural resonance frequency of the tube as measured in air

A_t - Surface area of the tube

V_t - Two dimensional volume of the tube

B_t - Bulk modulus of the tube

a - semi-minor axis of the ellipse

b - semi-major axis of the ellipse

The boundary condition that the tube becomes

$$-(P_{inc} + P_{scatt}) + \frac{iZ_t}{2\pi f\rho}\left[\frac{\partial P_{inc}}{\partial n'} + \frac{\partial P_{scatt}}{\partial n'}\right] = 0$$

where ρ is the density of the medium and

$\frac{\partial}{\partial n'}$ is the normal derivative at the surface of a tube.

A comparison of the prediction of the model with measurements is shown in Figure 3 for an array of ten steel tubes. The non-dimensional semiaxes of these tubes were $kb = 0.138\pi$ and the semiminor axes were $kb = 0.042$ at the single tube resonance frequency as measured in air. The major axis of a tube was aligned parallel to the direction of incident plane wave radiation and the center-to-center spacing was $kd = \frac{3}{5}\pi$ at the above frequency. The bulk modulus of the steel tubes were calculated and measured to be about 1/11 that of water. As seen from the measurement in the plane of the tubes, the reactive loading effect decreases the effective resonance frequency of the array in water 13 percent with respect to the single tube resonance frequency in air. The predictions from the arbitrary body program show a frequency shift of about 4 percent as compared with the measurements, but the predicted bandwidth agrees well with the data.

To obtain convergence for ten tubes with the above program requires at least five minutes/frequency of computer time on the Univac 1108. If one wished to investigate the properties of larger arrays of tubes and vary several array parameters, such an analysis becomes quite expensive. A mathematically simpler approach is to treat the tubes as acoustically round but retaining the same mechanical impedance function as was devised for the elliptical shape. Since the acoustic wavelengths of interest are large

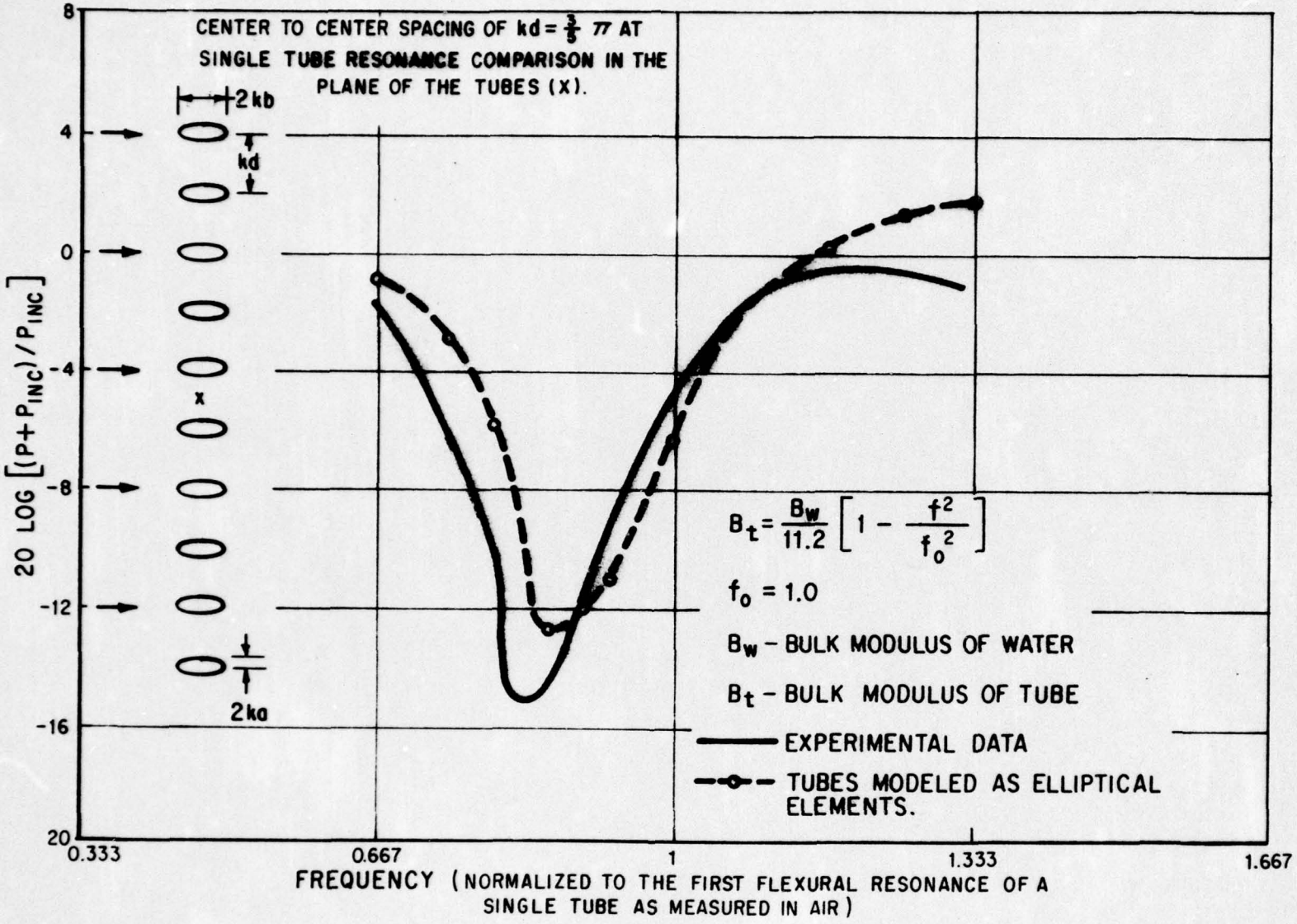

TEN STEEL TUBE ARRAY

FIGURE 3

compared with the dimensions of a tube, this approximation should not be critical. The scattered wave can then be described by series of cylindrical harmonic wave functions. The two dimensional volume of the round tubes was taken to be equal that of the corresponding elliptical tube.

As seen from Figure 4, the total pressure at point t becomes

$$P_t = P_{inc} + P_{scatt}$$

$$P_t = e^{ikr\cos\theta} + \sum_{\ell=1}^{L} \sum_{q=-\infty}^{\infty} {}^{\ell}A_q H_q(kr_\ell) e^{iq\theta_\ell}$$

where $H_q(kr_\ell)$ is the qth order Hankel function and A_q is an undetermined series coefficient.

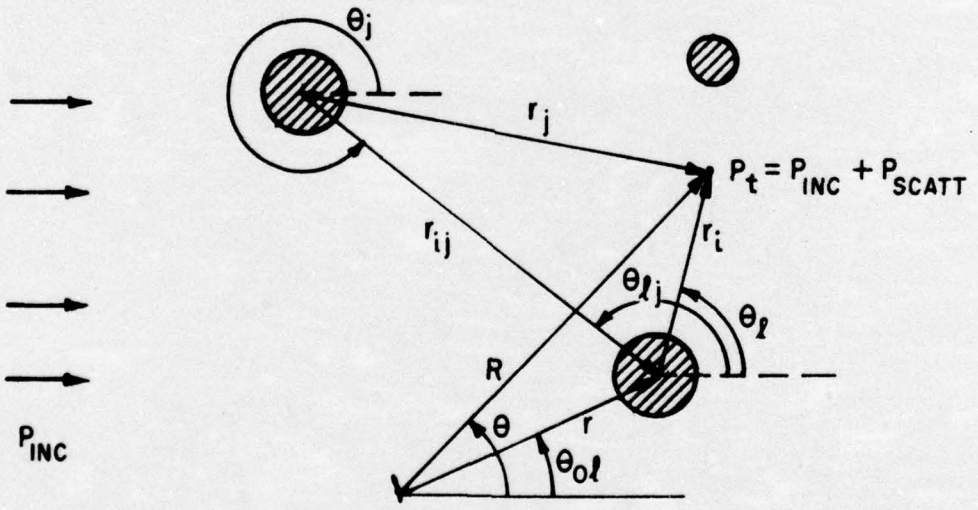

GEOMETRY FOR THE ROUND TUBE ANALYSIS

FIGURE 4

To satisfy the boundary conditions at the ℓth cylinder, rewrite P_{inc} in terms of Bessel functions as

$$P_{inc} = e^{ikr\cos\theta_{o\ell}} \sum_{q=-\infty}^{\infty} J_q(kr_\ell) e^{iq(\theta_\ell + \frac{\pi}{2})}$$

and use the Addition Theorem

$$H_q(kr_j) e^{iq\theta_j} = \sum_{m=-\infty}^{\infty} J_m(kr_\ell) H_{m-q}(kr_{\ell j}) e^{m\theta_\ell - (m-q)\theta_{\ell j}}$$

which expresses the cylindrical harmonics with respect to one coordinate system in terms of a second coordinate system.

The predictions from the round tube analysis are compared in Figure 5 with measurements taken in the center of the ten steel tube array. The frequency shift of 8 percent for the predicted curve with respect to the measurements is more pronounced than the curve obtained with the elliptically moded tubes (Figure 3). This additional frequenty shift is in part due to the closer effective spacing of the round tubes with respect to the equal area squashed elliptical tubes. As reported by Toulis[2], the mutual coupling in a plane area of compliant tubes causes the resonance frequency to approach that in vacuum as the spacing between the tubes decreases.

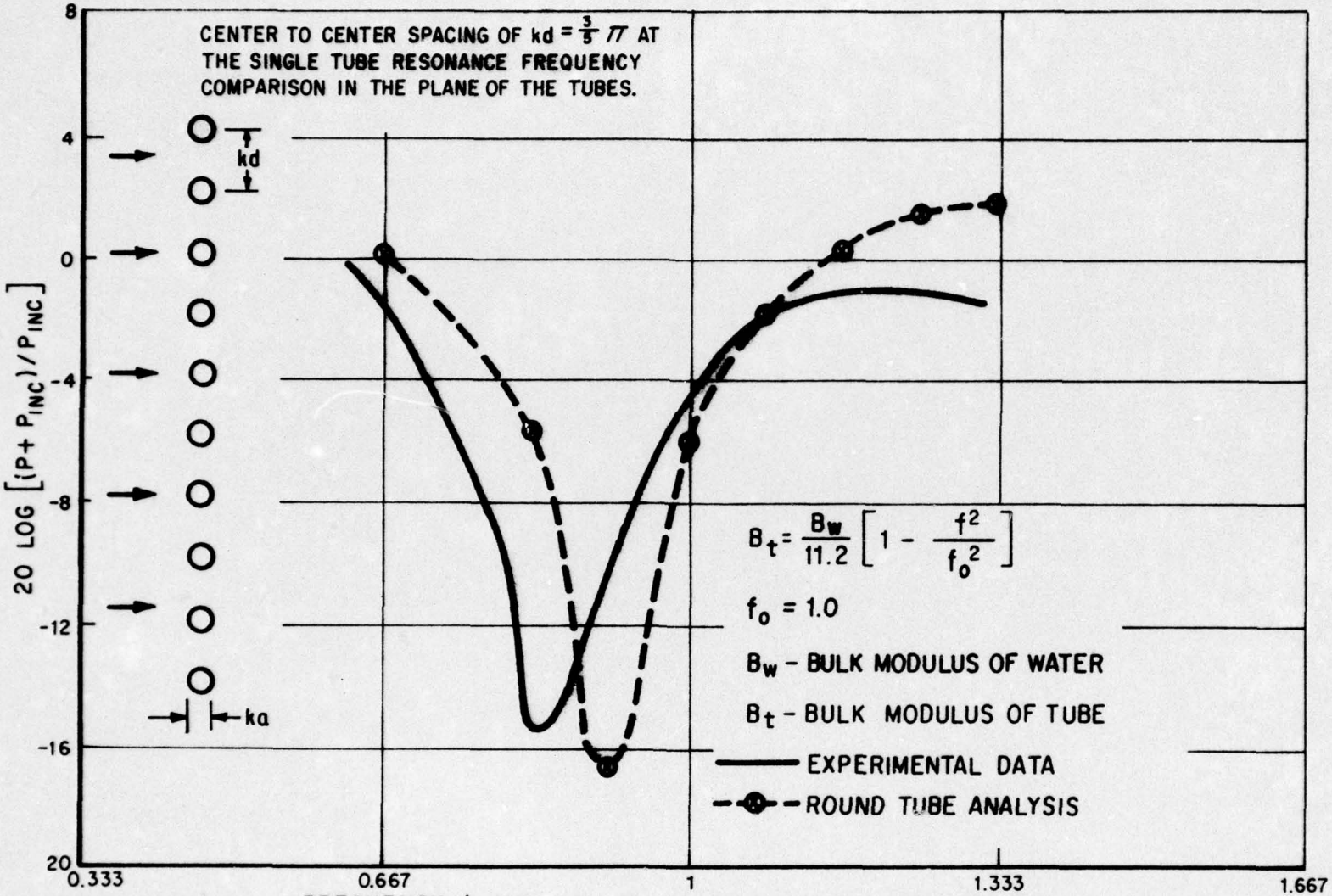

TEN STEEL TUBE ARRAY

FIGURE 5

CONCLUSION

Recent measurements made at NUSC with closely spaced plastic tubes will be used to determine any further modifications which might be made to the above models. Comparisons of model predictions with measurements from an area of ten steel tubes indicate that (1) the impedance function used to describe the tubes is reasonable for sparsely spaced arrays and (2) because the acoustic wavelengths are large compared with the dimensions of the tube, the mathematical shape used for an individual tube is not critical. The models described here are only the first step toward understanding the array performance in the actual situation where the tubes are imbedded in rubber and attached to a flexing metal surface.

REFERENCES

1. W.J. Toulis, "Acoustic Refraction and Scattering with Compliant Elements. II, Analysis", J. Acoust. Soc. Am., 29, 1027-1033, (1957).

2. W.J. Toulis, "Acoustic Refraction and Scattering with Compliant Elements. I, Measurements in Water", J. Acoust. Soc. Am., 29 1021-1026, (1957).